UNIVERSITY OF NOVA GORICA
GRADUATE SCHOOL

Characterization of atmospheric properties over the Cherenkov Telescope Array at La Palma

DISSERTATION

Miha Živec

Advisor: prof. dr. Samo Stanič

Ajdovščina, 2023

UNIVERZA V NOVI GORICI
FAKULTETA ZA PODIPLOMSKI ŠTUDIJ

Karakterizacija atmosferskih lastnosti nad Poljem Teleskopov Cherenkova na La Palmi

DISERTACIJA

Miha Živec

Mentor: prof. dr. Samo Stanič

Ajdovščina, 2023

Sognava rocce alte, spazi aperti e cielo
sopra la testa. Senza, era triste.

Mauro Corona

Acknowledgements

First, I would like to express my sincere gratitude to my mentor, Samo Stanič, for ten years of guidance, support, teaching, and constructive discussions that made this thesis possible. I would also like to thank all committee members for all the comments and improvements suggested, which made the work more consistent. Special thanks go to Brittni Benware for proofreading the thesis. I am also grateful for all the help and guidance on coding and data analysis given by Markus Gaug and Egon Pavlica. Additionally, special thanks go to Maruška Mole, William Eichinger, and Longlong Wang, who made an introduction to lidar methods much easier.

At this point, I would also like to thank all the members of the Barcelona Raman Lidar group and the past and present staff of the Center for Astrophysics and Cosmology, who accepted me as one of their own and became my second family during these four years. I am grateful to my fellow Ph.D. students, Taj Jankovič, Veronika Vodeb, and Erika Tomsič, for all the chats and discussions that solved many problems and made life at UNG much more pleasant.

Last but not least, there are no words to express my gratitude to my family for their continuous support throughout the years, without which nothing would be possible. I am grateful to Silvester for years of friendship and for being the closest thing to a brother that I ever had. I also extend my thanks to Anja, Ana, and Denise for countless hours of climbing and discussions that sometimes made life much simpler and sometimes much more complicated, but taught me that life is not just black and white.

THANK YOU ALL!

Abstract

Imaging Atmospheric Cherenkov Telescope (IACT) systems are used in high-energy astrophysics to detect and study gamma-ray sources in the universe. These telescopes measure properties of cosmic gamma rays using Cherenkov radiation emitted by secondary particles produced after interacting with the Earth's atmosphere. Atmospheric monitoring is crucial for the proper operation of IACT systems. A number of remote sensing and *in situ* methods are used to understand and correct the effects of the atmosphere on the propagation of Cherenkov radiation from its origin to the telescope. Failure to do so greatly decreases IACT performance, particularly, their energy resolution and threshold. Lidar systems can be used to measure atmospheric optical depth profiles, which are essential for IACT calibration.

The main aim of this thesis is to demonstrate that a prototype lidar for the northern site of the Cherenkov Telescope Array Observatory (CTAO), which is a next-generation IACT now under construction, has hardware and software capabilities that would lead to the construction of CTAO Raman lidar. Due to specific requirements of the CTAO, a Raman lidar, which can provide better atmospheric parameter accuracy, will be used for the first time in an IACT system. In 2021-2022 the BRL was deployed to the future CTAO-North site at the Roque de los Muchachos observatory, La Palma, for testing in its actual operating conditions. During a year and a half long test period, it underwent a number of tests, including manual and remote operation under various environmental conditions. These included hot summers, cold winters, rain, snow, ice, and strong winds, but also some more exotic events, such as desert sand intrusions (Calima) and volcanic eruptions. The latter two are presented in this work as test cases for atmospheric characterization.

Since the main goal of a CTAO lidar is the optical depth measurements, the BRL does not have the full set of features for aerosol characterization. While it can yield the Ångström exponent and lidar ratio, it does not provide depolarization information, which is one of the key components for aerosol typing. As the atmosphere at La Palma was found to be more complex than initially anticipated, we present the benefits of including depolarization capability by using a conceptually similar Raman lidar system specifically designed for aerosol characterization. We present the results of a campaign focused on the determination of bioaerosol capabilities to act as cloud condensation nuclei and ice-nucleating particles in mixed-phase clouds, where depolarization information was used to determine the thermodynamic phase of the cloud.

Keywords: Cherenkov Telescope Array Observatory, Raman Lidar, atmospheric optical depth, aerosol characterization, Cumbre Vieja, Calima

Povzetek

Teleskopi za zaznavanje bliskov Čerenkove svetlobe v atmosferi (IACT) se uporabljajo v visokoenergijski astrofiziki za odkrivanje in proučevanje izvorov kozmičnega sevanja gama. Za zaznavanje primarnih visokoenergijskih kozmičnih fotonov izkoriščajo sevanje Čerenkova, ki ob njihovem vpadu nastaja v zemeljski atmosferi. Oddajajo ga sekundarni delci, ki nastanejo ob interakcijah primarnih fotonov z atomskimi jedri atmosferskih plinov. Ker je atmosfera stalno spreminjajoči se sistem, moramo za natančne meritve lastnosti primarnih kozmičnih fotonov čimbolje poznati dogajanje v njej. Najpogosteje se za to uporablja daljinsko zaznavanje s pomočjo lidarja (Light Detection and Ranging), s katerim je mogoče izmeriti profil atmosferske optične globine (bistvenega pomena za korekcijo učinkov atmosfere na razširjanje sevanja Čerenkova) vzdolž smeri pregledovanja.

Glavni cilj disertacije je razvoj in prikaz strojnih in programskih zmogljivosti prototipa lidarja za observatorij Polje teleskopov Čerenkova (CTAO). Zaradi zahtev po visoki ločljivosti rekonstrukcije energije kozmičnih fotonov bo v CTAO prvič uporabljen Ramanski lidar, ki lahko zagotavlja večjo natančnost meritev atmosferskih parametrov kot elastični lidar. Naš prototip, imenovan tudi "Barcelona Raman Lidar" (BRL), med lidarskimi sistemi izstopa z velikim zrcalom in močnim laserjem. Zasnovan je, da popolno karakterizacijo atmosfere nad CTAO izvede kar v najkrajšem času. V letih 2021–2022 smo BRL preizkušali na severni lokaciji CTAO na La Palmi, Španija. Preizkusili smo delovanje pod pogoji, v katerih bo moral obratovati ramanski lidar CTAO. V letu in pol dolgem testnem obdobju je bil podvržen številnim preizkusom, vključno z ročnim in daljinskim upravljanjem v različnih okoljskih pogojih. Poleg običajnih so ti vključevali tudi nekatere eksotične dogodke, kot so vdori puščavskega peska (Calima) in vulkanski izbruh, predstavljene kot testni primeri.

Glavni rezultat meritev bodočega Ramanskega lidarja CTAO so meritve optične globine atmosfere, čemur je prilagojena zasnova lidarja. BRL kot prototip zato nima polne funkcionalnosti za karakterizacijo aerosolov (nima možnosti meritve depolarizacije pri sipanju svetlobe, ki je ena ključnih komponent za ugotavljanje tipa aerosolov), vseeno pa lahko na podlagi meritve Ångström-ovega eksponenta in lidarskega razmerja nudi omejen vpogled v sestavo aerosolov v ozračju. Zaradi opažene kompleksne sestave aerosolov nad La Palmo predstavljamo prednosti vključitve zmožnosti meritve depolarizacije na observatoriju CTAO. Kot primer smo uporabili meritve BRL konceptualno podobnega sistema Ramanskega lidarja v Sloveniji, ki je bil posebej zasnovan za karakterizacijo aerosolov. Predstavljamo rezultate raziskave, osredotočene na določanje zmožnosti bioaerosolov, da delujejo kot potencialna kondenzacijska jedra oziroma jedra za tvorbo lednih kristalov v oblakih. Informacije o depolarizaciji smo uporabili za določitev termodinamske faze oblaka.

Ključne besede: Polje teleskopov Čerenkova, Ramanski lidar, atmosferska optična globina, karakterizacija aerosolov, vulkan Cumbre Vieja, Calima

Contents

1

Introduction

1.1 Motivation

In 1989, when the imaging atmospheric Cherenkov telescope (IACT) built by the Whipple telescope collaboration [1] detected the first TeV gamma ray, a new observation window for gamma-ray astronomy opened by covering the most energetic (GeV to TeV) part of the electromagnetic spectrum. In the stereo configuration of multiple telescopes, a technique where an image of Cherenkov light signature of extensive air shower (EAS) development is taken, allowing for accurate direction and energy reconstruction of a primary gamma ray. The EAS is created when a very high energy gamma ray hits nuclei of atmospheric gases, and its development depends on primary gamma-ray energy and the molecular density profile along its trajectory [2]. During the interaction, energy is transferred, propelling particles toward the ground, and hitting more particles along the way. The secondary particles travel faster than the speed of light through the atmosphere, radiating Cherenkov light. As the atmosphere consists of constituent gases and particles in suspension, light passing through this medium scatters, and a fraction of the incident beam is dissipated in all directions. The scattering processes can either be elastic, where the scattered photons have the same energy as the incident ones, or inelastic, where energy exchange with the scatterers occurs, and the scattered photons have lower energy than the incident ones. This reduces the total amount of Cherenkov light reaching the observer at ground level, thus increasing the measured data uncertainty. Most events that affect atmospheric optical properties occur in the troposphere and tropopause. At the Cherenkov Telescope Array Observatory (CTAO) northern site, located at the Observatorio del Roque de los Muchachos (ORM) on the Canary Island of La Palma, with an approximate latitude of 28° North, the troposphere extends from the ground to the altitudes between 6 km and 18 km [3], depending on the time of year. While the atmospheric molecular content varies slowly [4], usually on time scales of the order of days to months, the aerosol concentrations change much faster on the order of hours. The aerosols are most abundant in the lowest part of the troposphere, the planetary boundary layer

(PBL), which experiences a regular daily cycle of its properties due to solar irradiation. The PBL can be between a few hundred meters to several kilometers thick at the CTAO-N site [5] and is directly influenced by interactions of the atmosphere with the Earth's surface [6, 7] and experiences turbulent transport of moisture and aerosols. Large aerosol densities in the PBL strongly influence light travel due to absorption and scattering. Even though the PBL almost completely lays down to the ground during the night, it may leave some residual layer that interferes with the Cherenkov light emitted by EAS [8]. Even faster changes in aerosol density can be created by low-altitude atmospheric events such as desert dust intrusions or salt and seawater droplets carried by strong winds can change light extinction of the atmosphere in a matter of minutes. Since the losses of the Cherenkov light can happen at different altitudes, an altitude-dependent assessment of the atmospheric extinction is mandatory to reduce the errors created due to the changing atmospheric conditions.

1.2 State of the art in the field

IACTs use the atmosphere as a calorimeter and direction tracker. For accurate data analysis and interpretation, one must have a good knowledge of the detector behavior, i.e., the atmosphere, which means that its processes need to be well understood. The ever-changing medium creates limitations on the use of such facilities, so some attempts to calibrate IACTs from standard candles (like in astronomy) have been made [9]. Problems also arise in attempts of cross-calibration with satellites [10], as they operate at a lower energy range than IACT facilities. This shows that a new approach to characterize atmospheric disturbances is needed. Throughout time, multiple different ways of telescope calibration and atmosphere monitoring were used. The first energy calibrations, used for telescope monitoring, were combinations of Monte Carlo simulations with calibration of the sensitivity with a reference light source [11, 12] and absolute energy threshold calibrations (e.g., muon images) [13, 14], yielding $10\% - 25\%$ accuracy on energy reconstruction. To increase reconstruction accuracy, IACT observatories moved to more active monitoring of the atmosphere with devices specially built for this purpose. This extends the capabilities of previously developed methods, e.g., exchanging reference light sources for wide-field stellar photometry with a dedicated telescope like FRAM (F/Photometric Robotic Atmospheric Monitors) [15, 16]. The problem with this still arise since only total optical aerosol depth can be inferred without additional assumptions. A more active approach has to be taken to get exact measurements of vertical aerosol loading throughout the atmosphere. This led to the use of lasers for telescope calibration [17]. In this case, a telescope collect Rayleigh backscattered light, and knowing the initial pulse intensity allows to make absolute telescope calibration accurately. To further extend the capabilities of this method, one can create a detector designed specifically for the task. For this, we find perfect candidates in ceilometers [18] and lidars [18, 19, 20], devices that were designed in the past for remote monitoring of the atmosphere through means of light propagation and backscattering. The approach of active measurements of verti-

cal atmospheric profiles can reduce the uncertainties created by interactions between the Cherenkov light and the atmosphere [8, 21]. The development of air showers is influenced by the molecular density profile along its path. The loss of Cherenkov photons can also be impacted by absorbing molecules and, more significantly, by scattering outside the camera's field-of-view due to both molecular (Rayleigh) and aerosol (Mie) scattering. Although clouds are usually not as thick as air showers, which can span several kilometers, they can still reduce the amount of Cherenkov light visible in the field of view of an IACT. Based on the primary gamma-ray energy, the shower maximum's interaction depth can result in energy-dependent effects if a cloud layer is at a specific altitude [22].

The need for more accurate measurements grew with the growth of the field of IACT astrophysics. Different observatories tackled the problem of corrections of atmospheric influence in different ways, with different success, but managed to drive the capabilities of atmospheric monitoring very far [5]. As a next-generation experiment, the Cherenkov Telescope Array Observatory collected experience from those that came before to increase the accuracy of atmospheric calibration even further [2, 23].

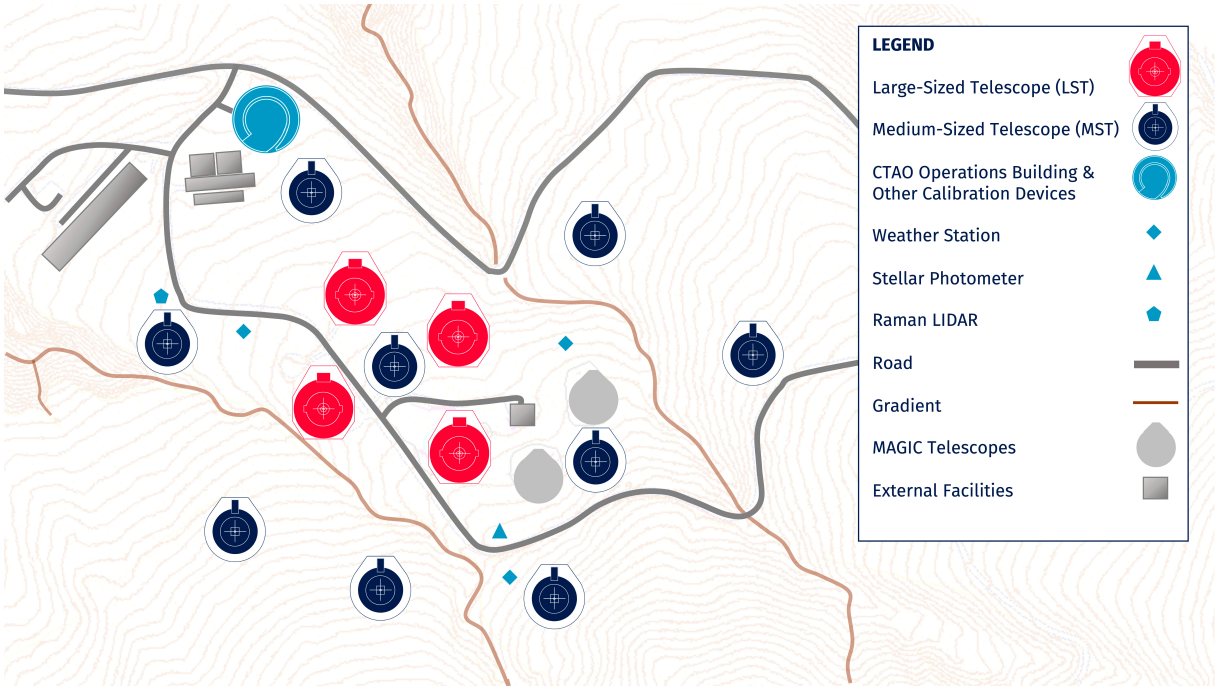

Figure 1.1: Layout of the CTAO Northern array at the Observatorio Astrofísico Roque de Los Muchachos, La Palma, Spain. The layout includes all the facilities that will comprise Alpha Configuration, among others, and the Raman lidar. © Cherenkov Telescope Array Observatory 2022.

1.3 Cherenkov Telescope Array

The Cherenkov Telescope Array Observatory (CTAO) is the next-generation IACT observatory allowing it to reach a sensitivity and resolution beyond the potential of currently operating Cherenkov telescopes [24]. Along with this increase in performance, the CTAO will manage to observe the whole sky visible from the Earth. There will be two sites to cover the sky - one in the northern (La Palma, Spain) and one in the southern hemisphere (Paranal, Chile). The larger site will be the southern site (CTAO-South) built at an altitude of about 2100 m a.s.l., while the northern site (CTAO-North) will be positioned at the Roque de los Muchachos, at 2400 m a.s.l.. The final configuration of CTA will hoast more individual telescopes than any other existing array, with CTA North having 13 telescopes spread over 0.6 km^2 and CTA South having 58 telescopes covering an area of approximately 4 km^2 after re-scoping. The telescopes are divided into three categories based on their dish size: Large-Sized Telescopes (LSTs) with a 23 m diameter, Medium-Sized Telescopes (MSTs) with an 11.5 m diameter, and Small-Sized Telescopes (SSTs) with a 4 m diameter. The Northern site of CTA will feature 4 LSTs and 9 MSTs, while CTA South will consist of 4 LSTs, 14 MSTs, and 40 SSTs in its final stage (Fig. 1.1). The CTAO will explore our Universe in depth in VHE gamma rays and investigate cosmic processes leading to the emission of ultra-relativistic particles with unprecedented sensitivity. An energy range from 100 GeV to 10 TeV CTA sensitivity will be 5-10 times better compared to existing experiments (Fig. 1.2). While this is the main CTAO operational energy range, the observatory will uniformly cover energies from 20 GeV to 300 TeV. Each type of telescope serves a specific purpose to achieve these energy coverage goals. LSTs are particularly well-suited for detecting gamma rays in the lower energy range of CTAO, with detection range from 20 GeV to 150 GeV. These events occur more frequently but produce a limited amount of Cherenkov light, making the large dish diameter necessary to collect the incoming photons. MSTs are the backbone of the array, covering energies from 150 GeV to 5 TeV. The SSTs are only used at the Southern site to enhance the performance at the highest energies, as the area around the galactic center that ought to produce gamma rays of the highest energies is only visible from CTAO-South. Their sensitivity covers the range from 5 TeV to 300 TeV, and as such events are relatively rare, a large number of SSTs must be spread over a large area to obtain stereoscopic detection of the same Cherenkov light. With its unique abilities, CTAO will tackles some of the major questions in astrophysics and fundamental physics. The studies will include a search of the origins of cosmic rays, exploration of the vicinity of neutron stars, pulsars, and black holes, and search for dark matter and other phenomena beyond the Standard Model.

1.3.1 Cherenkov Telescope Array strategy for atmospheric calibration

The CTAO Central Calibration Facilities aim to establish a comprehensive calibration strategy that builds upon the lessons learned from previous IACTs and the Pierre

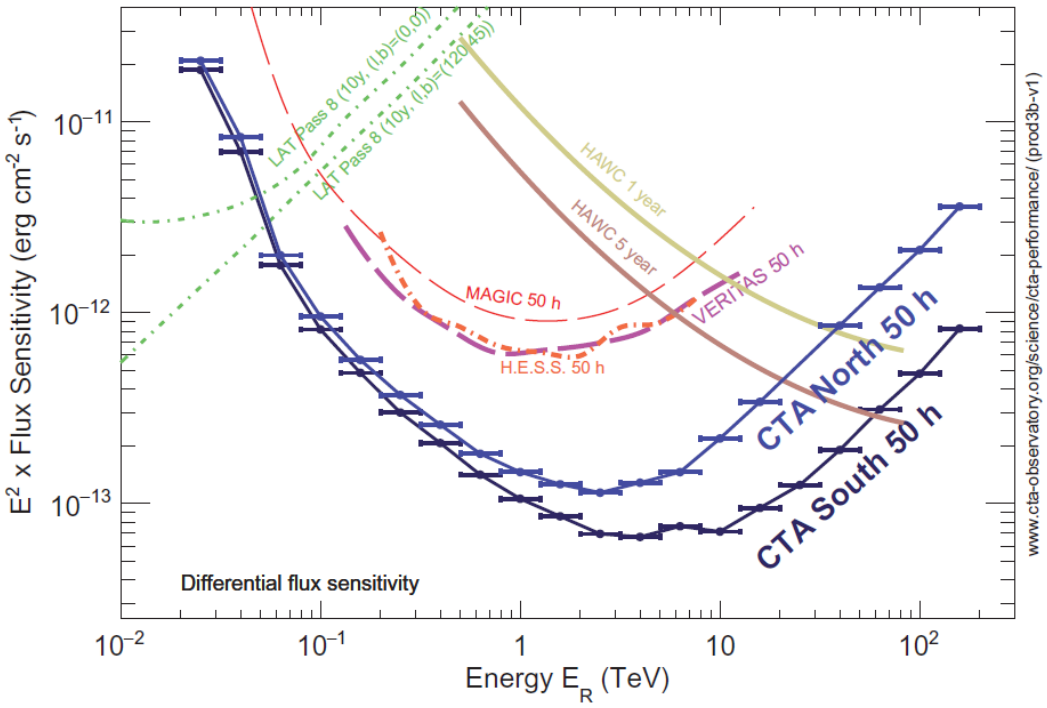

Figure 1.2: Comparison of the performance of CTA with Fermi-LAT, HAWC, MAGIC and H.E.S.S. The curves shown give only an indicative comparison of the sensitivity of the different instruments, as the method of calculation and the criteria applied are different. Figure adopted from [24].

Auger Observatory [17, 18, 25, 26]. To achieve this, a key component of the strategy is to thoroughly assess the characteristics of each site ahead of time and create customized devices and methods for monitoring each parameter. Unlike prior IACTs, these must have a wide field of view of over 10° x 10° and measure the extinction profile with a precision of a few percent. It has been realized that the current scheduling strategies of IACTs have room for improvement by taking into account atmospheric conditions for specific scientific objectives. This is particularly crucial for sources with very soft spectra that can only be observed below 100 Gev and require clear nights for accurate results, known as "photometric nights" in optical astronomy. The same applies to precise pointing observations, where low-energy events that do not trigger the readout are lost and cannot be corrected, unlike data from higher energy targets. The CTAO decided that the first step for atmospheric characterization above experimental sites would start even before the construction of the main part of the observatory. Various characterization activities are performed on-site to determine the atmospheric conditions of both locations. This information is necessary to establish requirements for the atmospheric monitoring systems and make remaining design decisions. The sites are evaluated using a radio sonde campaign to examine molecular profiles and assess the accuracy of global data assimilation systems that predict density profiles. A

lidar project [27] is also being carried out to analyze aerosol profiles, and a Sun/Moon photometer [28] is used. To continuously monitor the field-of-view for scientific observations, dedicated systems such as a Raman lidar [29], a small optical telescope (FRAM) [15] for measuring atmospheric extinction through stellar photometry will be used, whose prototypes are tested on-site. Other instruments, like an All-Sky Camera (ASC) [30] and a commercial Ceilometer, are being deployed to assess cloud coverage and altitudes, respectively, and assist in site characterization.

The use of lidar for atmospheric monitoring is quite common in high-energy astrophysics. However, the CTAO will be the first to employ the Raman channels in addition to the elastic ones. The lidar must meet several criteria to achieve CTAO needs. The lidar must measure extinction profiles up to altitudes of at least 15 km a.s.l., where extended air-showers are typically formed [31], to calibrate CTAO for any atmospheric effects along its line of sight. Since the CTAO can operate to the zenith angle of 60°, so must the lidar. Following the previous two points, the lidar range must be at least 30 km. The LIDAR range resolution must be at least, or better than, ∼300 m to cover the typical air-shower range of several kilometers. Early studies [32] have already shown that aerosol transmission profiling is best determined with powerful Raman lidars, which should be equipped with near-range optics in order to determine the full ground layer transmission reliably to meet the aerosol transmission accuracy requirement. Moreover, stratospheric aerosol extinction should be accessible to the LIDAR, at least when pointing toward the zenith. The atmosphere must be characterized using at least two wavelengths present in the Cherenkov light spectrum to be able to measure the aerosol transmittance with absolute accuracy of 0.03 [31]. A Nd:YAG laser, operating at its second and third harmonic frequency, provides the capability to characterize the atmosphere at 532 nm and 355 nm, which cover most of the measured Cherenkov light spectrum. Laser light from the lidar would blind the CTAO telescopes, so the data collection must be performed a few minutes before and after a CTAO observation period and during the changes of Wobble position or with dedicated trigger vetos. Lidar must perform full characterization of an extinction profile during a circa minute-long interval to achieve this. This can be performed with a short burst of about 500 laser pulses at a repetition rate higher than 10 Hz. The problem of collecting a large enough amount of light from this short-duration measurement is solved by using bigger mirrors than those usually used in lidars for meteorological atmosphere monitoring.

2

Remote sensing of atmospheric properties

In this chapter, the basic concepts about the atmosphere and light propagation through it will be presented. Chapter 2. is not a result of my work but is of the utmost importance for understanding the work and results presented in this thesis.

2.1 Atmospheric structure

The atmosphere is a layer of gases and aerosols that surround the Earth and comprises several layers (the main layers are the troposphere, stratosphere, mesosphere, thermosphere, and exosphere), which are usually defined by temperature behavior. Another thermodynamic variable that highly influences the environment is atmospheric pressure, due mainly to hydrostatic pressure produced by the weight of air. It follows the density distribution of the atmosphere that decreases approximately exponentially with height. The lowest layer of the atmosphere is the troposphere. It extends from the Earth's surface up to a height of approximately 17 km kilometers above the equator and 9 km above the poles. The thickness in regions in between depends on the time of year and is highest in summer. The troposphere ends with the tropopause, which shows an absolute temperature change rate below 2 °C/km and is approximately 2 km thick. In the troposphere resides approximately 80% of the atmosphere's mass, including most of the atmosphere's water vapor. This is also the layer in which most of the weather phenomena occur. The temperature in the troposphere falls with height, except in cases of inversion, where temperature increases with height in the first few hundred meters to up to a few kilometers, creating a very stable environment. The standard temperature lapse rate is 6.5 °C/km. The lowest part of the troposphere, which is in direct contact with the ground, is called the planetary boundary layer (PBL). Its height significantly depends on ground configuration and changes during the day, reaching its highest point in the afternoon. The PBL, on average, reaches 1500 m above the homogeneous ground and 500 m above large bodies of water. Obstacles on the ground create a drag on the moving air, which creates mixing and changes the direction of air movement. That is known as a tur-

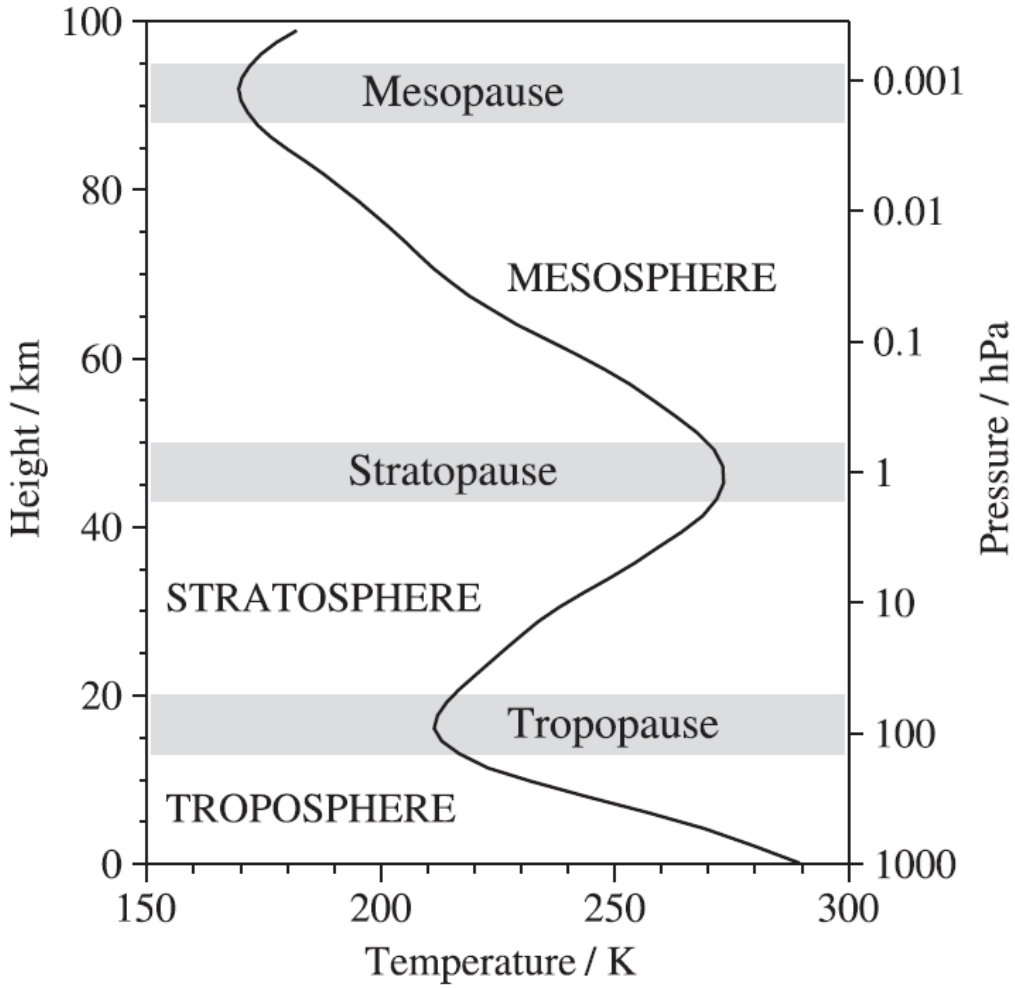

Figure 2.1: Typical vertical cross section of the first 100 km of the atmosphere. The height is in km, temperature in K and pressure in hPa. The figure is taken from [33].

bulent movement of winds in the PBL. Above the PBL is a free atmosphere that does not depend on the roughness of the terrain. In cases of an unstable atmosphere, convection starts. Convection breaks PBL, and the influence of the ground reaches through the whole troposphere. The tropopause stops convection at the top of the troposphere. On the other hand, if a temperature inversion appears and creates very stable atmospheric conditions, ground influence only reaches as high as the top of the inversion layer. Above the troposphere lies the stratosphere. This layer extends from the top of the tropopause to about 50 km above the ground. It contains the ozone layer, which protects Earth's life from harmful sun ultraviolet radiation. The temperature in the stratosphere generally increases with altitude. This layer is relatively stable and contains little water vapor, but the occurrence of stratospheric clouds is not impossible. The stratopause blocks the top of the stratosphere. The stratosphere is

followed by the mesosphere reaching up to 85 km. The mesosphere is characterized by temperature decreasing with altitude and by high winds. After the mesosphere, the atmosphere contains barely any particles. Through the thermosphere, (from 85 km to about 600 km), and exosphere (from 600 km to about 10000 km), slowly dissipates into the space.

2.2 Light wave

In the region of space where there is no charge or current [34], we have Maxwell's equations in the following form:

$$\vec{\nabla} \cdot \vec{E} = 0, \tag{2.1}$$

$$\vec{\nabla} \cdot \vec{B} = 0, \tag{2.2}$$

$$\vec{\nabla} \times \vec{E} = -\frac{\partial \vec{B}}{\partial t}, \tag{2.3}$$

$$\vec{\nabla} \times \vec{B} = -\mu_0 \epsilon_0 \frac{\partial \vec{E}}{\partial t}. \tag{2.4}$$

This is the set of coupled first-order, partial differential equations for the electric field $\vec{E}$ and the magnetic field $\vec{B}$. If the curl is applied to 2.3 and 2.4, we can decouple equations for $\vec{E}$ and $\vec{B}$, but they become of the second order.

$$\nabla^2 \vec{E} = \mu_0 \epsilon_0 \frac{\partial^2 \vec{E}}{\partial t^2}, \tag{2.5}$$

$$\nabla^2 \vec{B} = \mu_0 \epsilon_0 \frac{\partial^2 \vec{B}}{\partial t^2}. \tag{2.6}$$

In a vacuum, each Cartesian component of $\vec{E}$ and $\vec{B}$ satisfies the three-dimensional wave equation, traveling at the speed of approximately:

$$c = \sqrt{\frac{1}{\mu_0 \epsilon_0}} \cong 3 \times 10^8 \,\mathrm{m/s}.$$

The wave can be described as a monochromatic plane wave in its simplest form. It is confined to a single frequency ω, and when traveling through space in a single direction (z for discussion purposes, but can be any arbitrary direction), has no x or y dependency. This is because the fields are uniform for every plane perpendicular to the direction of propagation. Such fields can then be rewritten as

$$\tilde{\vec{E}}(z,t) = \tilde{\vec{E}}_0 \exp(ikz - i\omega t), \tag{2.7}$$

$$\tilde{\vec{B}}(z,t) = \tilde{\vec{B}}_0 \exp(ikz - i\omega t), \tag{2.8}$$

where $\tilde{\vec{E}}_0$ and $\tilde{\vec{B}}_0$ are complex amplitudes, and the *physical* field is represented by real components of those amplitudes and $\omega = ck$. Maxwell's equations 2.1 and 2.2 provide additional constraints, resulting in

$$(\tilde{E}_0)_z = (\tilde{B}_0)_z = 0. \tag{2.9}$$

This implies that the electromagnetic waves (EM) are transverse, meaning that electric and magnetic fields are perpendicular to their direction of propagation. From Faraday law and the fact that $\vec{E}$ and $\vec{B}$ are in phase and mutually perpendicular, one gets the relation of their real amplitudes to be

$$B_0 = \frac{1}{c} E_0. \tag{2.10}$$

The final form of the real part of $\vec{E}$ and $\vec{B}$ fields, where $\vec{E}$ is pointing in x direction and $\vec{B}$ is pointing in y direction can be written as

$$\vec{E}(z,t) = E_0 \cos(kz - \omega t + \delta)\hat{x}, \tag{2.11}$$

$$\vec{B}(z,t) = \frac{1}{c} E_0 \cos(kz - \omega t + \delta)\hat{y}. \tag{2.12}$$

This is a monochromatic plane wave polarized in the x direction, as shown in Fig.

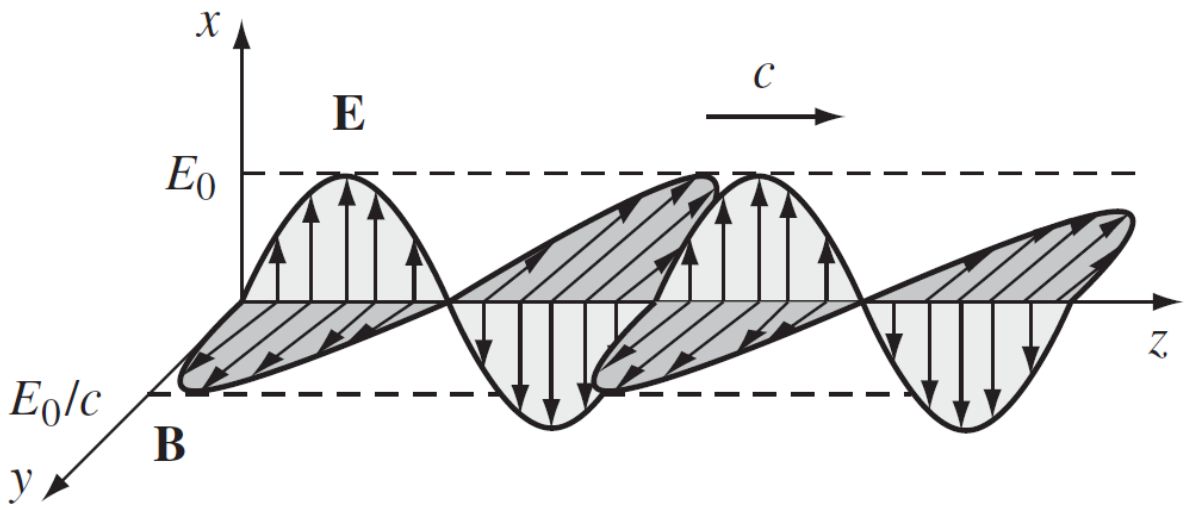

Figure 2.2: Depiction of a monochromatic plane wave described by the equations 2.11 and 2.12. The wave is traveling in z direction and has $\vec{E}$ field component in x direction and $\vec{B}$ field component in y direction. It is polarized in x direction (polarization is by convention the same as the direction of the $\vec{E}$ field). The figure is taken from [34].

2.2.

2.3 Light scattering

'Scattering' is a physical process in which particles constantly absorb and reradiate the energy from the incident electromagnetic wave [35]. In this way, particles can be described as a point source of the scattered energy. The size of particles on which light scatters in the atmosphere varies from angstrom (gas molecules) up to a centimeter (large raindrops and hail). The effect of particle size on scattering can be determined from the size parameter, which is for spherical particles defined as

$$x = \frac{2\pi a}{\lambda}, \tag{2.13}$$

where a is particle radius and λ is wavelength of the incident wave. If $x \ll 1$, the scattering is called Rayleigh scattering; if $x \geqslant 1$, it is called Lorentz-Mie scattering. Along the wavelength of incident light and geometric size, the intensity of light scattering depends on the characteristics of the scatterers, such as the shape and refractive index of particles, as well as the number density of these particles in the path of the light. Rayleigh scattering occurs equally in a forward and backward direction, while Mie scattering may highly increase the concentration of energy propelled in a forward direction (see Fig.2.3).

2.3.1 Rayleigh scattering

Rayleigh scattering [6, 35, 36] is the elastic scattering of electromagnetic radiation by molecules and particles much smaller than the wavelength of the incident radiation ($x \ll 1$). When radiation reaches a particle, a homogeneous electric field is produced (applied field). Due to the small size of the particle, this field generates a dipole configuration on it. We can connect this induced dipole moment $\vec{p}_0$ and total electric field $\vec{E}_0$ (combination of applied field and particles own field) through the electrostatic formula

$$\vec{p}_0 = \alpha \vec{E}_0, \tag{2.14}$$

where α represents the polarizability of a small particle. The applied field generates oscillation of an electric dipole in a fixed direction, producing a plane-polarized electromagnetic wave (the scattered wave). To evaluate the scattered wave far from the dipole, we assume that the scattered electric field is proportional to the acceleration of the dipole moment, the sine of the angle toward the observation point γ and inversely proportional to the distance from observer r:

$$\vec{E} = \frac{1}{c^2}\frac{1}{r}\frac{\partial^2 \vec{p}}{\partial t^2}\sin\gamma. \tag{2.15}$$

Ignoring depolarization effects (assumption of a perfectly spherical particle), we can describe an angular scattering coefficient β for wavelength λ and direction θ, in direction relative to the direction of the incident radiation as

$$\beta_{\theta,m} = \frac{\pi^2(n^2-1)^2 N_m}{2N_s^2\lambda^4} P(\Theta), \tag{2.16}$$

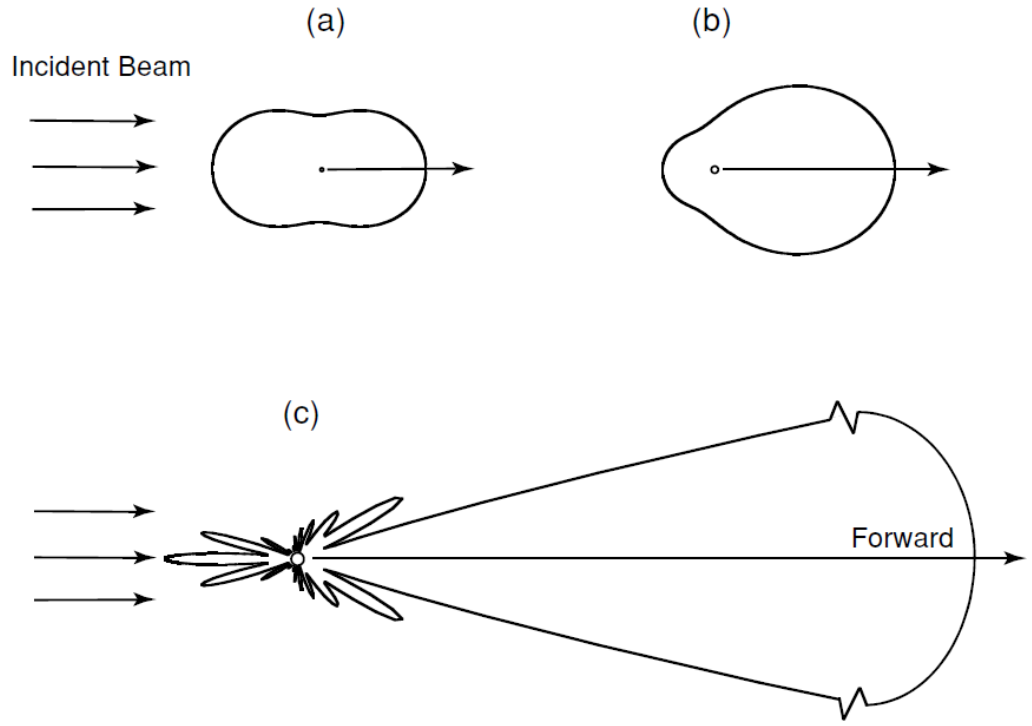

Figure 2.3: Angular patterns of the scattered intensity from spherical aerosols of three sizes illuminated by light: (a) a particle much smaller than the wavelength of light, (b) the size of a particle is approximately the same as the wavelength of light, (c) the particle is much bigger than the wavelength of light. In the (c) case, the forward scattering pattern is extremely large and is scaled for presentation purposes [35].

where n is the real part of the refractive index of the scattering medium, N_m the number density of molecules at the scattering point, N_s the number density of molecules at standard conditions, and $P(\Theta) = (1 + \cos^2\theta)$ the Rayleigh phase function for isotropic air molecules. In figure 2.3, we can see that the scattered light is symmetric around the direction of travel of the light beam, so that the intensity scattering coefficient can be rewritten as:

$$\beta_m = \frac{8\pi^3(n^2-1)^2 N_m}{3N_s^2\lambda^4}. \tag{2.17}$$

This can then be further reduced to a scattering cross-section (amount of scattering due to a single molecule):

$$\sigma_m = \frac{\beta_m}{N_m} = \frac{8\pi^3(n^2-1)^2}{3N_s^2\lambda^4}. \tag{2.18}$$

The scattering cross-section represents the amount of incident energy that is removed from the original direction because of a single scattering event such that the energy is

redistributed isotropically on the area of a sphere (the center of which is the scatterer) with radius r. In terms of the scattering cross-section, the scattered intensity can be expressed by

$$I(\Theta, r) = I_0 \frac{\sigma_m}{r^2} \frac{P(\Theta)}{4\pi}. \tag{2.19}$$

2.3.2 Lorentz-Mie scattering

Lorentz-Mie scattering [6, 35, 37, 38, 39] is the elastic scattering of electromagnetic radiation by molecules and particles which are similar in size or bigger than the wavelength of the incident radiation (size parameter from Eqn. 2.13 becomes $1 \lesssim x$). Particles of similar size as the wavelength of the incident light start to look upon a wavefront as a collection of separate rays [40], which can be considered independently from each other. When rays hit a particle's surface, they partially reflect and partially refract. This refraction can be visualized as an interaction of the waves that wrap themselves around a particle or travel through it. Different refracted rays emerge from the particle from different directions as they can travel around the particle or reflect inside it once or multiple times. After the incident with the particle, interference between these rays occurs. Constructive interference increases light traveling to specific directions and decreases in all other directions due to destructive interference. If the particle is much bigger than the wavelength of light, laws from geometric optics start to govern [40].

For the Lorentz-Mie scattering, the intensity scattered by a particle is a function of the direction, as shown in Eqn. 2.19, where

$$\frac{\sigma_s}{r^2} = \Omega_{eff} \tag{2.20}$$

the effective solid angle upon which scattering occurs. The scattering cross section σ_s is through the scattering efficiency parameter Q_s connected to the size parameter x as

$$\frac{\sigma_s}{\pi a^2} = Q_S = c_1 x^4 (1 + c_2 x^2 + c_3 x^4 + ...), \tag{2.21}$$

where the leading term is the dipole mode contribution from Rayleigh scattering. Eqn. 2.18 can be extended to all particles and in combination with Eqn. 2.21, a total scattering coefficient β_p can be rewritten as:

$$\beta_p = N_p \pi a^2 Q_s. \tag{2.22}$$

In reality, the assumption of an atmosphere full of particles uniform in size and composition is impractical; thus, the approximation in 2.22 needs to be extended to a polydisperse scattering. The scattering coefficient then becomes

$$\beta_p = \sum_{i=0}^{n} N(a_i) \pi a_i^2 Q_{s,i}, \tag{2.23}$$

with i being the constituent type. Similarly to Rayleigh scattering, light scattering direction preferences on bigger particles depend on a phase function $P(\Theta)$. In this case, the angular dependence becomes more complicated than in the case of scattering on point-like particles, and from Fig. 2.3 we can see that forward scattering preference increases with the increase of size parameter defined in Eqn. 2.13. The problem with particulates in the atmosphere is that sampling and determining their parameters is complicated as they are hard to access individually. This can be worked around with the approximated description of the wavelength dependence of their scattering efficiency. This can be done using an Ångström exponent, u, defined by the relation

$$\beta_p = \frac{const}{\lambda^u}. \tag{2.24}$$

Here, u varies from $u = 4$ for point-like particles (purely molecular scattering) to $u = 0$ for big particles [41]. The Ångström exponent is obtained from an empirical fit to the experimental data, so its specific value depends on a specific spectral range or a particular atmospheric condition.

2.3.3 Geometric optics

Light scattering computations of geometric optics are approximations of the fundamental electromagnetic theory. They are used when the dimensions of scatterers are much larger than the wavelength of the incident light so that the size parameter from Eqn. 2.13 is $x \gg 1$. It is based on the assumption that light travels in straight lines, which are a bundle of separate parallel rays. Each ray can be thought of separately and traced on its path, which is affected by the shape and position of objects. Two basic principles of geometric optics can then describe the path of the ray: by the laws of reflection and refraction. The law of reflection, shown in Eqn. 2.25, states that the angle of incidence of a light ray is equal to the angle of reflection and that the incident ray, the reflected ray, and the normal, to the surface of the reflecting object, all lie in the same plane.

$$\Theta_i = \Theta_s \tag{2.25}$$

The law of refraction, shown in Eqn. 2.26 states that the ratio of the sines of the angle of incidence and refraction remains constant for a given pair of media. This constant is known as the refractive index of the second medium with respect to the first medium.

$$\frac{n_1}{n_2} = \frac{\sin(\Theta_2)}{\sin(\Theta_1)} = m \tag{2.26}$$

To describe the scattering coefficient on a particle much larger than the wavelength of light, one must first consider effective cross-section σ_s defined as:

$$\sigma_s = Q_s A_s, \tag{2.27}$$

where Q_s is scattering efficiency and A_s is the geometric size of a scattering particle. Using σ_s and a volume density ρ_s, for a medium containing many scattering particles,

one receives the scattering coefficient as:

$$\beta_s = \rho_s \sigma_s. \tag{2.28}$$

2.3.4 Raman scattering

The energy of individual photons in the laser beam can be described with the means of quantum mechanics, where the energy of a photon only depends on the wavelength of light:

$$E = \frac{hc}{\lambda} = h\nu. \tag{2.29}$$

This quantization is then shown through the interaction between the photon and the particle, as only photons with energies that allow transition in particle energy states can interact with them [42]. When a system absorbs a photon, the energy initially carried by that photon must contribute to a corresponding increase in the internal energy of the system. When a photon is emitted, the system must give up an equivalent amount of its internal energy. The change in internal energy can occur through an increase in the kinetic energy of a particle, a change in the rotational or vibrational energy of a polyatomic molecule, and a change in the electric charge distribution or ionization of a particle.

Similarly to absorption, Raman scattering occurs through a change in a molecule's vibrational or rotational energy, but there is no change in its electronic state. As in this case, the energy of a photon does not need to match the particle excitation transition exactly; the change in energy of a scattered photon occurs. The energy difference between the two states is called the "Raman shift." When the molecule relaxes to its ground state, it releases a photon with a different wavelength than the original. In Raman scattering, the energy of the scattered photon is related to the energy of the incident photon by the following equation:

$$\Delta E = h(\nu_s - \nu_i), \tag{2.30}$$

where ΔE is the energy difference (Raman shift), h is Planck's constant, ν_s is the frequency of the scattered photon, and ν_i is the frequency of the incident photon. This can happen in two possible ways: the Stokes Raman scattering or the Anti-Stokes Raman scattering. In the case of Stokes scattering, the photon transfers energy from a lower energy state of the molecule to above a particular vibrational/rotational state, in which the molecule resides after the interaction. So the scattered photon has a lower energy (longer wavelength) than the incident photon, resulting in a positive Raman shift as the molecule's energy increases. The shift in the energy of a photon is the same as the difference between the molecule's initial and final energy state. This can be described by the following equation:

$$h\nu_s = h\nu_i - \Delta E. \tag{2.31}$$

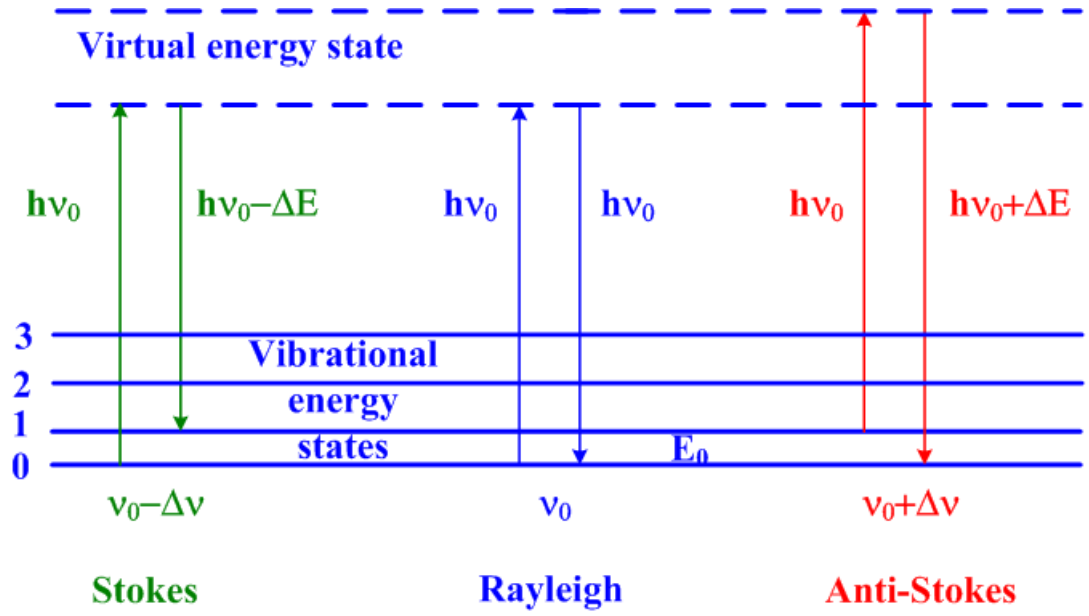

Figure 2.4: Elastic Raman scattering involves no change in energy or vibrational state of the molecule. Stokes Raman scattering results from the excitation of a molecule's vibrational mode, causing the molecule to absorb some of the energy from the incident photon. The energy difference between the incident and scattered photons corresponds to the energy of the vibrational mode. Anti-Stokes Raman scattering occurs when a molecule is already in a higher vibrational energy level, resulting in the scattered photon having more energy than the incident photon. The figure is taken from [43].

In the case of anti-Stokes scattering, the molecule already resides on some higher energy level, and during the scattering process, it moves to a lower energy level. This results in an increase of energy (shorter wavelength) on the scattered photon with respect to the incident photon, resulting in a negative Raman shift as the molecule loses energy. This can be described by the following equation:

$$h\nu_s = h\nu_i + \Delta E. \tag{2.32}$$

It is worth noting that Raman scattering is a relatively weak effect, and typically, a large number of photons must be used to detect the Raman signal. In addition, the Raman scattering cross-section depends on the molecule's vibrational and rotational states and polarizability.

2.4 Polarization

In linearly polarized electromagnetic waves, electric field vectors oscillate in the same plane during wave propagation, as shown in Fig. 2.2 [44]. In elastic scattering, only

linear processes are involved [35, 45], so electric fields transform as:

$$\vec{E}^s = \mathbf{A}\vec{E}^i. \tag{2.33}$$

i stands for the incident and s for scattered wave, $\vec{E}$ stands for the electric vector, which is divided into two components, one parallel $E_{\parallel}$ and one perpendicular $E_{\perp}$ to a reference plane,

$$\vec{E} = \begin{bmatrix} E_{\perp} \\ E_{\parallel} \end{bmatrix}. \tag{2.34}$$

A denotes the transformation matrix from the incident into a scattered wave,

$$\mathbf{A} = \begin{bmatrix} A_{11} A_{12} \\ A_{21} A_{22} \end{bmatrix}. \tag{2.35}$$

Values of the matrix **A** elements are related to quantities associated with the medium, through which the EM wave propagates (shape, size, orientation, and optical properties of particles that consist of the medium) and govern how much the polarization of the scattered rays will change during the collision. If the particles are smaller than the wavelength of the incident light, they can be treated as dipoles [45]. Spherical dipoles preserve the polarization of the incident light, while an irregular dipole partially depolarizes the backscattered radiation due to its asymmetry [46]; the description of particles of similar sizes as wavelengths can be done using geometric optics and changes in incoming and outgoing ray angles with scatterers. The light scattering on spherical particles retains its polarization due to the symmetry of a particle. Both the edge ray and the central ray get reflected by 180°, with the ray staying in the same reference plane as shown in Fig. 2.5. Similarly, scattering on nonspherical particles with reflectional symmetry regarding the scattering plane (the particle is identical to its mirror image as seen by the scattering plane; $A_{12} = A_{21} = 0$), will not cause depolarization of an electromagnetic wave, which has an electric vector parallel or perpendicular to the scattering plane [47]. In all other cases, the ray penetrating the nonspherical particle will undergo several reflections; during this, some energy is lost through refraction. A consequence of this is that too many internal reflections reduce the backscattering signal to be non-detectable. While the amount of internal reflections is small enough to produce a visible signal, the new electric vector has to be rotated to the initial coordinate, which produces depolarization of the electromagnetic wave. In addition, depolarization can be created in an optically thick medium when a ray bounces from several particles (multiple scattering), which, similarly to before, changes the scattering plane on every bounce. One of the crucial roles in detecting depolarization is played by absorption. As depolarization is created due to the internal reflections of a ray, aerosols with high absorption at the wavelength of the incoming light ray will dampen the backscattering of the ray.

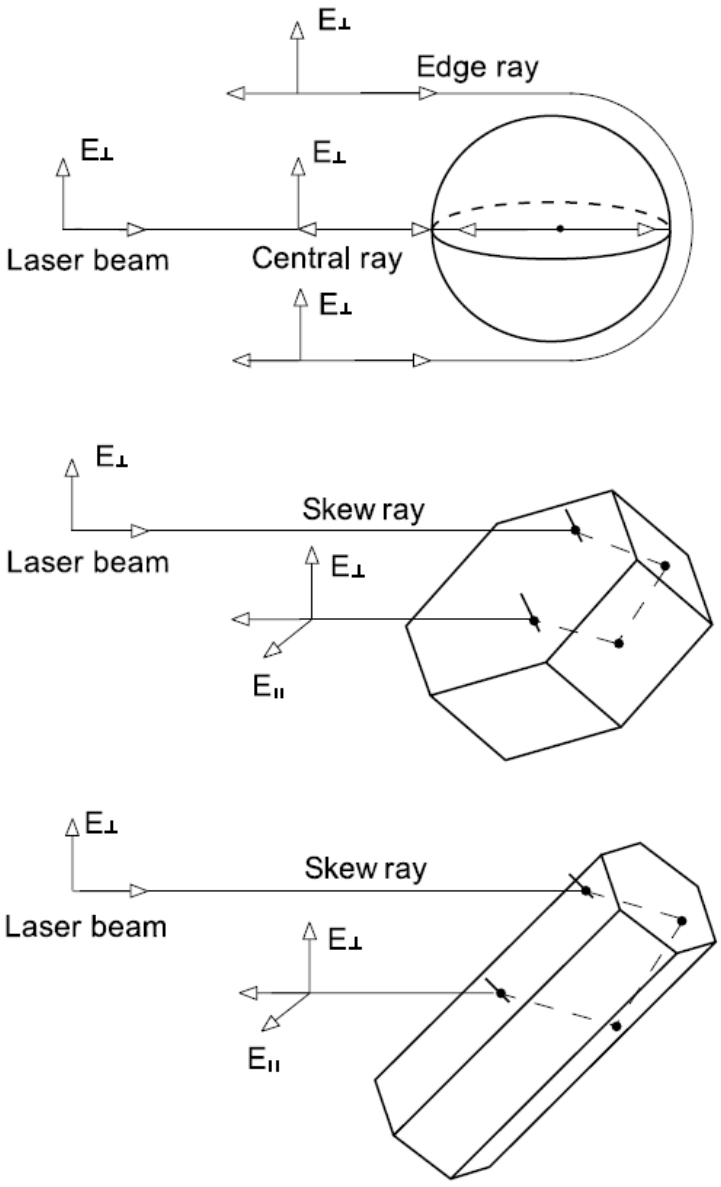

Figure 2.5: The laser emitted ray backscattering on a spherical droplet, a hexagonal plate, and a column, which are much larger than the wavelength of a ray. The geometrical symmetry of a sphere preserves wave polarization. At the same time, the nonspherical particles produce the cross-polarization component for all the light rays that are not perpendicular to the major axis of particles. The figure is taken from [35].

3

Light detection and ranging - LIDAR

Lidar (Light detection and ranging) is a remote sensing method that uses visible and near-to-visible light to measure atmosphere parameters. It operates on the same principle as radar, transmitting a beam of electromagnetic radiation and then detecting any backscattered radiation. As it is a similar technique, it is natural that its development started in parallel with the advancement of radar development in the 1930s, with some attempts to use visible light for measurements of air density profiles [48, 49] instead of radio waves. Even though they had some success with the use of search-light beams [50], the rapid development of lidars really started at the beginning of the 1960s with the invention of laser [51, 52]. The new technology was soon adapted for atmospheric monitoring purposes [53]. In the following decades, lidar technology continued to evolve and improve, leading to more advanced lidar instruments that could measure a broader range of atmospheric parameters, becoming essential tools for atmospheric observations and aerosol measurements [54]. For example, at the end of the 1960s, Raman lidar was developed [55, 56], which could be used to measure the concentration of gases like nitrogen, water vapor, and ozone. In the 1980s and 1990s, lidar technology was used extensively for studying the atmosphere and its variability. Many lidar instruments were developed and deployed in different parts of the world for this purpose. Measurements with high spatial and temporal resolution allow for detailed monitoring of quick changes on small scales from the ground throughout the atmosphere, with a signals reaching more than 100 km distance from the device. The possibility to detect signals from different interactions between light and atmospheric medium provides an opportunity to determine basic atmospheric variables, such as humidity, wind, and temperature, as well as aerosol loading distributions, aerosol composition, and detection of trace gases. The capability of detecting certain atmospheric properties depends on the device's design, especially the wavelengths, which can be measured by the detector [57]. The detector can measure three general configurations of channels: elastic channels, Raman channels, and depolarization channels. The most straightforward configuration is a lidar with a single elastic channel, where the detector only detects an elastically backscattered signals of emitted light. This

gives the capability to collect information about atmospheric structures, e.g., PBL height, lofted layer base, top and thickness, and cloud base, top and thickness, as well as some information about atmospheric optical properties (e.g. backscattering coefficients). We can also gain effective aerosol size distribution information using at least two elastic channels. Adding a Raman channel (the measured wavelength is shifted relatively to emitted one due to the Raman effect) allows measurement of the extinction coefficients. With at least two Raman channels and three elastic channels, one can infer even more aerosol properties, such as the single scattering albedo, the mass concentration, and the refractive index. Adding a corresponding depolarization channel to an elastic channel can provide information on aerosol shapes. As shown in the above examples, lidar tackles atmospheric parameters and allows us to assess a wide assortment of aerosol microphysical parameters that would otherwise only be possible to determine through *in situ* sampling.

3.1 Typical lidar setup

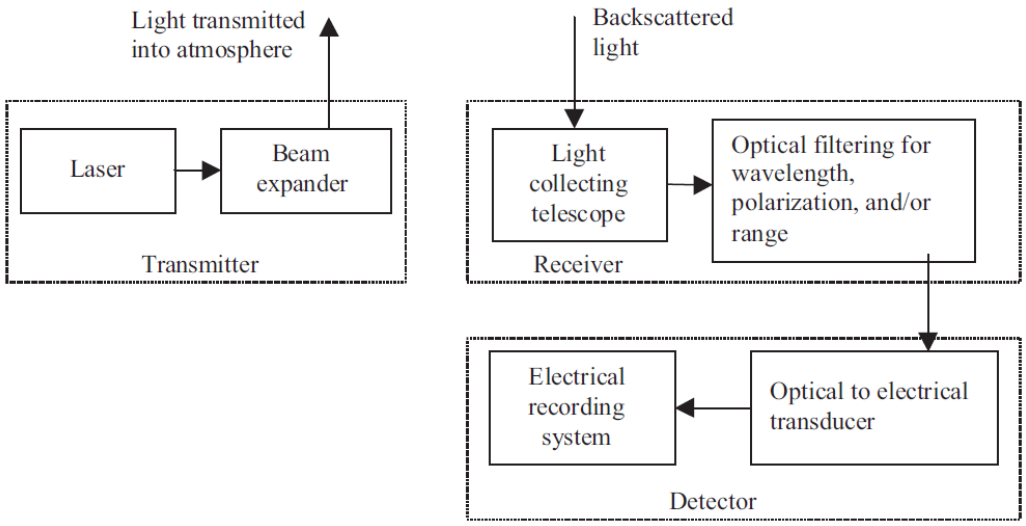

Figure 3.1: Schematic setup of a typical lidar system. The figure is adopted from [58].

Any lidar must have a transmitter, a receiver, and a detection-retrieval system to be operational(see Fig. 3.1). The geometric setup of the transmitter and the receiver has a strong influence on lidar operation. It is especially true for lidars with near-range observation capabilities [54]. Depending on the setup, they can be separated into three different classes: monostatic coaxial, monostatic biaxial, and a bistatic configuration, as shown in Fig. 3.2 [58, 59]. The bistatic configuration was primarily used in the past [50] when searchlights were used to shine to the sky, and the receiver had to scan along the transmitted beam to obtain an altitude profile of the scattered light. Now, most lidars are monostatic, with the transmitter and receiver in the same location. In a coaxial system, the laser beam is emitted along the optical axis of the receiver

telescope, which allows better near-range coverage of the return signal, while in the case of a biaxial system, the laser light must first enter the telescope's field of view, for it to collect the backscattered light, which can happen several hundred meters away from the device. This detected lidar signal is described with a single–scattering lidar

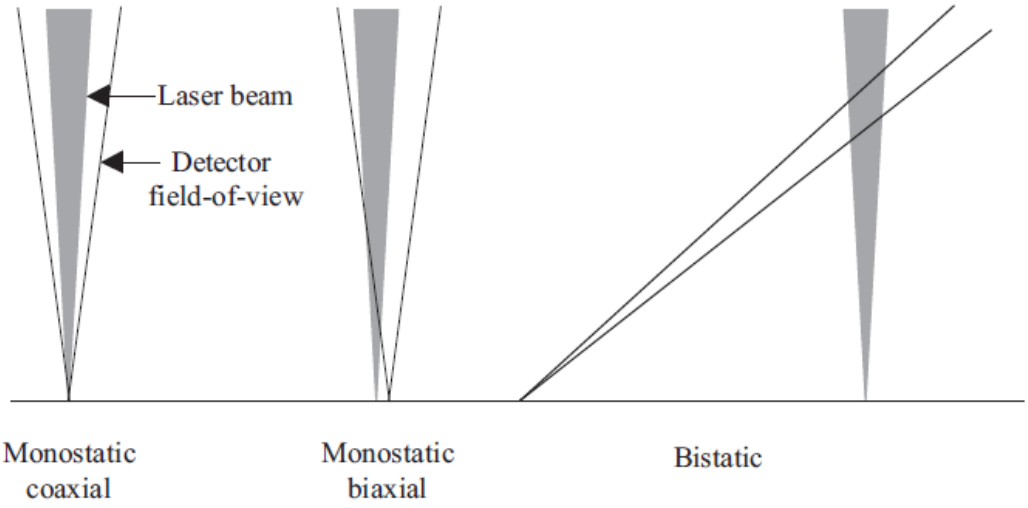

Figure 3.2: Three possible configurations of a lidar transmitter field of view and receiver field of view. The figure is adopted from [58].

equation as

$$P(\lambda_0, z) = CP_0 \frac{O(z)}{z^2} \beta(\lambda_0, z) \exp\left[-2\int_0^z \alpha(\lambda_0, z')dz'\right], \tag{3.1}$$

where $P(\lambda_0, z)$ is a received backscattered power from distance z, P_0 is a power transmitted by laser, C is the system constant that accounts for the transmission of the receiver unit, $O(z)$ is an overlap function, while $\alpha(\lambda_0, z)$ and $\beta(\lambda_0, z)$ are extinction and backscattering coefficients respectively. The first part of lidar equation is system related (P_0, C and $O(z)$) and the second part is atmosphere related ($\alpha(\lambda_0, z)$ and $\beta(\lambda_0, z)$). In order to calculate atmospheric backscattering and extinction coefficients from the total measured backscattered power, the system part of the equation has to be known precisely. P_0 and C depend on the collection efficiency of optical components and can be measured in the laboratory. On the other hand, the overlap function depends on the geometry of the whole device, so in most cases, it can be given only as an estimate. There is a possibility that it can be obtained experimentally using the Raman signal method [60].

3.1.1 Transmitter

As the name states, lidar is a device that uses light for measurements. Even though different sources were used historically, all new lidars are based on laser technology.

Two main types of laser sources are used in atmospheric lidar systems: solid-state lasers and gas lasers.

- **Solid-state lasers:** These lasers use solid materials as the active medium, such as Nd:YAG, ruby, or diode lasers. They are compact, reliable, and easy to operate, making them popular for various applications. Solid-state lasers can be operated in a continuous wave (CW) or a pulse mode and are can emit laser light at various wavelengths, including ultraviolet, visible, and near-infrared.
- **Gas lasers:** These lasers use gas as the active medium, such as CO2, He-Ne, or CO. They can generate high-power laser light at specific wavelengths, mainly in the infrared region.

Both solid-state and gas lasers have advantages and disadvantages, and the choice of laser source depends on the specific requirements of the atmospheric lidar system. For example, solid-state lasers are preferred for their compact size and ease of operation, while gas lasers are favored for their high power. Modulators (usually already part of the laser system) can control the laser intensity, pulse length, and pulse duration. This is crucial for the performance of tasks in different environments, as in some cases, intense laser pulses might be dangerous and high repetition, weak laser pulses over a long integration time might be necessary to achieve a greater range. The laser is does not fire directly into the atmosphere for most lidars. However, the beam travels through several optical elements, such as guiding mirrors to change beam direction, beam splitters, and collimators for shape control, and polarizators to achieve 100% linear polarization of a laser beam.

3.1.2 Receiver

The atmospheric lidar receiver is an essential component of a lidar system responsible for detecting the laser light that atmospheric particles have scattered. The receiver collects the scattered light and directs it to the detector, converting it into an electrical signal that can be processed and analyzed. The primary mirror's size strongly influences the lidars sensitivity and is crucial for achieving good signal collection for distances far from the device. The mirror design is further influenced by the design of the lidar itself, e.g., the mobile lidars size needs to accommodate handling and transportation. The second important feature of the lidar detector is the polychromator, which splits the collected light into separate wavelengths. Typically, it is comprised of several beam splitters and narrow band filters, which allow only a specific wavelength of light to enter the detector.

3.1.3 Detection and recording

When the light crosses the polychromator, it is directed toward a photodetector, where the photodetector photomultiplier tubes (PMTs) or avalanche photodiodes (APDs) are

used. PMTs have a higher gain than APDs, meaning they can amplify the signal to a greater extent. This allows PMTs to detect weaker signals than APDs. However, this higher gain also makes PMTs more sensitive to noise. Both high gain and high light sensitivity make PMTs perfect candidates for long-range lidar measurements and the detection of low signal scatterings, such as Raman scattering. On the other hand, APDs have a faster response times than PMTs, meaning they can be used for high-resolution timing measurements, e.g., lidars on board of planes. The signal received from the photodetector can be further amplified electronically and converted from analog to digital using an analog-to-digital converters. These are often available as a single electronic devices (i.e., a transient recorder), which are commonly especially designed for use with PMTs and APDs and provide, along analog signal recording, also a channel for photon count detection. This is useful in lidar data analysis for correcting low signal measurements at the far end of lidar detection range. The digitized data from a transient recorder is then sent to a computer for storage and further processing.

3.2 Raman lidar

From a signal collected by a purely elastic lidar, it is impossible to distinguish between the backscatter coefficient and extinction coefficient without additional assumptions [57]. This is a problem because the lidar ratio, ratio between the backscattering and extinction coefficient, provides information about the composition of aerosols but has to be explicitly assumed, to measure both coefficients. A workaround is the implementation of a channel that can measure the weak inelastic (Raman) scattering 2.3.4 from an abundant atmospheric species of molecules, such as N_2 or O_2 with well-defined proportions in the atmospheric composition [55, 61, 62, 63, 64]. This can be done because the Raman backscatter coefficient of the reference gas is known, then the lidar equation can be solved for the unknown particle extinction coefficient. As N_2 (and O_2 for more detailed measurement) accounts for the vast majority of the gas in the atmosphere, the subtracted extinction coefficient belongs solely to aerosol extinction. Lidars with multiple Raman channels are used for the measurement of Raman signals with less abundant gases, such as water vapor [65, 66, 67], carbon dioxide [68] and sulfur dioxide [68]. These studies have a different success rate, mainly dependent on abundance and current atmospheric conditions, and only reaching low measurement ranges (the exception being water vapor mixing ratio measurements [54]. The small Raman scattering cross section has previously limited Raman lidar operations to nighttime. However, technical advancements, specifically introducing high-powered transmitters and narrow-bandwidth detection systems, sufficiently reduced the daytime background and allowed daytime application [69, 70, 71]. The Raman scattering mechanism excites the rotational and vibrational states of air molecules in the atmosphere. In contrast to the differential absorption (DIAL) lidar technique, the Raman technique does not require specific laser wavelengths. However, shorter emission wavelengths are preferred because of Raman scattering cross-section wavelength de-

pendence λ^{-4}. One of the other possible uses of Raman measurements are temperature measurements. Rotational Raman (RR) lidar can measure temperature in clear air, aerosol layers, and optically thin clouds [54, 72]. This is due to the differences in temperature dependencies of the line within the rotational Raman band. Lines near the incident laser line decrease in intensity with rising temperature, while those with more significant wavelength differences increase. This is comes from the Maxwell-Boltzmann distribution of rotational energy levels. The ratio of two RR lidar signals with opposite temperature dependencies gives a temperature-dependent value unaffected by atmospheric transmission and range. Unlike the integration method, the RR technique does not require the assumption of hydrostatic equilibrium, so there are no systematic measurement errors in turbulent layers. The rotational Raman technique can also be used in the presence of particles because the particle backscatter signal has the same wavelength as the laser. However, for accurate results in clouds, the transmission of elastic-backscatter light in the RR channels must be low (10^{-7}). This was a challenge due to the proximity of the rotational Raman line signals to the laser wavelength. However, it has been overcome with the use of advanced optical components in the receiver.

3.2.1 Raman signal analysis - backscatter and extinction coefficients

The combination of Rayleigh and nitrogen Raman signal allows direct measurements of aerosol extinction and backscatter coefficients without making any assumptions on the lidar ratio [43, 61, 63]. For a Raman lidar, the lidar equation has to be rewritten as:

$$P(z,\lambda_0,\lambda_R) = CP_0\frac{O(z)}{z^2}\beta(z,\lambda_0,\lambda_R)\exp\Big[-\int_0^z(\alpha(\lambda_0,z')+\alpha(\lambda_R,z'))dz'\Big], \tag{3.2}$$

where all the factors have the same meaning as in Eqn. 3.1, except the terms with R subscript which are directly connected to the Raman wavelength. The backscattering coefficient is linked to the differential Raman backscatter cross-section of a gas molecule number density N as follows:

$$\beta(z,\lambda_0,\lambda_R) = N(z)\frac{d\sigma(\lambda_0,\lambda_R,\pi)}{d\Omega}. \tag{3.3}$$

Since the number densities of nitrogen and oxygen are usually known as well as used wavelengths ($P(z) \equiv P(z,\lambda_0,\lambda_R)$), the Eqn. 3.2 and 3.3 can be rewritten to:

$$\alpha(\lambda_0,z)+\alpha(\lambda_R,z) = \frac{d}{dz}\Big[ln\frac{O(z)N(z)}{z^2P(z)}\Big]. \tag{3.4}$$

This can be further reduced as $O(z)$ reaches unity at the full overlap between the laser beam and telescope fields of view. The total extinction can be rewritten as a combination of aerosol and molecular parts as follows:

$$\alpha(\lambda_{0,R},z) = \alpha_{mol}(\lambda_{0,R},z)+\alpha_{aer}(\lambda_{0,R},z), \tag{3.5}$$

where:

$$\alpha_{aer} = \alpha_{aer}(\lambda_0, z) + \alpha_{aer}(\lambda_R, z) = \frac{d}{dz}\left[ln\frac{O(z)N(z)}{z^2P(z)}\right] - \alpha_{mol}(\lambda_0, z) - \alpha_{mol}(\lambda_R, z). \tag{3.6}$$

The aerosol extinction coefficient can be obtained as:

$$\alpha_{aer}(\lambda_0, z) = \frac{\frac{d}{dz}\left[ln\frac{O(z)N(z)}{z^2P(z)}\right] - \alpha_{mol}(\lambda_0, z) - \alpha_{mol}(\lambda_R, z)}{1 + \left(\frac{\lambda_0}{\lambda_R}\right)^u}, \tag{3.7}$$

where u is the Ångström exponent between wavelengths λ_0 and λ_R (between 0 and 2 for most aerosol types), while the molecular extinction coefficients $\alpha_{mol}(\lambda_0, z)$ and $\alpha_{mol}(\lambda_R, z)$ can be directly calculated from pressure and temperature profiles. With known extinction coefficients, also the aerosol backscattering can be calculated:

$$\begin{aligned}\beta_{aer}(\lambda_0, z) = \beta_{mol}(\lambda_0, z) + [\beta_{mol}(\lambda_0, z_0) + \beta_{aer}(\lambda_0, z_0)]\frac{P_R(z_0)P_{Mie}(z)\beta(\lambda_R, z)}{P_R(z)P_{Mie}(z_0)\beta(\lambda_R, z_0)} \\ \times\frac{exp\left[-\int_z^{z_0}(\alpha_{aer}(\lambda_0, z') + \alpha_{mol}(\lambda_0, z'))dz'\right]}{exp\left[-\int_z^{z_0}(\alpha_{aer}(\lambda_R, z') + \alpha_{mol}(\lambda_R, z'))dz'\right]}.\end{aligned} \tag{3.8}$$

The height z_0 is called a reference height and is usually chosen at the altitude where the molecular backscatter is dominant. Aerosol backscatter at this height is estimated using extinction coefficients at a same height, while molecular backscattering profiles $\beta_{mol}(\lambda_0, z)$ and $\beta_{mol}(\lambda_R, z)$ can be calculated with the use of atmospheric pressure and temperature profiles. Knowing both aerosol backscattering and aerosol extinction, we can finally calculate the lidar ratio:

$$LR(\lambda_0, z) = \frac{\alpha_{aer}(\lambda_0, z)}{\beta_{aer}(\lambda_0, z)}. \tag{3.9}$$

3.3 Polarization lidar

Lidars that detect the change in polarization of backscattered light use transmitters with completely linearly polarized laser pulses. The detected signal is split into two components, one with the polarization plane parallel and one orthogonal to the plane of polarization of the outgoing beam [54]. Their ratio is referred to as the linear depolarization ratio and can be obtained after applying corrections for differences in the optical and electronic gains of the two channels. As shown in Chapter 2.4, the emergence of depolarization results from scattering on nonspherical or inhomogeneous particles, making polarized lidar a perfect tool for determining aerosol shape. In combination with the measurements of the Ångström exponent and lidar ratio, the depolarization ratio provide a very accurate tool for aerosol composition measurements [43].

3.3.1 Pure molecular scattering

The typical molecular size is usually much smaller than the lidar wavelength, so the Rayleigh scattering applies. Molecular backscattering is applicable for the near-ultraviolet and visible light channels and produces depolarization within values of about a few percent [73, 74, 75, 76, 77]. Due to the small percentage of depolarization, it is necessary to take into account for clean air measurements. However, it can be neglected for cloud measurements and heavy aerosol pollution (such as soot, sand, volcanic ash, and marine aerosols).

3.3.2 Aerosol scattering

Aerosols are a combination of wet and dry particles of natural (wildfires, haze, volcanic emission, wind-risen dust) or anthropogenic origin (smoke, soot, vehicle emission) [43, 78]. Due to aerosol type diversity, their shape and size vary considerably. In turn, the return signal spans from Rayleigh (molecular cluster-sized particles) to the geometric optics scattering domain (dust, soot), and due to their shape differences, the depolarization produced by particles varies. There is little or no depolarization for deliquesced and other spherical aerosols. The depolarization at irregularly shaped particles strongly depends on their size parameter [79, 80] and, to a degree, on a refractive index at the laser wavelength. If particles are too absorbing, there is no depolarization expected. Similarly, very low depolarization values are expected in cases when an aerosol acts as a core for a liquid shell [80, 81, 82, 83].

3.3.3 Water cloud scattering

Lorentz-Mie scattering theory shows that we only get front and rear surface reflection under spherical symmetry though this mechanism does not produce any depolarization [54, 84, 85]. In a water cloud, depolarization usually increases with laser pulse penetration depth; this arises from near-perfect backward photon scattering on more than one droplet [86]. This multiple scattering builds up depolarization, and the lidar return signal consists of a mixture of primary scattered polarized light and multiply scattered depolarized light. Depolarization increases with cloud depth because the effect of primary scattering decreases as the laser pulse attenuates while multiple scattering accumulates. This inverse relationship means that the depolarization created by water clouds will generally be greater than theoretical predictions (and clear-sky measurements) but will still be smaller than mixed-phase and ice-cloud measurements.

3.3.4 Ice cloud scattering

The depolarization in ice clouds varies depending on the shape and orientation of ice crystals in the cloud [54, 87]. The targeted depolarization ratios span from 30% to 70% on pure ice clouds [84, 88]. A significant difference between the depolarization of

different types of ice crystals is expected due to their wide range of shapes and sizes. For example, depolarization on hexagonal ice crystals increases with the crystal's length from a thin plate toward a long column. Although this may seem helpful for inferring the composition of ice clouds, ice crystals often show hollow, complex spatial, and irregular or rounded shapes, which prevents direct determination of their shapes just from the depolarization ratio. Moreover, the typical situation in clouds involves a diverse mixture of ice crystal types caused by a combination of physical cloud processes, including new ice crystal nucleation, vertical transport, and ambient growth/evaporation conditions.

3.3.5 Mixed phase clouds

The true value of polarization lidar is shown in mixed-phase cloud studies [54, 89]. From the depolarization measurements it is possible to distinguish between layers of supercooled water, layers of ice crystals, and layers of mixed composition. The advantage of lidar is also in detecting particles in virga, where even the best (shortest wavelength) microwave radar measurements fail due to the particle's smaller size and low density. It would appear that the lidar's high susceptibility to multiple scattering and its limited ability to penetrate optically thick clouds result in a penetration depth on the order of tens to hundreds of meters.

3.3.6 Depolarization analysis

The depolarization ratio is the ratio between the backscattered power of two orthogonally polarized Mie-Rayleigh channels operating at the same wavelength [43]. The plane of polarization of one of the channels is parallel to the laser polarization plane, while the plane of polarization of the other channel is perpendicular to it. The particle depolarization ratio plays an important role in investigating aerosol shape since it differs significantly regarding the geometries of observed particles. Known value ranges of particle depolarization ratios for certain aerosols can be used to distinguish their types in lidar return signals [54]. To determine the volume polarization ratio, which includes both molecular and aerosol contributions, the lidar equation 3.1 has to be written for each plane of polarization separately [90]:

$$P^{\parallel}(\lambda_0, z) = C^{\parallel} P_0^{\parallel} \frac{O^{\parallel}(z)}{z^2} \beta^{\parallel}(\lambda_0, z) \exp\left[-2 \int_0^z \alpha^{\parallel}(\lambda_0, z') dz' \right], \tag{3.10}$$

$$P^{\perp}(\lambda_0, z) = C^{\perp} P_0^{\perp} \frac{O^{\perp}(z)}{z^2} \beta^{\perp}(\lambda_0, z) \exp\left[-\int_0^z \{\alpha^{\parallel}(\lambda_0, z') + \alpha^{\perp}(\lambda_0, z')\} dz' \right]. \tag{3.11}$$

The volume depolarization ratio can then be written as

$$\delta_V = K \frac{P^{\perp}}{P^{\parallel}} = \frac{\beta^{\perp}}{\beta^{\parallel}} \exp(\tau^{\parallel} - \tau^{\perp}), \tag{3.12}$$

where K is the relative amplification of the two channels

$$K = \frac{C^{\parallel} P_0^{\parallel}}{C^{\perp} P_0^{\perp}}, \tag{3.13}$$

which depends on the detector and is determined by calibration. Atmospheric transmission τ usually does not depend on the polarization of light ($\tau^{\parallel} = \tau^{\perp}$); therefore the volume depolarization ratio can be split into separate components (molecule and aerosol depolarization) and rewritten as

$$\delta_V = \frac{\beta^{\perp}}{\beta^{\parallel}} = \frac{\beta_m^{\perp} + \beta_p^{\perp}}{\beta_m^{\parallel} + \beta_p^{\parallel}}. \tag{3.14}$$

The components of the volume depolarization ratio need to be separated to receive a particle depolarization ratio, and then the equation can be solved for δ_p

$$\delta_p = \frac{(\beta_m^{\parallel} + \beta_m^{\perp})(\delta_V - \delta_m) + \delta_V(\beta_p^{\parallel} + \beta_p^{\perp})(1 + \delta_m)}{(\beta_m^{\parallel} + \beta_m^{\perp})(\delta_m - \delta_V) + (\beta_p^{\parallel} + \beta_p^{\perp})(1 + \delta_m)}. \tag{3.15}$$

Lidar measurement can obtain the volume depolarization ratio and the particle backscattering coefficient directly. In contrast, the molecular backscattering coefficient needs to be obtained with radiosonde data measurements or from atmospheric models.

4

The Raman lidar for the CTA observatory at La Palma

The Barcelona Raman Lidar (BRL)[1] [31, 91] is one of two Raman lidars (the other being the Laboratoire Univers et Particules de Montpellier (LUPM) lidar [29, 31], designed as prototypes for the future Raman lidar for Cherenkov Telescope Array Observatory (CTAO). Both prototypes provide scanning capabilities in azimuth and zenith and can be operated remotely. BRL was awarded the status of a CTAO Raman Lidar Pathfinder in 2019, implying its potential for future permanent inclusion into the CTAO North observatory. Even though the new official name is the CTAO-North Raman Lidar Pathfinder, for the sake of convenience, the system will be, in most cases, referred to by its original name, the Barcelona Raman Lidar.

4.1 Main components

The BRL is a custom-made lidar with the specific task of providing information about Cherenkov light transmissivity of the atmosphere above the northern site of CTAO. The demanding requirements of the CTAO, like 30 km elastic line range and 20 km Raman line range, require the device to be pushed to extremes regarding its size and strength.

4.1.1 Transmitter

The laser used in the BRL is a QUANTEL Brilliant Nd:YAG 1064 nm. It is a pulsed 10 Hz with a base wavelength of 1064 nm, while for the purpose of a lidar a second (532 nm) and third (355 nm) harmonics are included, respectively, providing 160 mJ and 70 mJ energy per pulse. The harmonic generation is made with highly deuterated KDP crystals (KD_2PO_4) cut at the proper angle for the required wavelengths. They are assembled in compact modules, including the non-linear crystals and a removable set of dichroic mirrors (Fig. 4.2). Phase matching for the second and third harmonics is obtained by mechanical adjustment. Each crystal is temperature stabilized in a

[1] http://ctan-lidar-pathfinder.ung.si/

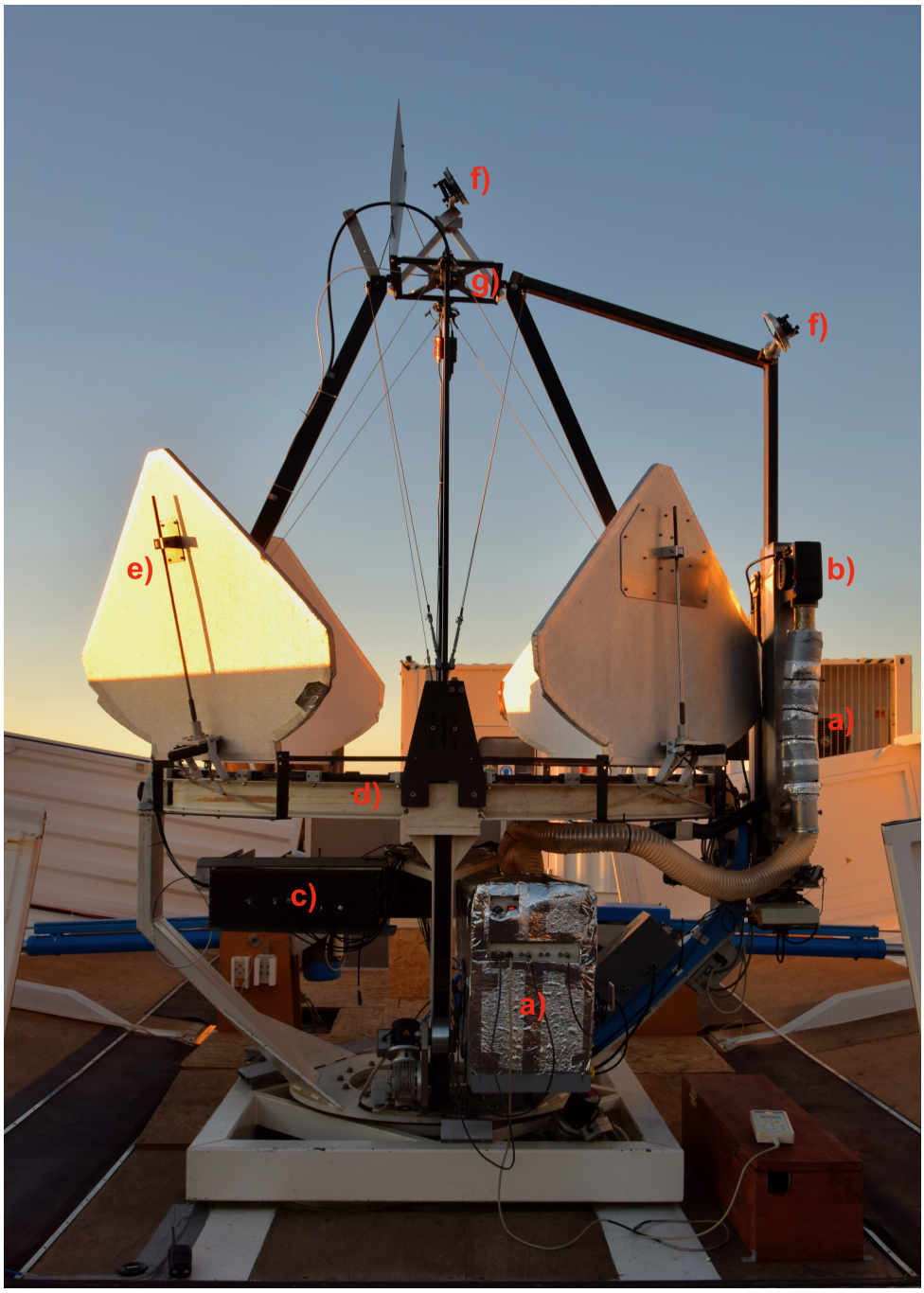

Figure 4.1: The BRL deployed for operation at the LST-1 site, Roque de los Muchachos Observatory, La Palma, in August 2021. Highlighted are the following lidar components: (a) laser power and laser head, (b) heater for laser operation under cold ambient temperature conditions, (c) polychromator, (d) main mirror, (e) petals, (f) guiding dichroic mirrors for the transmitter and (g) shutter for the optic fiber.

sealed-off cell, ensuring long-term energy stability. Cell windows are anti-reflection coated at the appropriate wavelengths.

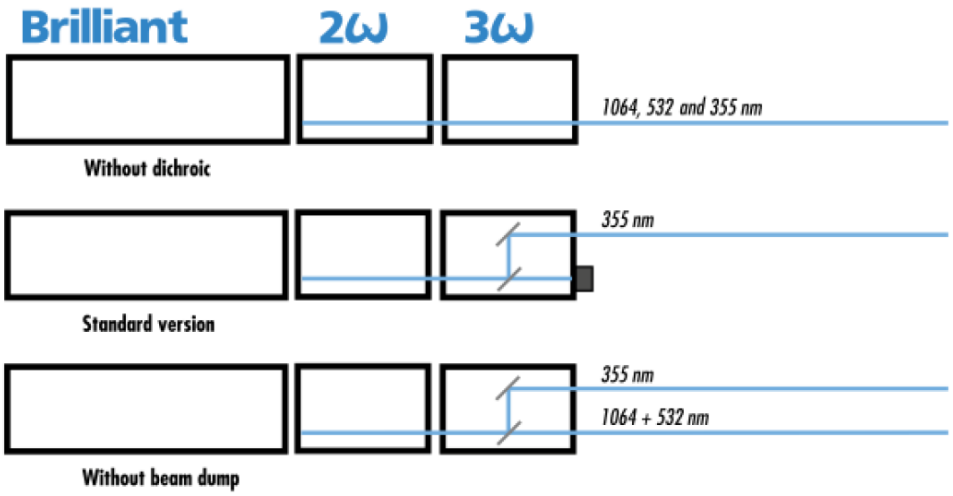

Figure 4.2: Different harmonic configurations for the laser output. Using both second and third harmonics generators without dichroic mirrors provides all three output wavelengths (1064 nm, 532 nm and 355 nm) at the same hole (upper sketch). While with dichroics, the 355 nm line can be split apart from the other two lines, and depending on the setting of the beam dump, one can remove the first and second lines (middle sketch) or have a third line beam firing from a different hole as the first two (lower sketch). Figure acquired from Quantel[2].

A coaxial setup is employed to reduce the overlap of field of view distance for BRL. It differs from the standard monostatic coaxial setting because it has a laser arm next to the telescope. The laser beam is directed in front of the telescope via two dichroic guiding mirrors to achieve coaxial configuration(Fig. 4.1f), that way, the laser beam coincides with a telescope's optical axis. The mirrors are designed in such a way that they have high reflectivity for 355 nm and 532 nm wavelengths and a very low reflectivity at 1064 nm to protect the liquid light guide (a polymer tube with a liquid core, that carries light in a manner similar to fiber optic cables) from strong infrared light. The guiding mirrors reflect light at an angle $61.1^\circ \pm 0.3^\circ$ instead of at 90° to reduce the space requirements to change a laser beam's direction.

4.1.2 Receiver

The BRL has a 1.8 m diameter primary mirror with an f-number of 1 (Fig. 4.1d). It was produced for the CLUE experiment (Cherenkov Light Ultraviolet Experiment) in Padova [92] with a slumping technique developed at CERN [93, 94]. It was made from

[2] https://www.quantel-laser.com/

float glass with an exceptionally smooth surface, produced in Venice, Italy (*Società Italiana Vetri of Porto Marghera*). The reflective coating of vacuum-evaporated 80 nm thick aluminum was performed in Asiago, Italy (*Osservatorio Astrofísico of the University of Padova*). The roughness of the mirror is 2–3 nm with an initial reflectivity of 95%. After four years of operation, the mirror was re-coated at La Palma, Spain (*Herschel observatory*), because its reflectivity has degraded to 50-60%. A final realuminization, this time including protective coating, was performed in Milan, Italy (*ZAOT s.r.l.*) at the end of 2020, before shipping the lidar to La Palma. In order to further increase the dynamic range of the system, special custom-designed near-range optics have been developed. While the primary lidar optics provide access to distance ranges greater than $\sim$150 m, the near-range optics cover 20 m to $\gtrsim$200 m distance in the lidars field of view. At present, the near-range optics can be used only for the elastic scattering 532 nm channel.

The light collected with the primary mirror is transported to the polychromator by a Lumatec Series 300 liquid-light-guide (LLG, length of 3.2 m and diameter of 8 mm). Its peak transmission value is up to 80% and covers a spectral range from 320 nm to 650 nm, within which there is no optical degradation of transmitted radiation. The maximum incidence angle of reflected light into the LLG is $\sim$30°. In order to reduce background, light coming from angles $>$30° must not be transmitted through the LLG. The LLG has a numerical aperture of 72°, perfectly matching the incoming light angle requirements [95].

The polychromator splits the light transmitted through the liquid-light-guide into four read-out channels: two to analyze the elastic-backscatter light at 355 nm and 532 nm and two for the Raman Nitrogen backscattered light, at 387 nm and 607 nm [96]. After collimation by 100 mm lens couples (LC), the incoming light is directed towards its respective detector with the help of three dichroic mirrors [31]. In each channel, the light is again focused by LCs and noise-reduced by 10 nm wide interference filters. Finally, each of the four wavelengths is collected by a 1.5 inch, high quantum efficiency PMT of type Hamamatsu R11920, the same as those used for the Large-Sized-Telescope camera [97].

4.1.3 Movement and protection components

The BRL itself is enclosed in a standard 20 ft shipping container that protects the device and the accompanying instrumentation from environmental influences. When the lidar is in operation, the container is open, which is achieved by two *Servomech* linear actuators powered by a 1.5 kW IEC standard motor. The movement of the motors is controlled manually or remotely through a licli (lidar client software) control interface. While the maximum movement range and correct order of the movement procedure are also guaranteed physically by several switches, some also prevent the container's closure if the telescope is not in parked position. The container can be opened or closed completely within one minute.

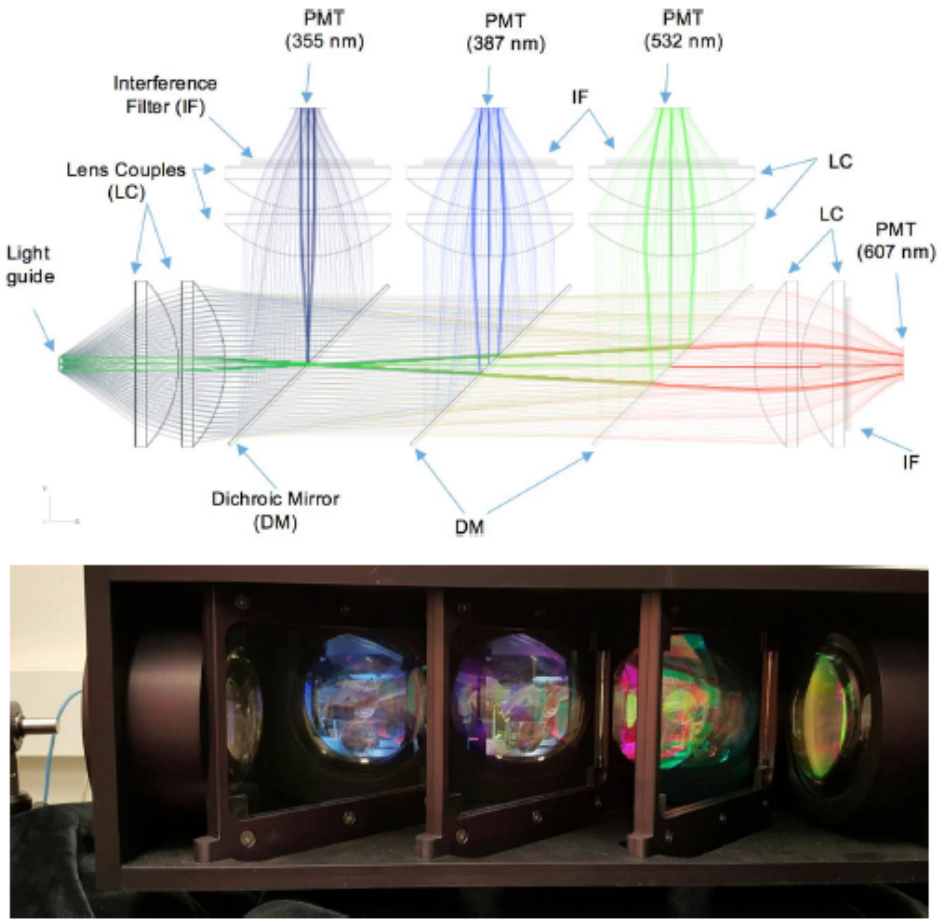

Figure 4.3: **Top:** The Zemax design of the BRL polychromator. **Bottom:** A picture of the polychromator taken from the bottom side. After collimation by 100 mm lens couples (LC), the incoming light is directed towards its respective detector with the help of three dichroic mirrors (DM). For each channel, the light is again focused by Lens Couples and the noise is reduced by 10 nm wide interference filters (IF). Each of the four wavelengths is then collected by a 1.5 in high-quantum-efficiency Hamamatsu R11920 photomultiplier tubes (PMT), which are of the same type same as those used in the Large-Sized-Telescope camera [31].

The telescope is placed on a custom-made chassis on an alt-azimuth mount, allowing zenith and azimuth angle movements. The chassis also holds the petals and supports the laser arm and the optical system in the focal plane. The four polystyrene petals protect the primary mirror from any possible damage while working around the telescope and prevent sunlight reflection during daily maintenance and operation.

4.2 Data retrieval

Data retrieval is based on the Licel Optical Transient Recorder[3], a sophisticated data acquisition device designed for lidar remote sensing applications. It delivers data with high dynamic range and temporal resolution as it can handle fast signal repetition rates. Licel Transient Recorder combines analog detection of photomultiplier pulse current and single photon counting, enhancing the dynamic range through a combination of a 12-bit, 40 MHz A/D converter and a 250 MHz fast photon counting system. A high-speed data interface allows the acquisition system to be read out between laser shots.

The transient recorder comprises a fast-transient digitizer with onboard signal averaging, a discriminator for single photon detection, and a multichannel scaler with preamplifiers for analog and photon counting systems. The analog signal is amplified, digitized by a 12-bit, 20/40 MHz A/D converter, and written to a 24-bit wide RAM. The high-frequency component of the signal is amplified and detected by a 250 MHz fast discriminator. The photon counting system includes a fast three-stage preamplifier and a discriminator with 64 threshold levels. The data is then stored in standard Licel binary data format[4]. The device can be fully software-controlled, allowing the input ranges for both analog and photon counting to be selected. Selectable are also discriminator levels and active bins. The acquired analog and photon counting signals can be read out separately and transferred to a National Instruments DIO-32-HS family (PC) interface card through 2×16 bit interface. One interface card can control up to sixteen transient recorders, with four operational for the Pathfinder lidar.

4.3 Data analysis

The retrieved lidar data were processed using custom analysis software tools written in Python3[5]. It is used both for the pre-analysis (such as gluing of the analog and photon counting channel or noise removal) and high-level analysis aimed at retrieving the desired atmospheric parameters. All the code is original; however, some of it is based on the MAGIC lidar analysis tool written in the MAGIC Analysis Framework (MARS) [98, 99], which was adapted for the BRL and re-written in Python3. A part of the high-level analysis code was prepared as a part of this thesis as a result of BRL development efforts and is the main deliverable of my work. High-level tools have two main functionalities: data processing (extraction of atmospheric parameters from backscattering lidar return signals in the available detection channels) and visualization of the obtained parameters (atmospheric profiles, 2D atmospheric scans, and temporal profiles). My specific contribution was the implementation of the Raman signal analysis (Section 3.2.1) as well as two-dimensional spatial visualization in

[3] https://licel.com/

[4] https://licel.com/raw_data_format.html

[5] https://www.python.org/

the BRL code. The output of these codes are range profiles of particular investigated atmospheric parameters as well as two-dimensional visual representations, which are stored in standard graphic formats (PNG[6] or PDF[7]). The Range Height Indicator (RHI) tool and the aerosol characterization tool that I coded (calculation and visualization of extinction and backscattering coefficients as well as Ångström exponent and lidar ratio) both use the Data Visualizator (written by M. Gaug) as a framework for basic operation and then expand on it with more complex analysis, such as barycentric interpolation of missing angles in scans or the extraction of aerosol backscatter and extinction profiles.

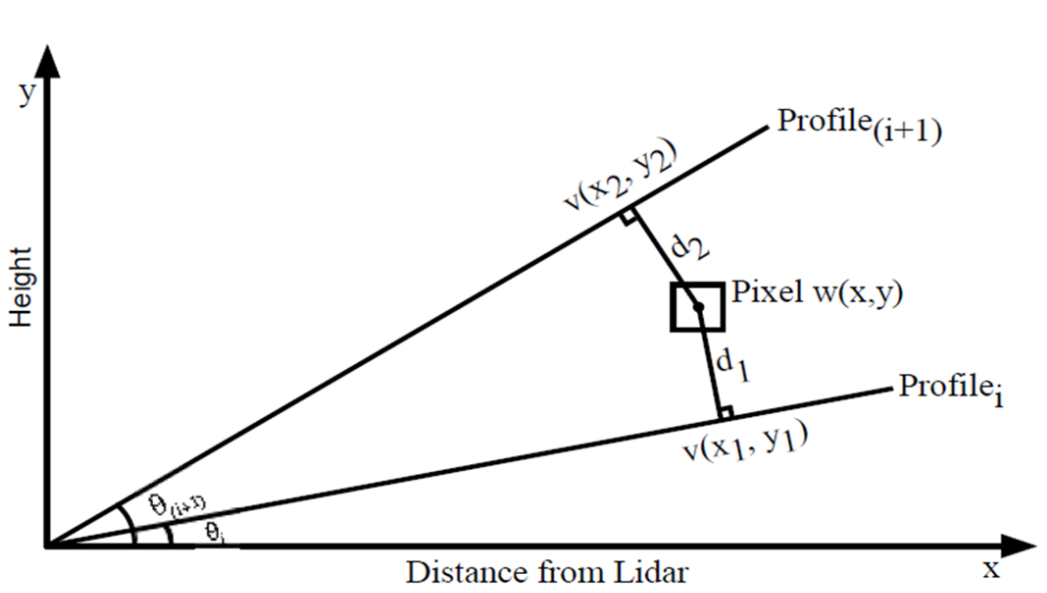

Figure 4.4: Creation of 2D RHI diagrams, using barycentric interpolation for calculation of a weighted logarithm of RSCS value. Each pixel of the diagram represents RSCS value at that position. Adopted from [6].

The RHI tool exploits the BRLs scanning capability, which allows it to make a cross-section scan of the atmosphere, creating a 2D map of atmospheric features above the lidar. RHI diagram is compiled from the data of several lidar return signal profiles (logarithm of range square corrected signal) retrieved at different discrete zenith angles. On a RHI diagram the horizontal axis represents the distance from the lidar and the vertical axis the height above the device. As measurements at discrete angles create gaps in the diagram, the missing pixels were filled using a barycentric interpolation scheme [100] between successive step profiles (Fig. 4.4). For the calculation of

[6] https://www.w3.org/TR/png/
[7] https://www.iso.org/standard/75839.html

weighted value at each pixel the following relation

$$w(x,y) = \frac{v(x_1,y_1)d_2 + v(x_2,y_2)d_1}{d_1 + d_2}, \tag{4.1}$$

was used, where $v(x_1,y_1)$, $v(x_2,y_2)$ are logarithms of measured RSCS values in successive step profiles and d_1, d_2 are the shortest distances between the locations of these measurements and the location of the interpolated pixel. As an example of this representation, see Fig. 4.12. The aerosol characterization follows the analysis described in section 3.2.1 and the example of its final product can be seen in Fig. 4.13.

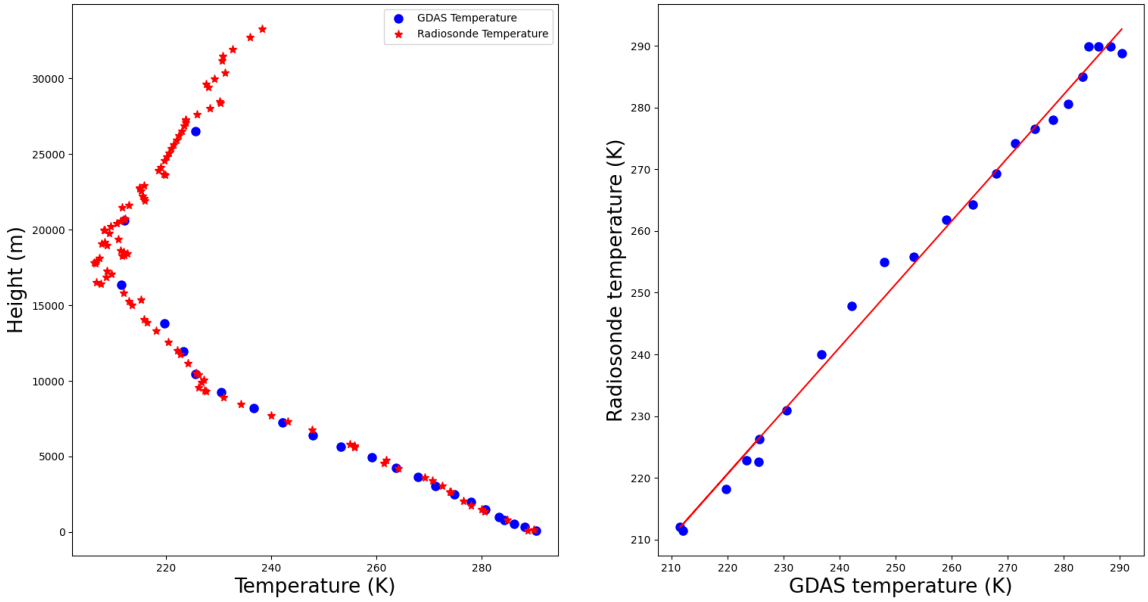

Figure 4.5: Temperature comparison between GDAS for grid point 29°N, 18°W and radiosonde launched from Tenerife (station number 60018, 28.47°N, 16.38°W) on 29 March 2021 at midnight. **Left:** Change in temperature with height, where GDAS values are in blue and radiosonde measurements are in red. **Right:** Linear correlation between GDAS temperature and radiosonde temperature with a correlation coefficient of 1.03 ± 0.02.

The complete BRL analysis software is stored in GitLab[8]. Backscattering on aerosols and molecules of atmospheric gases was treated separately to reduce systematic uncertainties of atmospheric parameters (e.g. Ångström). For the latter, molecular densities were estimated based on Global Data Assimilation System[9] (GDAS) for a grid data point very close to La Palma (29°N, 18°W, about 28 km northwards the ORM, above the Atlantic [101]). GDAS is an established model for predictions of molecular density profiles and integrated densities with minor discrepancies (of the order of 1%) concerning actual atmospheric conditions. Nevertheless, even minor discrepancies were

[8] https://gitlab.cta-observatory.org/cta-array-elements/ccf/LIDAR_Analysis
[9] https://www.ncei.noaa.gov/products/weather-climate-models/global-data-assimilation

found to lead to substantial bias [2], so measurements from radiosondes launched from the Santa Cruz de La Palma airport every 12 hours are being incorporated into GDAS. We assume that GDAS would correctly incorporate this additional data into its constraints forcing the model, however, we also performed ground validation of the model pressure and temperature at the lidar site [101] and radiosonde validation of the model temperature using Tenerife radiosonde data. In both cases very good agreement with GDAS was found. The correlation between temperature measured with radiosonde at Tenerife and the one from GDAS was found to be 1.03 ± 0.02. The error may be due to the fact that temperatures were not retrieved at exactly the same height and that modeling and radiosonde data retrieval positions are not co-located.

4.4 Experimental site Roque de los Muchachos, La Palma

Roque de los Muchachos is the highest peak (2426 m a.s.l.) of La Palma, the westernmost island of the Canary Islands chain. The islands are located in the Atlantic Ocean, off the coast of northwestern Africa, as shown in Fig. 4.6. The climate is generally subtropical and oceanic with warm temperatures and less pronounced seasonality [102], but changes significantly with elevation. The island is of volcanic origin and is divided into a northern, older part of the island, where the volcanic activity stopped, the and a southern, younger part, which is still volcanically active, with the latest eruptions happening in 2021, 1971, and 1949. The main drivers of the weather patterns on La Palma are the descending branch of Hadley cell [103] and Trade winds from the Azores. Strong temperature inversions are typical for this area (see Fig. 4.7) and reach up to 1200 m a.s.l. during summer and 1800 m a.s.l. during winter [104]. Inversions are present for about 80% of the time. An inversion creates two separate well-defined regimes, where the moist marine air is trapped below the inversion layer and the dry air above it. The free troposphere above the inversion layer is ultra clean, with concentrations of PM_{10} particles (aerodynamic diameter of 10 μm or less) lower than 10 μg m^{-3} [5]. This is one of the main reasons why is the Observatorio del Roque de los Muchachos (ORM) is considered to be among the best astronomical sites globally. The observatory facilities located at elevations between roughly 2000 m a.s.l. and 2400 m a.s.l., it is located in an environment with very clean atmospheric conditions most of the time. In cases of a weakening inversion layer, low-level African trade winds may start to dominate the region. Consequently, the boundary layer rises above the ORM and "Calima", the Saharan dust intrusions occur [105, 106, 107]. In this case, large amounts of aerosols are introduced into the troposphere, and the light transmissivity is highly reduced. Saharan dust during Calima can reach altitudes up to 8400 m a.s.l. [108], even though it is mainly found below the heights of 2000 m above ground [106]. The vertical atmospheric profile of dust loading can vary from a turbulently mixed single layer to strong stratification in several distinct layers, as visible in Fig. 4.8.

Figure 4.6: **Top:** The location of the Island of La Palma (marked with a red box) on a regional map. It is the westernmost island in the chain of the Canary Islands, just west of the coast of Africa in the Atlantic Ocean. **Middle:** A bird's eye view of La Palma. The island's northern part is dominated by the Caldera de Taburiente, with the CTAO-North location marked with a red star. In the southern part of the island, a yellow star marks the location of the Tajogaite volcano. **Bottom:** A topographic view of the northern slopes of Caldera de Taburiente, where the observatory resides. The satellite images and topographic view were acquired from Google Earth[10](©Google Earth 2023).

[10] `https://earth.google.com/web`

Figure 4.7: Cloud accumulation on the temperature inversion layer between moist and wet regime. Photo taken from the Roque de los Muchachos Observatory in the morning of 15. 04. 2022.

Volcanic eruption is another major event that can hinder light transmissivity in the atmosphere. Volcanic activity can produce large quantities of ash that can, due to the vertical development of a volcanic plume, highly reduce light transmission at any altitude throughout the troposphere, as happened in the case described in 4.8. The volcanoes near ORM are not the only factor that has to be considered. Stratovolcanic eruptions are rare events that can influence the optical visibility in the lower stratosphere (15000-20000 m a.s.l.) [2]. On such altitudes, ash can travel very far, and volcanoes from other parts of the world have to be considered, as was the case of El Chichón in Mexico and Mount Pinatubo in the Philippines [109].

4.5 Observatorio del Roque de los Muchachos test campaign

The Barcelona Raman Lidar (BRL) was deployed at Observatorio del Roque de los Muchachos (ORM) for extensive on-field tests between February 2021 and May 2022. The system was deployed in an experimental area of the LST-1 telescope, near the area where the final device for CTAO-North will be deployed. The BRL recorded its

Figure 4.8: The highly stratified layers containing different aerosol types on a photo were taken on 17 September 2021, during the campaign for calibration and validation of the Aeolus satellite mission above Cape Verde (in similar environmental conditions as La Palma) [110, 111, 112].

first light at ORM on 25 March 2021. From that day to the end of its operation and removal from ORM, it operated for a total of 33 nights and accumulated about 20 hours of data. Data-taking-related details are summarized in table A1. The relatively limited dataset is largely due to the conditions imposed by the Instituto de Astrofísica de Canarias (IAC), which manages the ORM site, and the LST consortium. BRL operation was limited to astronomic twilight periods or moonlit nights, which reduced the lidar performance, as it was designed to operate during dark nights. During most of the campaign, the laser worked at reduced power, and the photomultiplier voltages were set to about 50% of their design values to protect the equipment. BRL was not able to operate under bad weather conditions (e.g., rain, fog, or sleet). The prototype also experienced a number of technical problems that prevented operation, most frequent being the LST-1 site safety interlocks, failure of laser startup due to low system temperature, and DAQ software problems. Despite these problems, the BRL operation was tested under several meteorological conditions, including during Calima events and the first stages of the Cumbre Vieja volcano eruption (now known as Tajogaite), in September 2021. During later stages of volcanic activity, the observatory, as well as BRL activities, were stopped due to volcanic ash deposition on the site. Testing resumed from January to May 2022, when it was dismantled and removed from the ORM. Apart from the lessons learned about the device itself, the testing provided several good measurements during interesting atmospheric phenomenae. BRL has performed well in measurements of backscattering and extinction coefficients,

both necessary for CTAO calibration. We used complete lidar information about the atmosphere in selected cases to explore its physical properties, including basic characterization of aerosol types above the observatory.

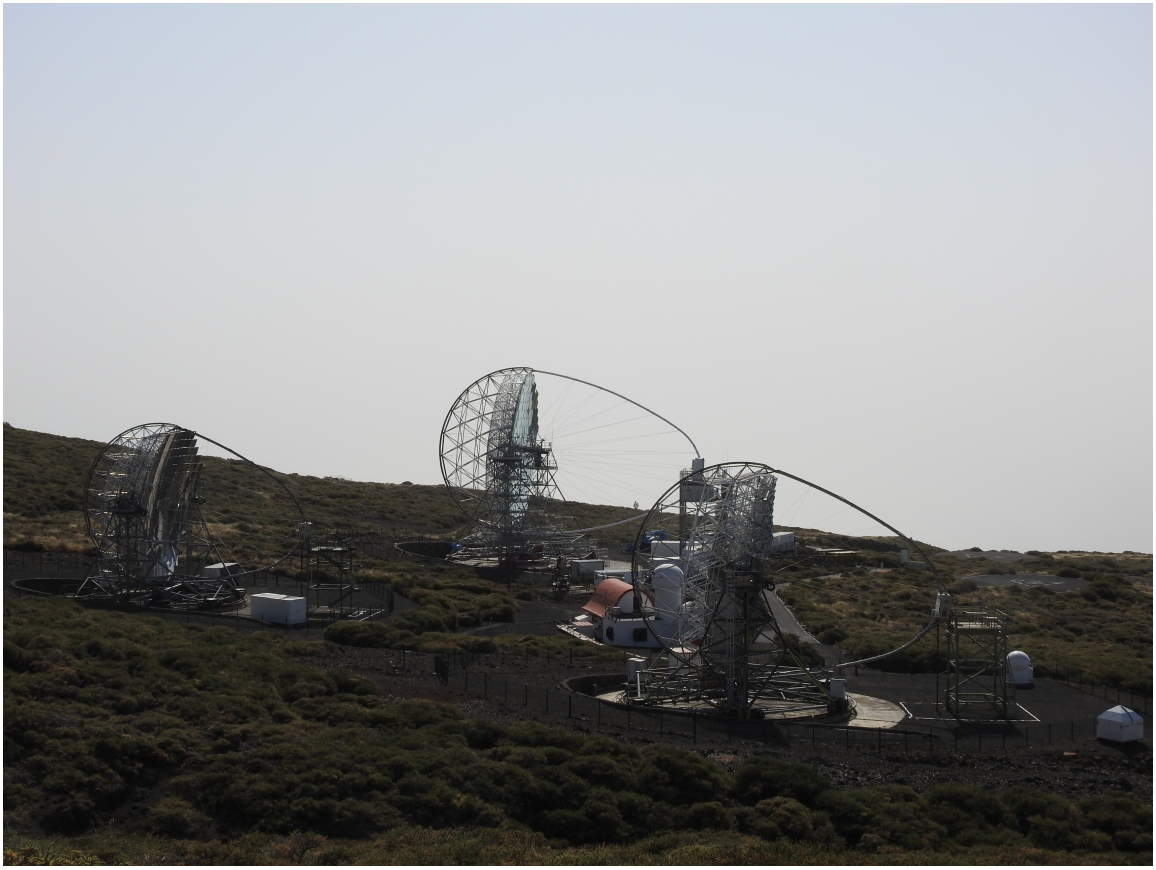

Figure 4.9: The LST-1 and MAGIC telescopes on a hazy calima background.

4.6 Case 1 - Clear sky

ORM location was chosen due to its ultra-clean atmosphere, suitable for astronomic observations. Most of the lidar data (Appendix A1) were therefore retrieved in clear sky conditions. Even though this scenario is ideal for astrophysical observations, it posed a problem for testing of the BRL prototype lidar, where more scatterers in the atmosphere would be very welcome. The combination of low backscattering signals, safety requirements (reduced laser power, measurements allowed only during twilight at full moon), and high noise due to the persisting electronics issues led to low signal-to-noise ratio of the measurements. This is particularly evident in the return signal of the weak Raman lines, but also affected the stronger elastic lines. As a result, most of the data was not truly usable for atmospheric studies, it was only useful for the BRL lidar debugging purposes.

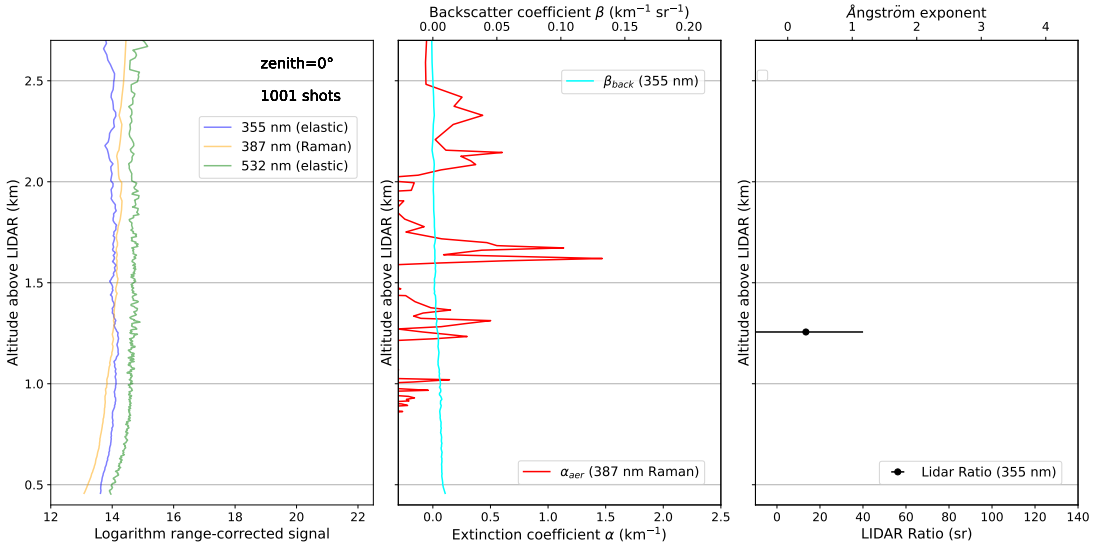

Figure 4.10: **Left:** Range square corrected lidar returns in the three analog channels where blue at 355 nm and green at 532 nm are elastic, and orange at 389 nm is the Raman backscattering channel. The measurement was performed at a zenith angle of 20° with 2001 laser shots at 10 Hz rate. All three return signals were very low. **Center:** The backscattering coefficient retrieved from 355 nm channel in cyan and the extinction coefficient of aerosols retrieved from Raman 389 nm channel in red are both close to 0. **Right:** The lidar ratio for 355 nm channel is close to 0 and has a large uncertainty. Ångström exponent profile (355 nm-532 nm) could not be retrieved.

To illustrate this, we present the measurement made on 29 March 2021 in ultra-clean atmospheric conditions (Fig. 4.10). All three return signals (elastic and Raman) are extremely low. Atmospheric backscattering and extinction, the parameters relevant for the Cherenkov Telescope Array Observatory (Section 1.3.1) can nevertheless be adequately retrieved and are both close to 0 with a relatively large uncertainty (due to low signal-to-noise ratios in all three channels and the subtraction of the molecular part of the backscattering and extinction coefficients). These uncertainties further increase with the complexity of the analysis, when combining data from different channels, making the retrieval of quantities such as lidar ratio meaningless. We were fortunate that during the BRL commissioning we experienced two atmospheric events with elevated aerosol content (periodic incursion of mineral dust from Africa and a volcanic eruption on the island of La Palma itself. During these two events, described in detail in sections 4.7 and 4.8, lidar return signals were about two to four magnitudes higher than in ultra-clean conditions and allowed for complete analysis of all retrievable atmospheric parameters, which was a welcome test of BRL lidar full capabilities.

4.7 Case 2 - Calima

In the fourth and fifth week of August 2021, an approximately ten-day-long Saharan dust intrusion, so-called Calima, occurred (Fig. 4.9). Calima breached the usually stable inversion layer and significantly degraded the air quality above the observatory. In the first few days, mineral dust concentration was so high that multiple scatterings made accurate analysis of constituent aerosols almost impossible. In the event's final days, when Saharan dust spread over a large part of the Atlantic Ocean (Fig. 4.11), the concentration of scatterers decreased. A more accurate analysis was performed on data collected in the evenings of 25 and 26 August 2021. On both days, average lidar ratios were found to be around 40-50 sr and Ångström exponent was below 1.5, which implies scattering on large, irregularly-shaped particles, such as mineral dust [113, 114, 115]. A drop in extinction coefficient at about 1.5 km, that occurred on both days, is probably associated with the top of the dust layer. Especially interesting is the case on 25 August, where a scan revealed dust that was not uniformly distributed

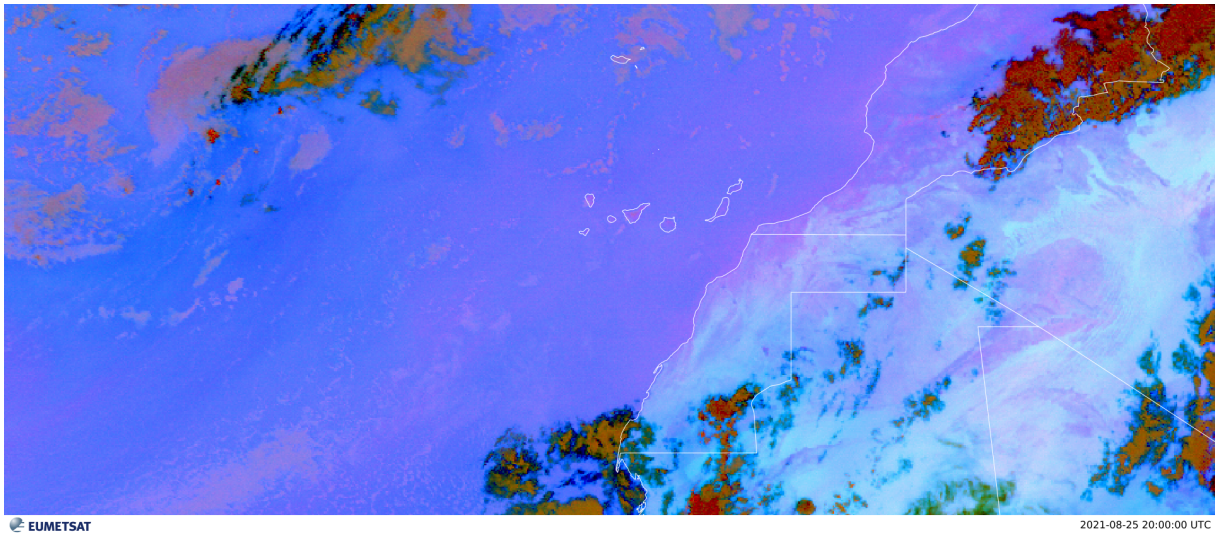

Figure 4.11: Satellite image (*Dust RGB - MSG - 0 degree*) of mineral dust over Western Africa and the Atlantic Ocean, including the Canary Islands. Dust is colored in pink, clear sky in blue, and clouds in dark red. The image was taken on 25 August 2021 at 20:00 UTC, simultaneous to our lidar measurements. ©EUMETSAT 2021.

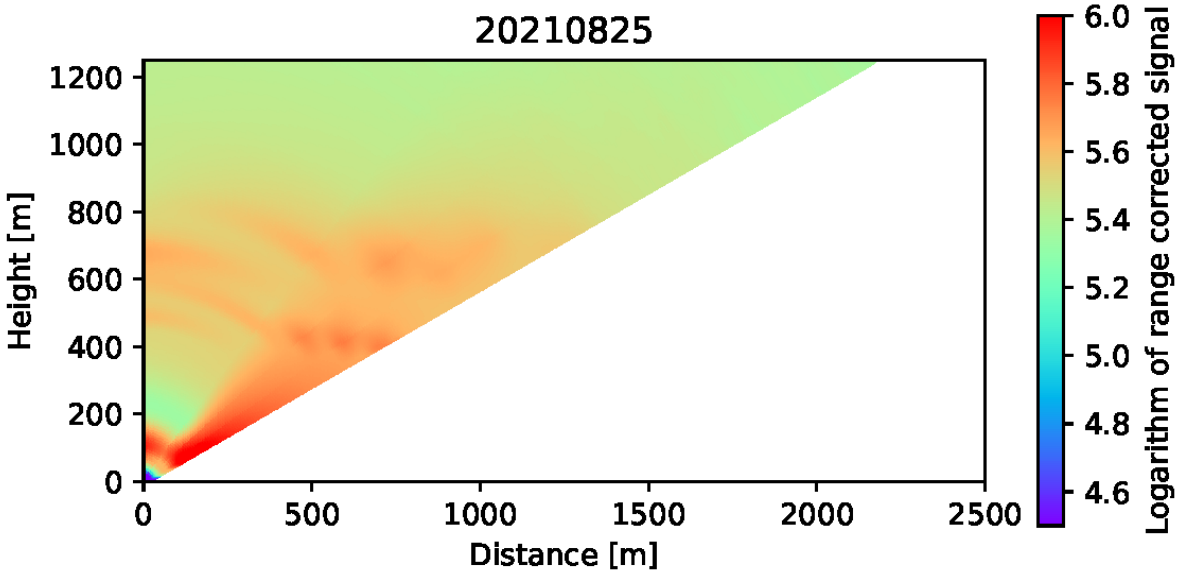

Figure 4.12: Spatial distribution of clouds and aerosol loading above the ORM on 25 August 2021. The plot is based on five 90 s long measurements in the 355 nm return channel at different zenith angles ranging from 0° to 60° in steps that correspond to regular increases from air mass of 1 to air mass of 2. A barycentric interpolation was used to fill the gaps. We can see an irregular aerosol density profile created by Saharan dust, which slowly disperses to a clear atmosphere.

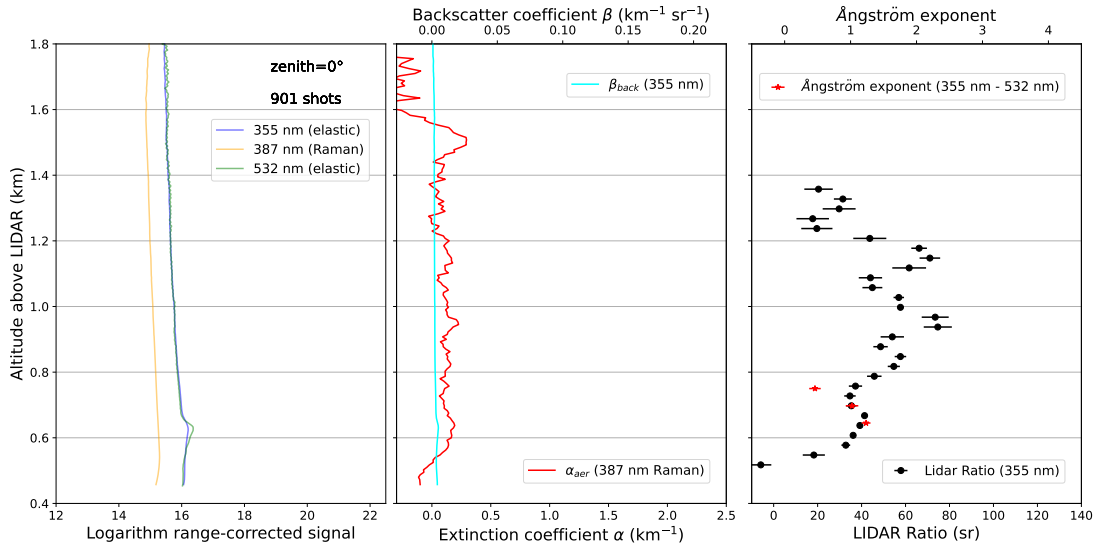

Figure 4.13: Atmospheric properties on 25 August 2021. **Left:** Range square corrected lidar returns in the three analog channels where blue at 355 nm and green at 532 nm are elastic, and orange at 389 nm is the Raman backscattering channel. The measurement was performed at a zenith angle of 0° with 901 laser shots at 10 Hz rate. **Center:** The backscattering coefficient retrieved from 355 nm channel in cyan and the extinction coefficient of aerosols retrieved from Raman 389 nm channel in red. **Right:** Ångström exponent profile (355 nm-532 nm) in red stars and the lidar ratio for 355 nm channel in black dots.

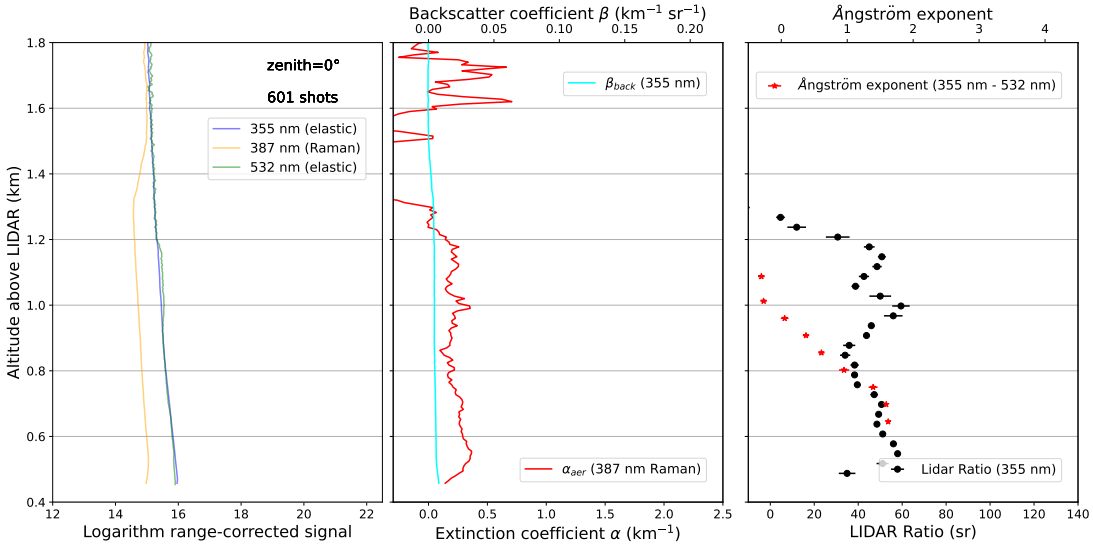

Figure 4.14: Atmospheric properties on 26 August 2021. **Left:** Range square corrected lidar returns in the three analog channels where blue at 355 nm and green at 532 nm are elastic, and orange at 389 nm is the Raman backscattering channel. The measurement was performed at a zenith angle of 0° with 601 laser shots at 10 Hz rate. The increase of Raman signal is an artifact from background subtraction, where even a tiny may amplify at high distances. **Center:** The backscattering coefficient retrieved from 355 nm channel in cyan and the extinction coefficient of aerosols retrieved from Raman 389 nm channel in red. **Right:** Ångström exponent profile (355 nm-532 nm) in red stars and the lidar ratio for 355 nm channel in black dots.

throughout the lower troposphere (see irregular density profile patterns in Fig. 4.12). Instead, there are visible elevated layers of scatterers about 400 m and 700 m above the ground (Figs. 4.12 and 4.13). Similar stratification of aerosol layers above the Atlantic was also observed in 2021 above the nearby Cape Verde Islands (Fig. 4.8).

4.8 Case 3 - Tajogaite volcano eruption

On 19 September 2021, the Cumbre Vieja volcano erupted in the southern part of La Palma Island. The volcano is located about 14 km air distance toward the south-south-east of the Observatorio del Roque de los Muchachos (ORM). The plume spread over the entire island in the following days, as shown in Fig. 4.15. A vertical sky scan was performed during the measurements on the evening of 22 September 2021. At that time, the laser was not yet operated at full power, and the high voltages of the elastic-lines PMTs were reduced to protect the readout system after the reflectivity increase of the re-aluminized primary mirror. Only later, during the spring of 2022, further protective measures were introduced, and the system was operated at full power. In the obtained data, two distinct features are visible: an optically thick layer of clouds at altitudes above 2300 m a.g.l. directly above the lidar, at a zenith angle of 0° (Fig. 4.16), which dissipates out toward the north, and a thinner layer located at an altitude of 1500 m a.g.l., which covers all the scanned sky quite homogeneously. From the ratio between the extinction and backscattering coefficients at one wavelength,

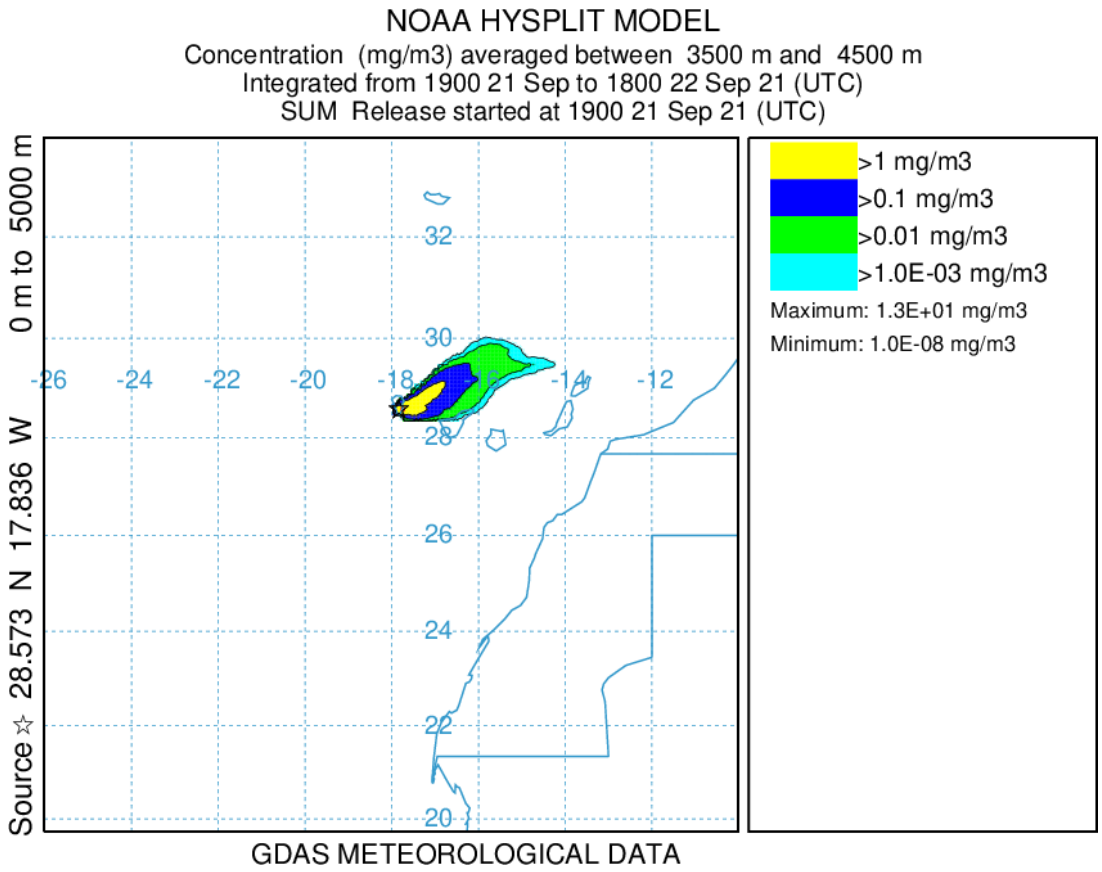

Figure 4.15: Dispersion of volcanic ash, continuously ejected from the Cumbre Vieja volcano one day before the lidar measurement, as obtained from the NOAA ARL HYSPLIT Dispersion Model [116, 117]. The colour contours represent the daily average of ash concentration at altitudes between 3500 m a.s.l. and 4500 m a.s.l. where the elevated aerosol layer was observed by the BRL. Numerical values of ash concentrations can be regarded as estimates only due to the quantitatively unknown volcanic mass ejection rate during that time.

the so-called lidar ratio, shown in Fig. 4.17, we can further distinguish two layers: one with large diameter scatterers at about 1.6 km above the lidar and another layer of much smaller particulates beyond 2.3 km a.g.l. Similar conclusions can be drawn from the ratio between the extinction coefficients of two different wavelengths, the so-called Ångström exponent. We obtained a lidar ratio of (76±20) sr and an Ångström exponent of 0.30±0.02 for the lower overdensity, indicative of particles with large diameters. In contrast, the lidar ratio for the upper one is considerably smaller and comparable with almost point-like scatterers. Note that a transition is visible within the upper layer from larger (below 2.8 km) to smaller scatterers. From the combined results of both ratios and knowledge about the local environment, we can conclude that the lower aerosol loading is composed of volcanic ash that was dispersed from the Cumbre Vieja volcano plume, while the upper part must be due to a cloud with typical characteristics for the La Palma atmosphere at those altitudes. This is also

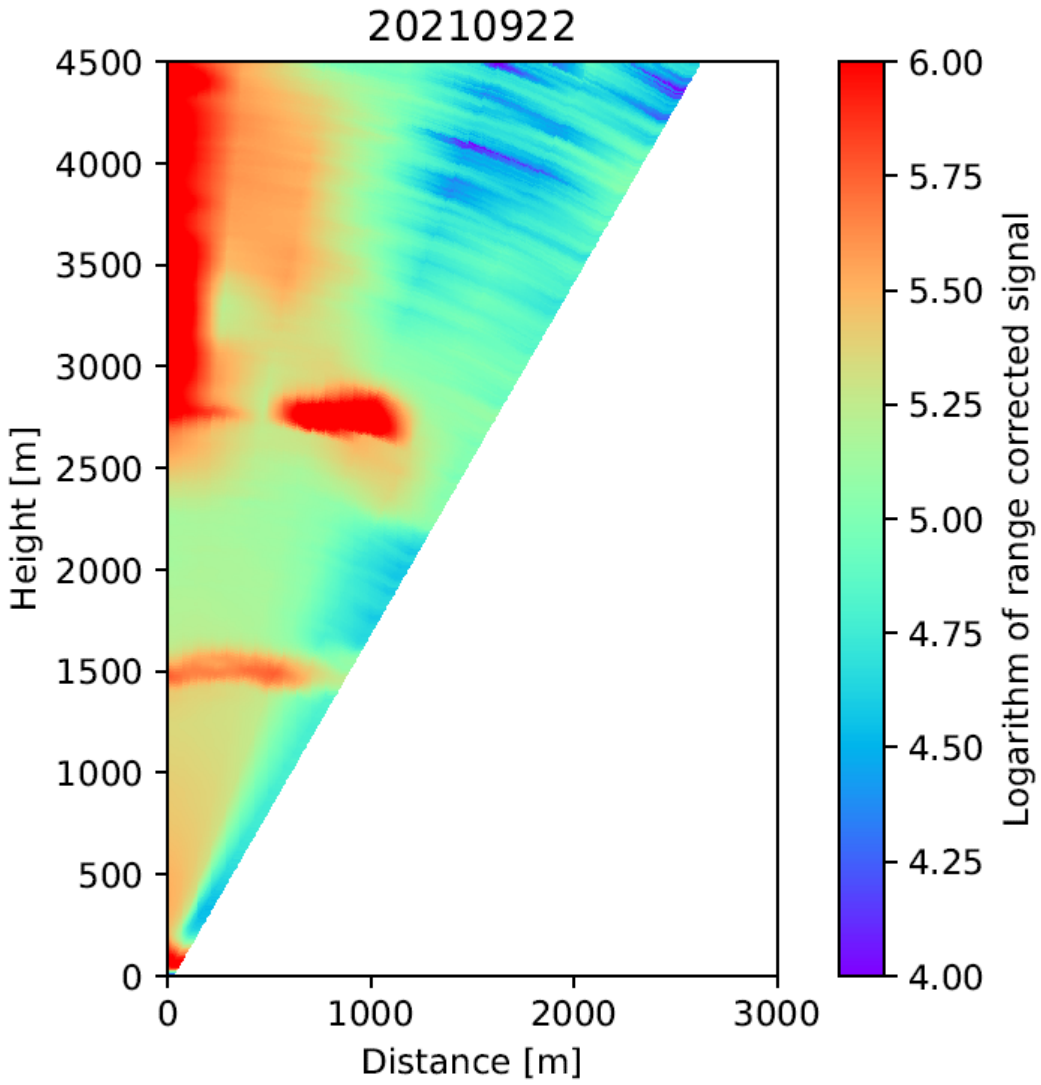

Figure 4.16: Spatial distribution of clouds and aerosol loading above the ORM on 22 September 2021. The plot is based on seven 200 s long measurements in the 355 nm return channel at different zenith angles ranging from 0° to 30° in steps of 5°. A barycentric interpolation was used to fill the gaps. The volcanic ash layer is clearly visible 1500 m above the observatory (approximately 3700 m a.s.l.).

corroborated by satellite data, shown in Fig. 4.18. Even though, during the lidar measurement, the plume is found below the thick cloud layer, visible also in the lidar measurement, completely covering it from the satellite view, the clockwise motion of the plume visible in multiple consecutive satellites suggests that it was located above the ORM during the time of measurement.

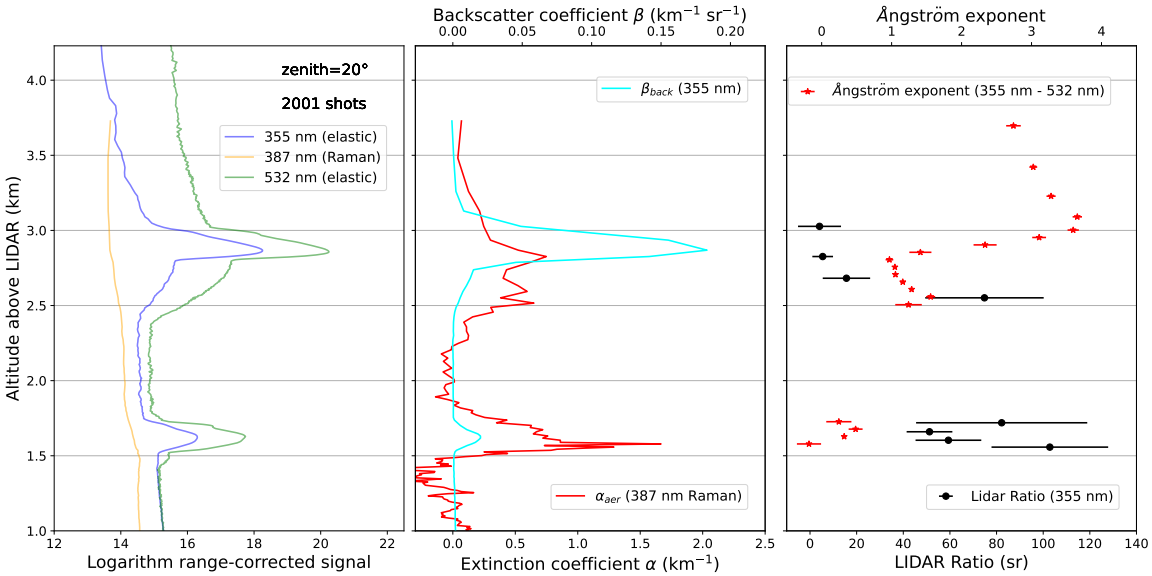

Figure 4.17: **Left:** Range square corrected lidar returns in the three analog channels where blue at 355 nm and green at 532 nm are elastic, and orange at 389 nm is the Raman backscattering channel. The measurement was performed at a zenith angle of 20° with 2001 laser shots at 10 Hz rate. **Center:** The backscattering coefficient retrieved from 355 nm channel in cyan and the extinction coefficient of aerosols retrieved from Raman 389 nm channel in red. The extinction coefficient exhibits the same peaks visible in backscattering channels, but the lower peak is much more prominent in the case of extinction. **Right:** Ångström exponent profile (355 nm-532 nm) in red stars and the lidar ratio for 355 nm channel in black dots.

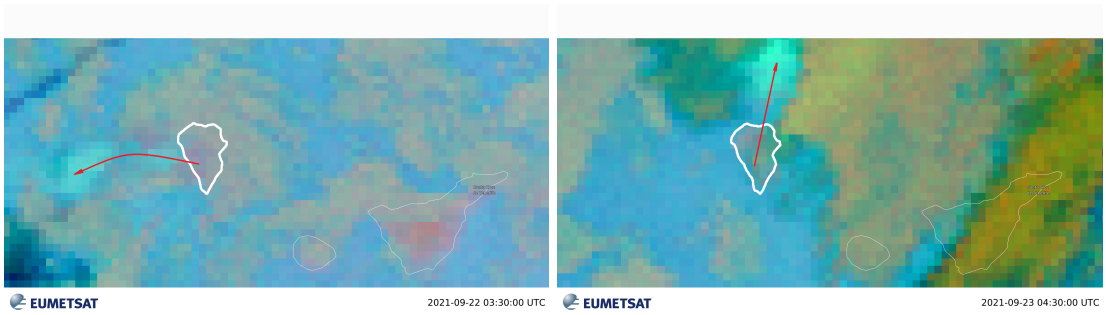

Figure 4.18: Satellite image (*Volcanic Ash RGB - MSG - 0 degree*) of the volcanic plume (cyan, corresponding to enhanced SO_2 concentration) above La Palma. The left image was taken on 22 September 2021 at 03:00 UTC, our lidar measurement was performed at 19:30 UTC, and the right image was taken after the measurement, on 23 September 2021 at 04:30 UTC. The wind direction (on the images indicated with a red arrow) changed in a clockwise manner, which blew the plume above the observatory. ©EUMETSAT 2021.

5

Characterization of aerosols with polarization Raman lidar

The Barcelona Raman Lidar has proven to be able to provide backscattering and extinction coefficient profiles as required by the CTA Observatory. Moreover, we also demonstrated that it can be used for basic aerosol characterization using the obtained lidar ratio and Ångström exponent, as shown in the case of Tajogaite volcanic eruption (4.8). The limitation of this characterization is that lidar ratio can be similar for several different aerosol types, as the extinction coefficient changes due to various parameters such as size, shape, composition, and loading of aerosol particles. We can infer aerosol particles' size distribution and composition with the Ångström exponent, as different aerosols have different wavelength dependencies. The depolarization should be invoked to get a much clearer picture of the distribution of specific aerosol types [43]. The depolarization ratio alone can show the thermodynamic phase of cloud constituents and can provide information about multiple scattering, i.e., the volume density of scatterers. The multiple scattering can be especially important for Cherenkov astronomy as light can be scattered into or out of the field-of-view of the telescopes. It can thus influence the calculation of total primary energy [118, 119, 120] even though the Cherenkov light is not so prone to this effect as fluorescent light, due to the smaller emission angles relative to the shower axis [121].

As the Barcelona Raman lidar (BRL) does not have the capability to detect polarization changes in the backscattered signal, we used a similar Raman lidar system with an additional depolarization detection capability at the University of Nova Gorica (UNG) to estimate the impact of aerosol typing through polarization change. Even though the two devices are not entirely the same, the UNG lidar is conceptually close enough to the BRL to use a common data analysis platform. The UNG lidar has the same number of elastic and Raman channels as the final version of CTAO-N Raman lidar. In addition, the UNG lidar measures the depolarization of the almost 100% polarized outgoing laser pulses by collecting it in two orthogonally polarized elastic detection channels.

As the test case for aerosol characterization using depolarization, we presented an observation campaign studying bioaerosol-induced ice nucleation in clouds, where

the information on the thermodynamic phase of cloud constituents (droplets or ice particles) was crucially important. In three measurement campaigns from October to December 2020, the constituents of clouds were sampled *in situ* while the cloud was simultaneously probed with a polarization Raman lidar to distinguish between the liquid and solid phases of water inside the cloud. In these campaigns I was operating the UNG lidar and performing measurements, which I later analyzed and interpreted in terms of the type of cloud contents.

5.1 Ice nucleation potential for bioaerosol cloud-condensation nuclei in mixed-phase clouds

A subset of aerosol particles, called cloud condensation nuclei (CCN), facilitate the condensation of water vapor and the formation of cloud droplets at supersaturated conditions due to a combination of their hygroscopicity and size. Another type of aerosol particle, called ice-nucleating particles (INP), is the key to facilitating the formation of ice in the temperature range between 0 °C and about -38 °C. While CCN is a common type of aerosol occurring at concentrations of 10^4-10^6 /l of air [122], INP are much less abundant and occur at concentrations of 10^{-6}-10^3 /l of air [123]. The type and concentration of CCN and INP directly reflect in the cloud droplet numbers and size distribution, therefore driving the optical properties of clouds. In addition, INP is a prerequisite for a large fraction of precipitation formation over continents [124] and therefore affects the cloud lifetime and the atmospheric water cycle [125].

Although the concentrations of biological aerosols are 4-5 orders of magnitude smaller than the concentrations of both CCN and cloud droplets [126], they may have an important role in the development of clouds and precipitation [127] as bioaerosols nucleate ice at higher temperatures (between -13 °C and 0 °C) [123]. Microbial cells are typically considered as efficient as CCN due to their relatively large sizes [128] and are considered easily activated into droplets under cloudy conditions [129].

To investigate the role of specific biological agents (microbial cells, bacteria, viruses, and fungi) as CCN, they were sampled *in situ* inside the cloud. At the same time, the thermodynamic phase of the cloud was determined through the change in polarization of light, which was due to different shapes of particles on which light scatters (see Section 2.4). The study investigated the composition of bacterial and fungal communities in interstitial and coarse bioaerosols and assessed whether specific taxa are better CCN than others. In addition, the impact of multiple scattering on the lidar signal can be seen.

5.2 Experimental site in the Vipava Valley

The campaign was conducted in the Vipava Valley in western Slovenia. It is located on a junction between three different geographic regions with distinct climates. The Vipava Hills enclose the valley - the Karst Plateau from the south and the Trnovski

Gozd Plateau and Nanos from the north. To the east, where the Nanos and the Vipava Hills meet, there is the Razdrto Pass, behind which lies central Slovenia. To the west, the valley opens to the vast Friulian plains. The valley floor is flat, with the lowest point at about 60 m a.s.l. (Batuje) and the highest at about 170 m a.s.l. (Podnanos) ∼40 km along the length of the valley. Both edges rise quickly, with the northern altitudes reaching above 1000 m a.s.l. and the southern altitudes are of about 300 m a.s.l.

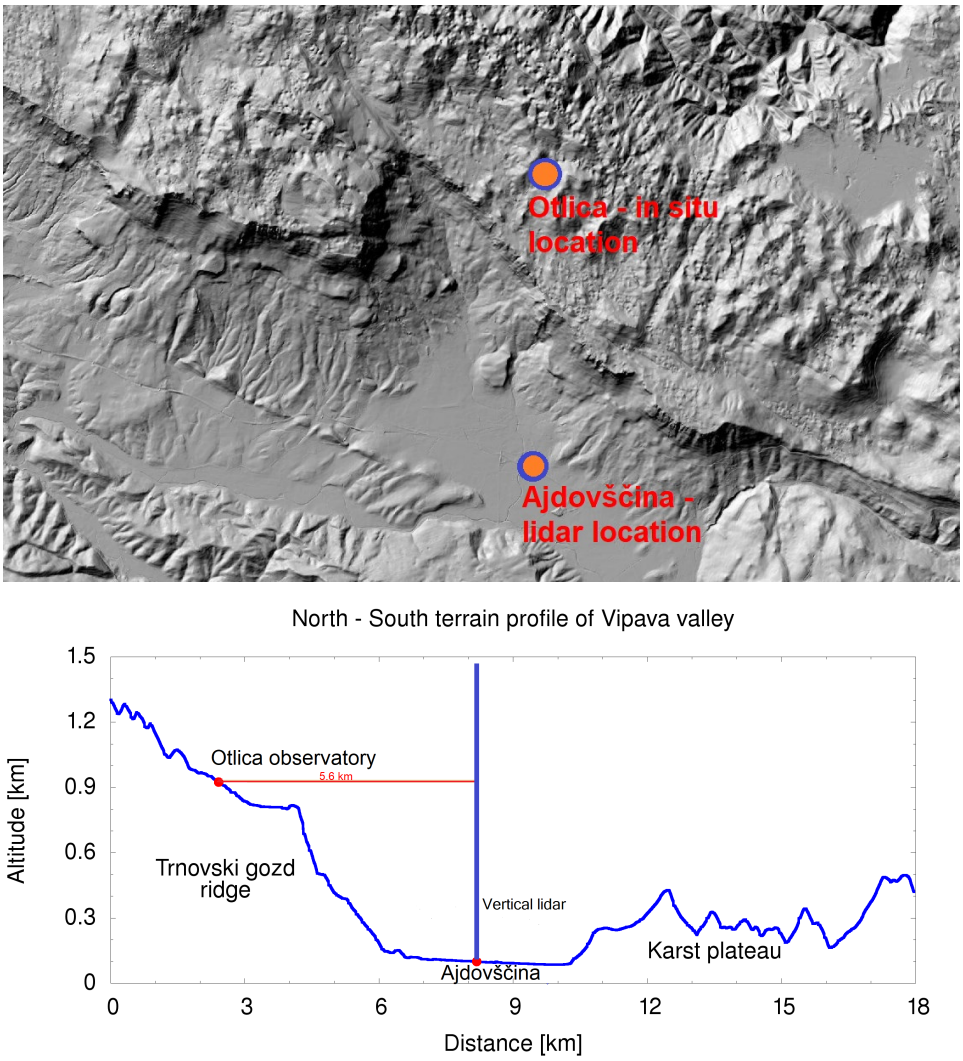

Figure 5.1: **Top:** A topographic map with marked positions of Otlica meteorological observatory and Ajdovščina (©Atlas okolja, ARSO[11]). **Bottom:** Schematic view of a terrain profile of the Vipava valley. The lidar in Ajdovščina is located below a Trnovski Gozd Plateau, where the Otlica observatory resides. Between them is about 800 m vertical drop and an air distance of 5.6 km.

[11] http://gis.arso.gov.si/atlasokolja/profile.aspx?id=Atlas_Okolja_AXL@Arso

Figure 5.2: Assembled lidar system in its working environment at the Center for atmospheric research of the University of Nova Gorica in Ajdovščina. The atmosphere is accessed through a 1 m^2 rooftop window with $> 85\%$ light transmission and an electrical shutter. The telescope is mounted as close to the window as possible, leaving room for the spectroscopic filter and the transmitter below. In addition, panels painted in black are covering most of the mount to prevent any additional stray light from the room to get into the lidar, as well as to prevent any laser beam scattering around the room the system is built in.

The specific terrain configuration and infrastructure in and above the valley are ideal for studying aerosols composing clouds in stable, non-windy conditions. The horizontal distance between the University of Nova Gorica (UNG) lidar site and its Alpine meteorological observatory at Otlica[12], where the *in situ* sampling took place, is only about 5 km. A low cloud, observed by lidar from Ajdovščina, in such conditions, is the same as a cloud in Otlica. Because of the elevation difference, the sampling device can be set up on the surface, providing much simpler and more extended sampling periods as an airborne mission would have.

5.3 Main lidar components

The polarization Raman lidar system, located at the University of Nova Gorica in Ajdovščina was completed in August 2017 and is described in detail in [43, 65, 130]. It allows simultaneous measurements of aerosol backscatter coefficients at 355 nm and 1064 nm, lidar ratio, volume depolarization ratio, particle depolarization ratio, and backscattered Ångström exponent. The lidar has two independent transmitters, one at 355 nm and the other at 1064 nm, a receiver telescope, a spectroscopic filter with detectors for five separate channels, and the data acquisition system. The channels cover two Raman signals (vibration nitrogen signal at 386.7 nm and vibration water vapor signal at 408.4 nm), two Mie-Rayleigh signals at 355 nm with different polarization planes and Mie-Rayleigh signal at 1064 nm.

The lidar is set up indoors so that it can also be operated in unfavorable weather conditions (e.g., strong wind, rain). The components are assembled on a mechanical support that holds the telescope 180 cm above the ground as close as possible to a 1 m^2 rooftop borosilicate window with more than 85% light transmission in the UV and IR part of the EM spectrum in order to prevent light from reaching the receiver from the room. In addition, the mounting allows the transmitter and spectroscopic systems to be directly below the telescope.

5.3.1 Transmitter

The transmitter comprises two Nd:YAG pulsed lasers, beam expanders, and turning mirrors. Even though the fundamental wavelength of the Nd:YAG laser system is 1064 nm, which operates Big Sky Ultra, the more powerful Q-smart 450 laser emits 355 nm light that is created using an attached non-linear harmonics generator. The Big Sky Ultra laser, operates with a 20 Hz repetition rate and pulse energy of 50 mJ, at 1064 nm is used to investigate Mie scattering on aerosols. The Q-smart 450 laser, operating with a 10 Hz repetition rate and pulse energy of 130 mJ at 355 nm, is used to investigate Raman and Mie–Rayleigh scattering. As Q-smart 450 laser pulses at 355 nm were found to be only 98.5% horizontally polarized [65], a polarization beam splitter with T_P:T_S > 2000:1 was employed to improve the purity to better than 99.99%.

[12] https://www.ung.si/en/research/center-for-atmospheric-research/otlica-observatory/

Misalignment of the horizontal polarization plane of the transmitter is less than $\pm 1^{\circ}$. For both lasers, the fixed full-width divergence of the beams was reduced to less than 0.2 mrad using beam expanders. A $3\times$ beam expander was added to the 355-nm laser and a $5\times$ beam expander to the 1064-nm laser.

5.3.2 Receiver

The main parts of the lidar receiver are a telescope, a spectroscopic filter, and detectors. The backscattering light the telescope collects is then separated into five channels with specific wavelengths and polarizations. Light pulses in each channel are converted to electric signals by an avalanche photodiode or photomultiplier (depending on the wavelength).

A Cassegrain-type telescope with 600 mm primary and 80 mm secondary aperture is used to collect the backscattered light. A large telescope aperture provides sufficient return signal intensity for rapid Raman measurements. In the telescope's backplane, a coupling lens was installed to focus the beam toward the far end of the filter box, located approximately 2 m from the end of the telescope. At the focal point, the beam's diameter is $\sim$2 cm. The light travels nearly parallel throughout the system with a full-angle convergence of approximately 2.5 mrad.

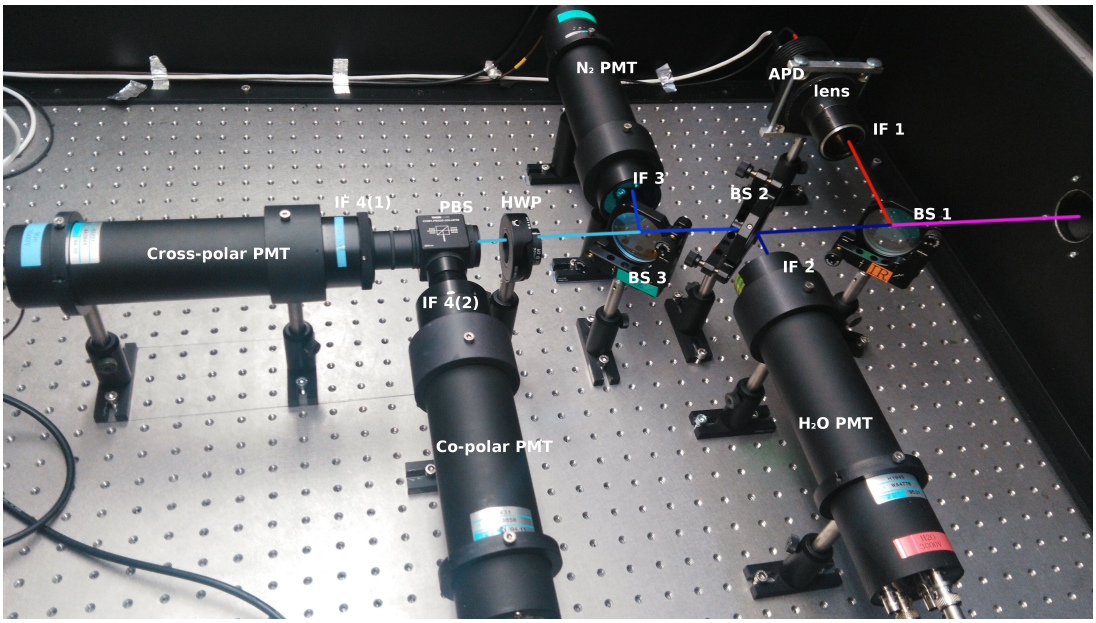

Figure 5.3: Optical components arrangement inside the spectroscopic box with indicated light path. Beam-splitter (BS1), interference filter (IF1), aspherical lens and avalanche photodiode (APD) are used for the infra-red elastic channel. BS2, IF2 and a photomultiplier tube (PMT) are used for the H2O channel. BS3, IF3 and a PMT are used for N2 channel. Half wave plate (HWP), polarization beam splitter (PBS), two interference filters (IF4) and two PMTs are used for S and P polarization UV elastic channels.

The telescope is shielded from different environmental conditions with a 5 mm thick UV-transparent borosilicate glass window measuring 850 mm × 980 mm. The transmission of the window for vertical light is 85% (355 nm) and 90% (1064 nm). The total averaged optical efficiency of the receiver system, including telescope (95%), lens (90%), turning mirror (98%), and borosilicate glass, is estimated at 71.4% in UV and 75.6% in IR.

Table 5.1: Specifications of the components used in the spectroscopic system. The beam splitter (BS1), interference filter (IF1), and aspherical lens were used for the infra-red Mie channel. BS2 and IF2 were used for the H_2O channel. BS3 and IF3 were used for the N_2 channel. HWP, PBS, and two interference filters (IF4) were used for S and P polarization UV Mie–Rayleigh channels. $T_{P/S}$: P/S polarization transmittance, $R_{P/S}$: P/S polarization reflectance, WL: Wavelength.

Spectroscopic system

BS 1		**BS 2**	
$T_P/T_S(<650\,nm)$	>95.0%	T_p/T_s(345–395 nm)	>95.0%/90.0%
$R_P/R_S(>650\,nm)$	>97.0%	R_p/R_s(400–415 nm)	>97.0%
BS 3		**PBS**	
$T_{P/S}$(345–365 nm)	>95.0%/90.0%	T_P/T_S(355 nm)	95.0%/0.5%
R_P/R_S(385–395 nm)	>97.0%	R_P/R_S(355 nm)	99.5%/5.0%
IF 1		**IF 2**	
Central WL	1064 nm	Central WL	407.7 nm
Bandwidth	0.6 nm	Bandwidth	5.2 nm
Peak T	25.0%	Peak T	66.9%
IF 3		**IF 4**	
Central WL	386.5 nm	Central WL	355 nm
Bandwidth	4.8 nm	Bandwidth	1.0 nm
Peak T	65.0%	Peak T	55.0%
Aspherical lens		**HWP**	
Focal Length	25 mm	Central WL	355 nm
Diameter	25 mm	Rotation angle resolution	1°

A beam-splitter (BS1) reflects the IR light to an IR filter IF 1 and a 25 mm, 25 mm focal length lens, which focuses it onto a 1.5 mm APD detector. At the next beam-splitter, a (BS 2) H_2O signal is extracted using an interference filter IF2 at 407.4 nm center wavelength with 4.8 nm bandwidth. Beam-splitter (BS 3) reflects the signal with wavelengths between 385 nm and 395 nm and is used for separating the N_2 signal, which is extracted by IF 3 with a central wavelength of 386.5 nm and bandwidth

of 5.2 nm. The light after BS 3 is used for two polarized Mie channels, where the P and S polarizations are separated by a polarization beam-splitter (PBS) and filtered by two 355 nm filters of the same type (IF 4). The five signals that come through the spectroscopic filter are converted into electrical signals using Hamamatsu photomultiplier tubes in the UV spectrum and an EG&G avalanche photodiode in the IR part of the spectrum. The Hamamatsu H1949-50 photomultiplier tubes operating at 2500 V are used for the Raman channels, while the HamamatsuH2341-50 photomultiplier tubes operating at 3000 V are used for Mie-Rayleigh channels.

5.3.3 Data retrieval and analysis

Output signals from the photomultiplier tubes and the avalanche photodiodes were amplified and digitized by Licel transient recorders TR40-160, providing analog and photon counting detection chains. For the analog detection chain, the signal was amplified according to the selected input range and digitized by a 12-bit A/D converter at 40 MHz. A hardware adder was used to write the summed signal into a 24-bit-wide RAM. Simultaneously, the signal was also amplified in the photon counting detection chain. A 250 MHz discriminator detected every photon event above the selected threshold voltage, which had 64 different discriminator levels and two different preamplifier settings. Then, the photon counting signal was written to a 16-bit-wide summation RAM, which allowed averaging up to 4094 acquisition cycles. Both detection chains provided a range resolution of 3.75 m and a maximum detection range of 61.4 km.

Licel transient recorders are connected to a Linux-based data acquisition (DAQ) computer through an Ethernet link. The DAQ uses custom software, which is partially based on the software of lidars used for the Pierre Auger Observatory [131, 132, 133]. The DAQ software is written in C++ with use of the support packages CERN ROOT[13] and QT[14]. The latter is used for a graphical user interface, which allows easier setting and operation of the lidar system, including real-time lidar return information to monitor data quality. The ROOT package is used for data handling and storage, saving parameters, and digitized lidar return traces into tree-structured ROOT native binary files.

For the analysis, a custom set of codes is used. Codes are written in C++ using the ROOT package for the data reading and plotting, performing analysis and plotting in a single step. The final products are then stored in new tree-structured ROOT files or directly as an image in png format. The analysis code can be semi-interactive using a graphical user interface written in Python3, allowing the user to change data files easily, set limits on time intervals, and set a maximum height of the plotting region.

[13] `https://root.cern.ch/`

[14] `https://www.qt.io/`

5.4 *In situ* measurements

The constituents of clouds were sampled at the Atmospheric Observatory of the University of Nova Gorica at Otlica so that the partitioning of bioaerosol particles between the condensed and the interstitial phase could be investigated. A total of 24 aerosol samples were collected (Table B1). The interstitial and coarse aerosol particles were collected simultaneously $\sim$2 m above ground. The interstitial inlet, which was a large inverted metal container with a diameter of 63.6 cm, was coupled with a BioSampler (SKC Ltd) with a flow rate of 11-12 l/min. The inlet was chosen in such a way that the settling velocities of particles $>5\,\mu$ m (with a density close to water droplets) were larger than the updraft force created by the sampling flow of the BioSampler. A virtual impactor (VI) was used to enhance the collection of supermicron particles, i.e., cloud droplets. The VI was coupled to a BioSampler and was operated at a total-to-minor flow ratio of 6.3-7.3. To prevent contamination, the tubing connecting the inlets to the BioSamplers was washed with 70% ethanol before each of the three sampling campaigns. The sampling liquid used in the BioSamplers was either 0.9% NaCl solution for ambient temperatures above 0 °C, or 20% NaCl solution for ambient temperatures below 0 °C. The samples were fixed with glutaraldehyde and stored at -20 °C for analysis.

Figure 5.4: The sampling setup at the Otlica Observatory in working conditions. The inverted metal container served as an interstitial inlet, which, in combination with the BioSampler, was used for the collection of particles smaller than 5 μm.

Flow cytometry was used to analyze the cell concentration and autofluorescence in the samples. Two flow cytometers were used, the 3-laser Aurora (Cytek Biosciences) and the 5-laser ID7000 (Sony). A forward scatter threshold of 50,000 (Aurora) or 150 (ID7000) was set. The samples were stained with SYBR Green I nucleic acid gel stain at a 5× final concentration and incubated for 15 minutes in the dark before analysis. Unstained samples were used as controls, and auto-fluorescent populations were analyzed for selected samples.

From the obtained samples, DNA was extracted using the DNeasy PowerSoil Pro Kit (Qiagen, Hilden, DE) from 250 μ l aliquots of individual samples [134]. The relevant bacterial and fungal genes were amplified using modified Illumina Metagenomic Sequencing Library Preparation guidelines[15]. Amplicon sequencing of bacterial 16S rRNA genes and the fungal ITS region was used to determine the community composition of the bioaerosols.

Bioinformatic analyses were performed using the R[16] package v4.1.2 [135]. Trimming and primer removal were done with Cutadapt v0.1.1 [136]. 'DADA2' v1.18.0 [137] was utilized for error correction, ASV calling, chimera removal, and taxonomic classification. The Silva SSU reference database nr. 138 was employed for the taxonomic classification of bacteria, and the 2021 UNITE 'general fast release for fungi 2' was used for fungal ITS [138, 139]. Decontamination was carried out using pooled sampling controls, nucleic acid extraction blanks, and PCR negatives with the R package Decontam v1.10.0 [140] using the prevalence method with a threshold of 0.1. Custom R scripts were used for all further data analysis, including PCA and PERMANOVA on clr transformed read counts and differential abundance analysis between interstitial and coarse samples for October and December 2020 samples using paired Wilcoxon signed rank tests with adjusted p-values for false discovery rate using the Benjamini & Hochberg method and a significance cutoff of 0.05.

Droplet freezing experiments were performed over a temperature range between 0 °C and -28 °C using the PINGUIN [141] setup (Plate based ice nucleation detection in gallium with an infra-red camera) to quantify the ice nucleating particles in the course and the interstitial samples. Starting with an ambient temperature, the temperature was decreased at 1 K/min until -28 °C. The individual temperatures were recorded using the FLIR A655sc w/25 thermal camera calibrated with a thermistor (TE Connectivity 2.252 kΩ) mounted in a fix-point cavity. The freezing events were determined using custom-made software based on the lateral heat release caused by the nucleation. The negative control for each run was MQ water filter-sterilized using a syringe filter (0.22 μm pore size, Millipore, Massachusetts, USA). Sampling control for each sample was also included in the analysis. Based on the frozen fractions [142], we

[15] https://support.illumina.com/documents/documentation/chemistry_documentation/16s/16s-metagenomic-library-prep-guide-15044223-b.pdf

[16] https://www.r-project.org/

calculated the number of ice nucleation active sites per volume of air $N_V(T)$ as:

$$N_V(T) = \frac{-\ln(1 - f_{ice}(T))}{V_D \times V_{air}} \times V_{tot} \times d. \tag{5.1}$$

Where V_D the droplet volume, V_{tot} the total volume of sample, $f_{ice}(T)$ is the fraction of frozen droplets at a given temperature, d is the dilution factor and the V_{air} the volume of air collected for each sample.

5.5 Results

The measurement campaign yielded 12 data-taking events during three distinct periods (22-24 October 2020, 1-4 December 2020, and 19-22 December 2020, table B1). In the first period in October, the depolarization ratio of clouds at observatory height was mostly low, with values between 0.5% and 4%, suggesting that the cloud content was predominantly water droplets [89]. In the following two periods in December, the depolarization ratio values were between 8% and 20%, indicating the presence of nonspherical particles. It still does not reach values commonly associated with purely ice clouds, so we assumed the presence of mixed-phase clouds [89]. It was verified that the depolarization ratio is linearly correlated with *in situ* measured minimum temperature (-0.66 ± 0.11, Fig. 5.5) and was thus used as an indicator for phase state of the cloud in the further analysis of bioaerosols.

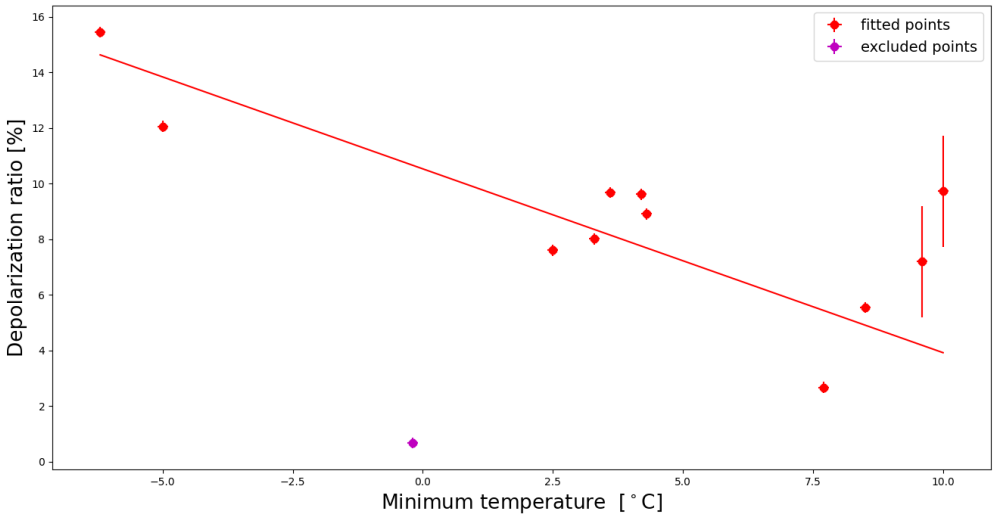

Figure 5.5: Linear correlation between depolarization ratio and minimum temperature at sampling site with a correlation coefficient of -0.66 ± 0.11. The data point in magenta corresponds to the case when there was no cloud at measurement height and was not used for the calculation of the correlation. The accuracy of depolarization measurement was 0.2% for thin clouds and 2% for thick clouds with multiple scattering [43]. The accuracy of the temperature measurements was 0.1 °C.

The increase of depolarization indicating the presence of ice crystals could also be a misinterpretation of the depolarization ratio change due to multiple scattering. As the investigated cloud layer was initially relatively thin in 9 out of 12 cases (no more than 200 m, see Fig. 5.6), the number of multiply scattered photons was expected to be low. Simultaneous measurement of the depolarization ratio in a second, thick, and elevated cloud layer (above 1500 m a.s.l.) was found to be considerably higher, exceeding 30%, as well as the depolarization values obtained when both layers merged later in the day, both confirming our expectations. In contrast, the depolarization ratio was close to 0% on a clear day and close to 10% on two days when the cloud layer was thick with no ice crystals due to high temperatures. The data point with no cloud was excluded from correlation analysis as the samples obtained were not representative.

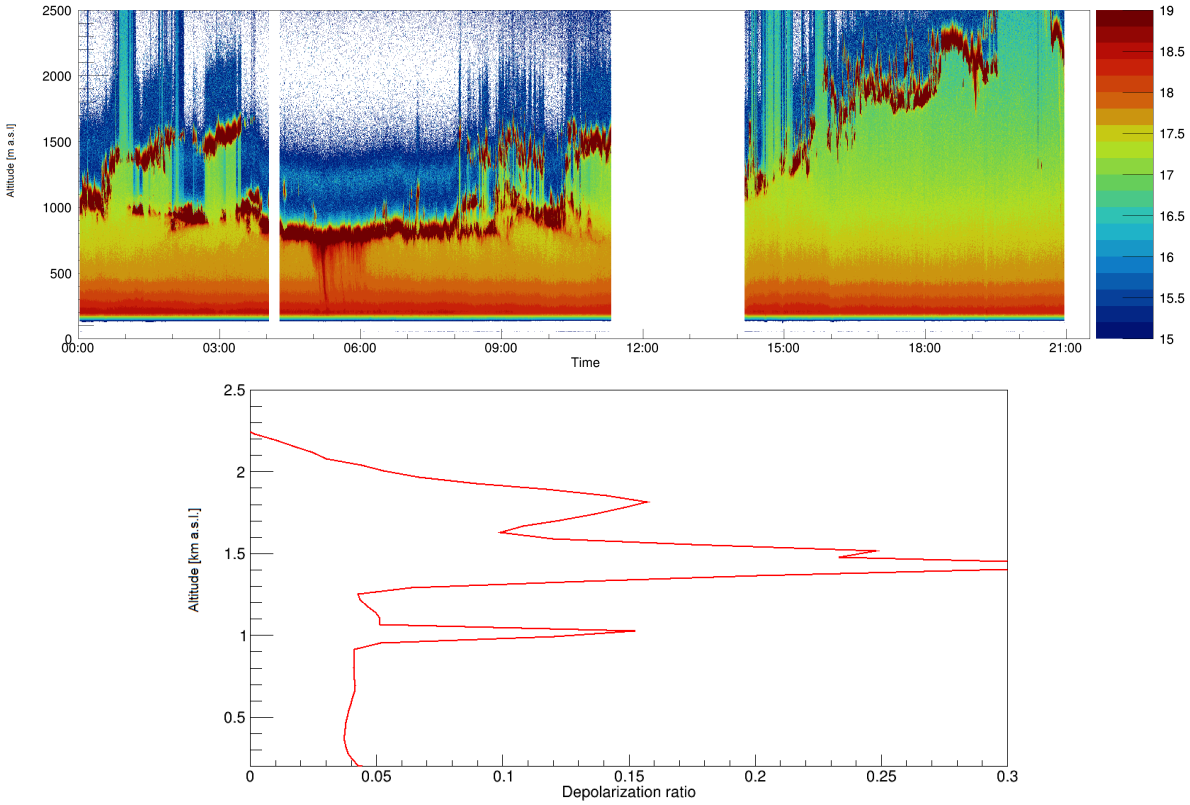

Figure 5.6: Lidar data from 4 December 2020. **Top:** Logarithm of the range corrected backscattered signal at 355 nm shows temporal variation of aerosol loading over the Vipava Valley. In the morning, two layers of clouds are visible. The lower layer is at the same height as the Otlica Observatory. **Bottom:** Depolarization ratio profile between 1 AM and 1:30 AM shows the presence of two cloud layers at about 1000 m a.s.l. and 1500 m a.s.l. The depolarization of 15% in the lower layer implies mixed-phase clouds. In the upper layer, lidar signal gradually disappears due to high optical thickness of the cloud. High depolarization peak at the bottom of this layer, which is due to multiple scattering, and its gradual decrease with height imply the presence of mixed phase aerosols in this layer as well.

Bioaerosols were found in most samples in all 12 data-taking events at concentrations significantly higher than controls. The bacterial communities were found to be dominated by Gammaproteobacteria, Alphaproteobacteria, Actinobacteria, Bacilli, and Cyanobacteria. In contrast, the fungal communities were mainly composed of Basidiomycota affiliated with Agaricomycetes and Tremellomycetes (Fig. 5.7). Concentrations of interstitial bioaerosols (4.5×10^5 m^3 on average) were found to be significantly higher than those of coarse bioaerosols (1.2×10^5 m^3) (Fig. 5.8A), indicating that most bioaerosols did not activate into cloud droplets at supersaturated conditions. Low wind speed, temperatures around 0 °C, and the absence of or low precipitation did not significantly affect total bioaerosol concentrations.

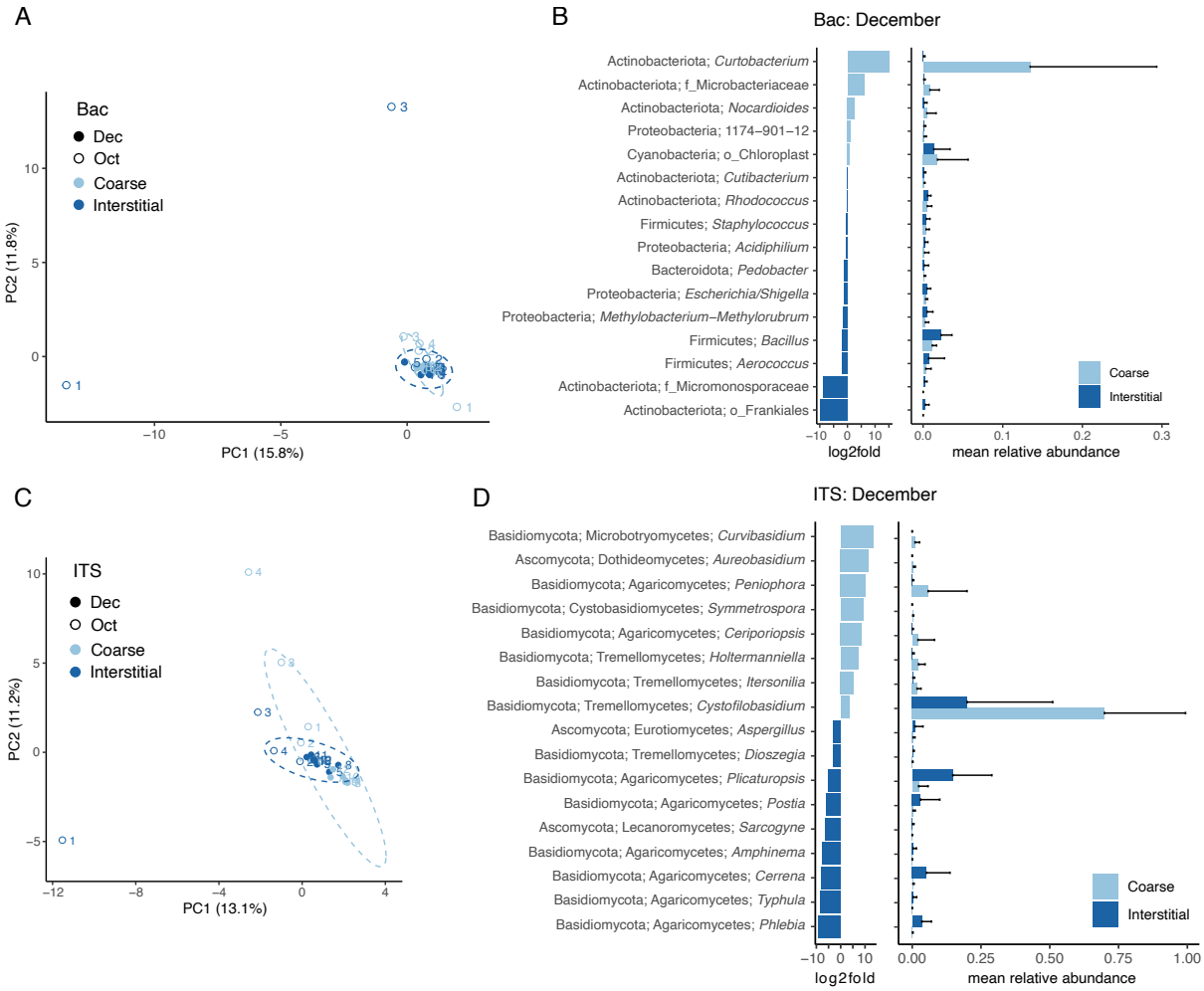

Figure 5.7: Microbiome analysis of bacterial 16S rRNA gene sequences (A, B) and fungal ITS sequences (C, D). (A, C) PCA plot of clr transformed read counts, closed and open symbols show December and October samples, respectively. Color coding shows coarse and interstitial samples according to legend. (B, D) Differentially abundant genera in December between coarse and interstitial samples (Wilcoxon signed rank tests, $p<0.05$). The first bar plot shows log2-fold chance, the second bar plot shows the mean relative abundance (+SD).

No significant differences between interstitial and coarse communities for bacteria were found, but significant differences for fungi were observed. A differential abundance analysis revealed 16 bacterial and 17 fungal genera (Fig. 5.7) that were differentially abundant in one of the cloud phases. Most differentially abundant genera represented a minor fraction of the total community. Most bacterial and fungal taxa cells had a comparable, i.e., poor ability to act as CCN regardless of their size, physiology, or surface properties, as they were distributed evenly between the interstitial and coarse phase.

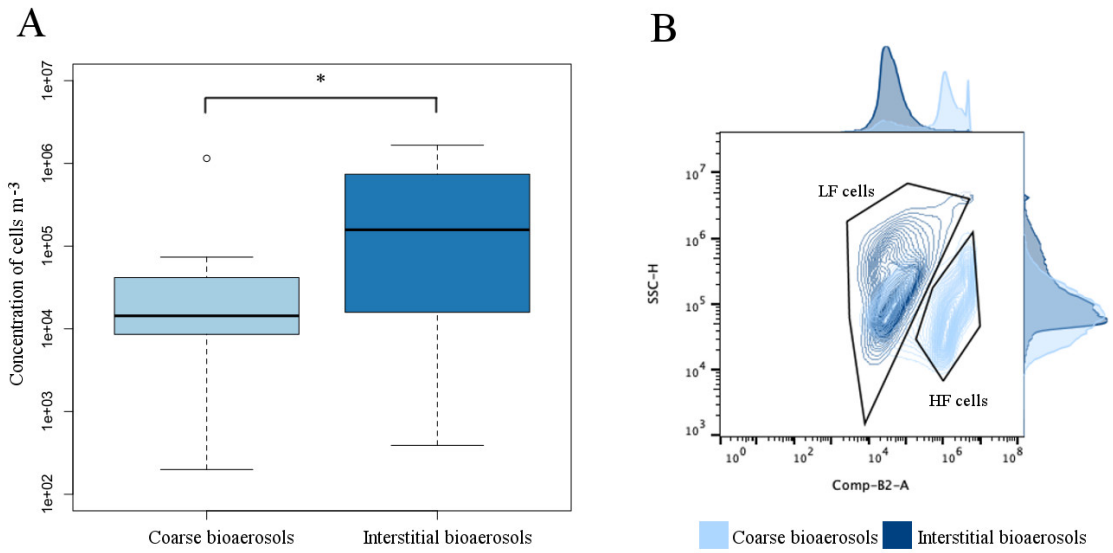

Figure 5.8: The concentration of microbial cells m^{-3} for the coarse and interstitial phase of the cloud as determined by flow cytometry. The "$*$" sign indicates a significance level of $p<0.05$ for differences between interstitial and coarse communities of bioaerosols. A plot dot obtained with the Aurora (Cytek Biosciences) spectral flow cytometer showing the side scatter of cells as a function of fluorescence in the B2 channel (emission wavelength of 528 nm, when excited with the blue laser) for a pair of coarse and interstitial samples (collected on 19 December 2020). While low fluorescent (LF) cells are present in both phases, high fluorescent (HF) cells are present only in the coarse phase. Adjunct histograms are shown for each of the phases and parameters (side scatter and B2 fluorescence).

Notable exceptions were cells of *Cystofilobasidium* sp. and *Curtobacterium* sp. were found to be very good CCN, preferentially found in the coarse bioaerosol fraction. These cells were characterized by an elevated autofluorescence (significantly higher than other microbial cells, Fig. 5.8B) corresponding to oxidized flavins, which suggests that atmospheric aging enhanced their ability to act as CCN. When excited with the blue laser at 488 nm, the fluorescence at 528 nm was on average $8.3 - 14.8\times$ higher compared to the regular population. These types of microbial cells formed between 15% and 77% of the entire coarse bioaerosol sample. We also found that this autofluo-

rescent population exhibits larger forward and side scattering compared to the regular population of cells, indicating that these cells are either larger or form aggregates.

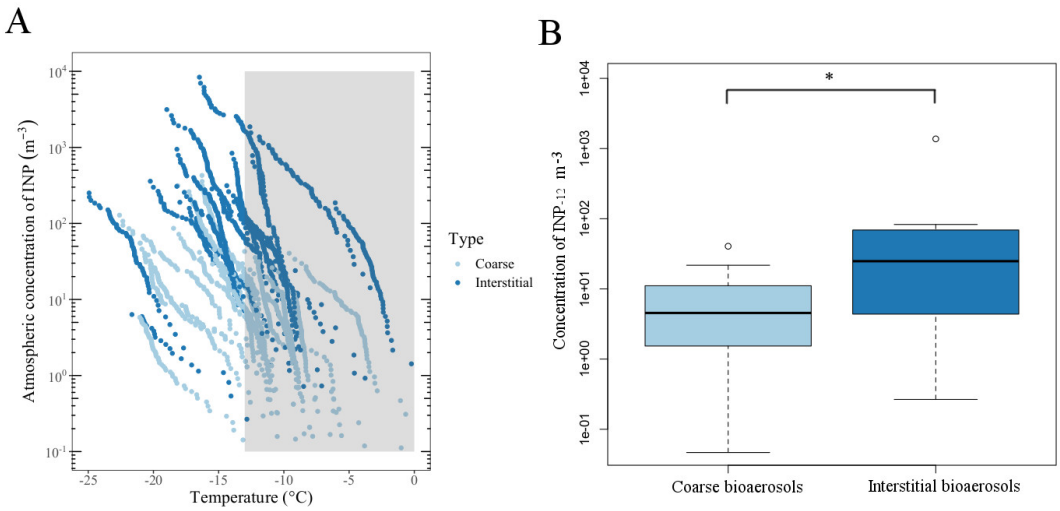

Figure 5.9: **A:** Concentration of INP as a function of nucleation temperature in the coarse and the interstitial cloud fraction. The shaded area denotes biogenic INP. **B:** Concentration of INP_{-12} in the coarse and the interstitial cloud fraction. The "$*$" sign indicates a significance level of $p<0.05$ for differences between interstitial and coarse communities of bioaerosols.

In two December 2020 periods, where lidar data implied the presence of ice crystals in the sampled cloud, the partitioning of ice-nucleating particles between the interstitial and the coarse cloud phase was assessed through the concentration of INP as a function of their nucleation temperature. Using the PINGUIN cold-stage instrument, it was discovered that the majority of samples (83%) contained INP that were active at temperatures equal to or colder than –13 °C, indicating that these INP were associated with ice nucleating proteins carried by bioaerosols. There was a positive correlation between the concentration of INP active at -12°C and bioaerosol concentration, supporting their biogenic origin. The concentration of INP in the interstitial aerosols was found to be higher than in the coarse aerosols. The average concentration of INP active in the interstitial aerosols at –12 °C was 142.2 INP_{-12} m^{-3} (Fig.5.9B). The ability of these biogenic INPs to act as CCN was found to be low.

The correlations between depolarization ratio and aerosol concentration were also investigated. In the coarse sample, it was found to be decreasing exponentially (as $e^{-\mu DR}$ with $\mu = 0.6 \pm 1.1$) with depolarization (Fig. 5.10). In contrast, the aerosol concentration in interstitial samples does not seem to be affected. This is probably due to the Wegener–Bergeron–Findeisen process [143], where, in the presence of ice crystals, the ambient pressure falls below saturation vapor pressure for droplets but not for ice crystals. This leads to the evaporation of water droplets with bioaerosols in them, and as such, they end up in the interstitial instead of the coarse samples.

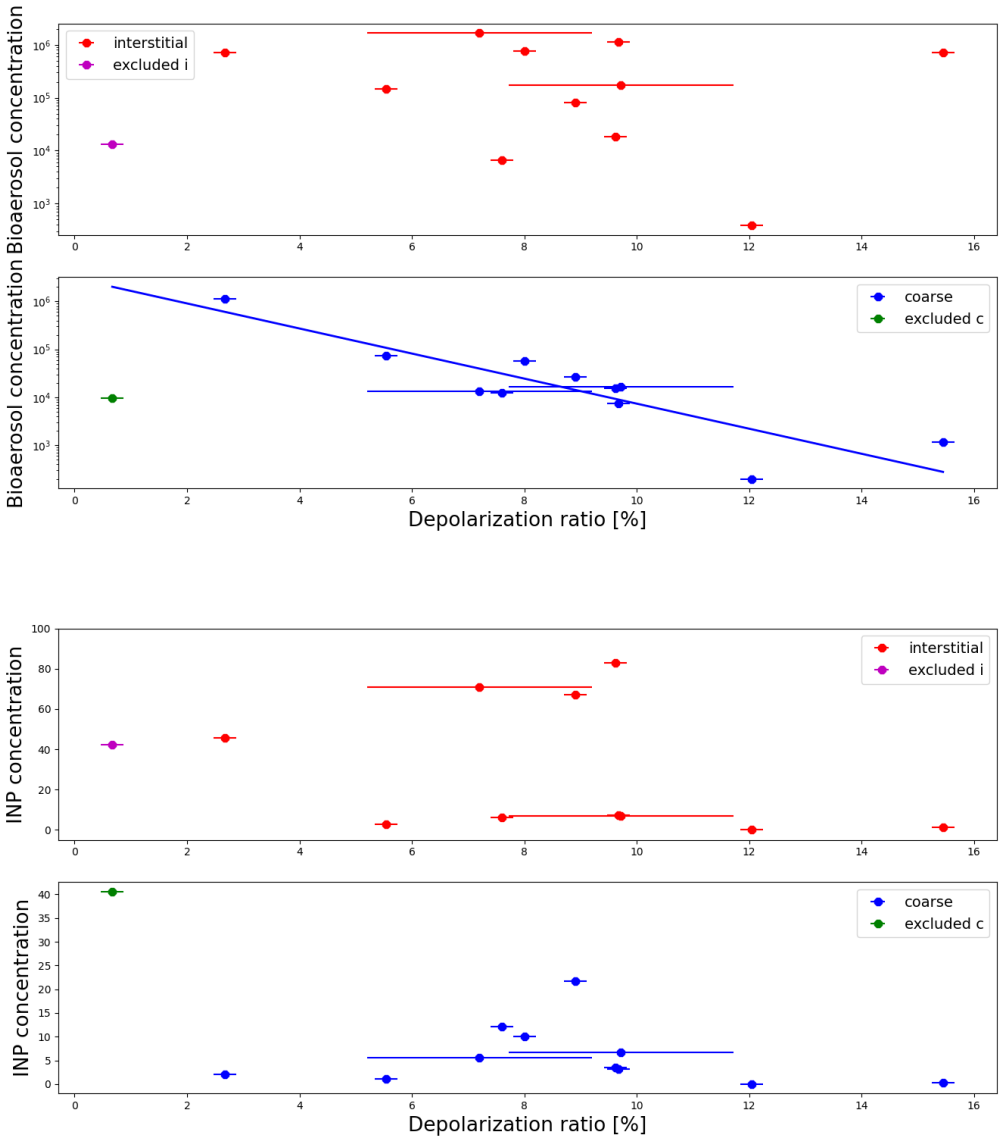

Figure 5.10: Comparison of depolarization dependence of bioaerosol (top) and INP (bottom) concentrations in interstitial (red) and coarse (blue) samples. Bioaerosol concentration in coarse samples was found to be decreasing exponentially with increase in depolarization, while the rest (aerosol interstitial, INP interstitial and INP coarse) remain constant. The data points in magenta(interstitial)/green(coarse) corresponds to the case when there was no cloud at measurement height and was not used in the calculation of the correlation.

The dependence of the ratio of the most abundant genus of bacteria *Pseudomonas* sp. present in both coarse (top) and interstitial (bottom) samples with respect tot the total bacteria content was also investigated. It was found that, with the increase of

depolarization ratio, the content ratio of these bacteria was decreasing as -2.52 ± 1.14 in the coarse sample and increasing as 1.62 ± 0.74 in the interstitial sample (Fig. 5.11). This result suggests that the species of *Pseudomonas* present in the studied clouds were poor INP, as they were less abundant during conditions when there was ice buildup in the clouds.

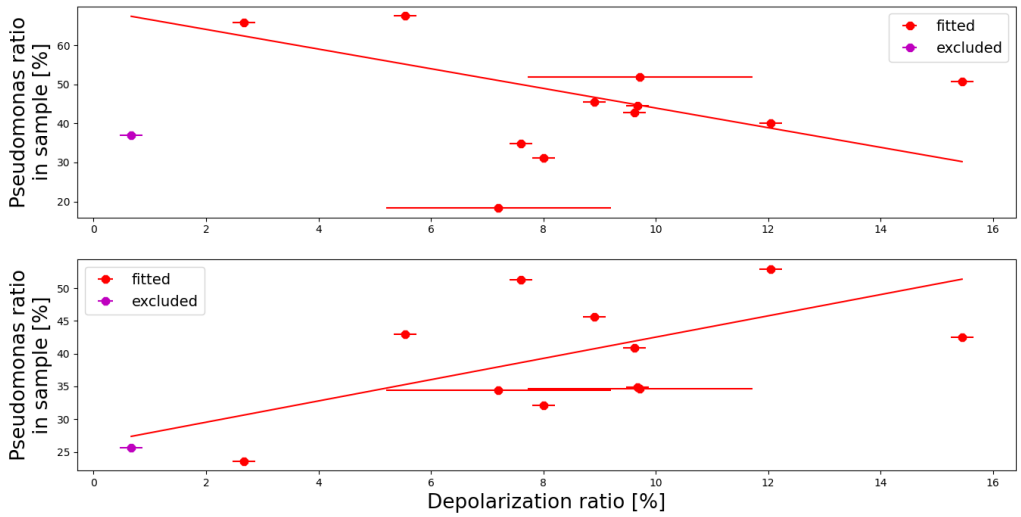

Figure 5.11: Ratio of *Pseudomonas* sp., the predominant bacteria genus, in coarse (top) and interstitial (bottom) sample with respect to depolarization. Linear fit shows a decreasing trend (-2.52 ± 1.14) in the coarse sample and an increasing trend (1.62 ± 0.74) in the interstitial sample. The data points in magenta corresponds to the case when there was no cloud at measurement height and were not used in the calculation of the correlation.

To conclude, based on the lidar information on the phase state of clouds, the effects of bioaerosol presence and their ability to act as CCN or INP were investigated. Despite relatively high bioaerosol concentrations observed, these are still between 1 and 7 orders of magnitude smaller than the typical non-biological CCN or cloud droplet concentrations in the atmosphere [122]. We observed that bioaerosols at *in situ* supersaturated conditions were mainly found in the clouds interstitial phase, suggesting they were poor CCN. The exception was cells of *Cystofilobasidium* sp. and *Curtobacterium* sp., containing an elevated level of autofluorescent molecules, which were in abundance in the coarse sample and clearly acted as very good CCN, much better than the cells with none or lower levels of these molecules. In the mixed phase and ice clouds, modeling suggests that INPs are inefficient when competing with very hygroscopic CCN for water vapor [144]. The predominant ice nucleation mode is immersion freezing of CCN [145] and not INP. The inability of bioaerosols to act as CCN could inhibit their ice-nucleation activity *in situ*. In agreement with this, in mixed-phase clouds as well as most bioaerosols were discovered in the interstitial phase, suggesting the same poor ability of bioaerosols to act as biogenic INP as for CCN.

6

Conclusions and prospects

The primary aim of this work was to test the capabilities of the Barcelona Raman Lidar (BRL), which is the prototype for the CTAO-North Raman lidar for atmospheric characterization at La Palma and to develop the necessary analysis tools for its data. Based on the BRL performance, the final device will be constructed to become a part of the support infrastructure for the northern site of the Cherenkov Telescope Array Observatory (CTAO). Detailed mapping of optical depth is crucially important for Cherenkov gamma ray astronomy, where the properties of primary high energy cosmic photons (CR) are derived from the flashes of Cherenkov light that showers of secondary particles create in the atmosphere. The ever-changing atmosphere accounts for the major part of systematic uncertainties in determining CR energy and direction, which must be determined with an accuracy below 10%. In this case, lidar is an ideal monitoring device since it can quickly retrieve UV and visible light backscattering properties within the CTAO's detection volume. Due to similar wavelengths of the Cherenkov light from CR and BRL UV lidar pulses, the obtained optical depth can be applied as a correction to the measurements of CTAO Cherenkov telescopes. We demonstrated that the BRL can also be used as a meteorological lidar with the capabilities for basic aerosol classification, which are limited, as it was not primarily designed for this task.

The test campaign of the Barcelona Raman lidar, performed between March 2021 and April 2022 at the Roque de los Muchachos Observatory at La Palma, was aimed at confirming the adequacy of the BRL design for CTAO. Its performance and behavior were checked in a natural working environment, and its various modes of operation were tested and debugged. The relatively limited dataset obtained is, to some extent, due to BRL integration problems into the LST-1 site safety interlock system, which will be addressed in the future integration of the Raman lidar into CTAO controls. Based on this campaign we conclude that the lidar design is suitable, but the device itself needs to be more robust in its final version. Apart from the lessons learned about the device itself, which will be implemented in its new version (new laser, new electronics for gating of PMT signals, new control system), BRL has been shown to

perform well in the measurements of backscattering and extinction coefficients, both needed for CTAO calibration, in all weather conditions. As the sole operating Raman lidar in La Palma during its commissioning period, it provided interesting details about the atmosphere's physical properties above La Palma for selected high aerosol content cases.

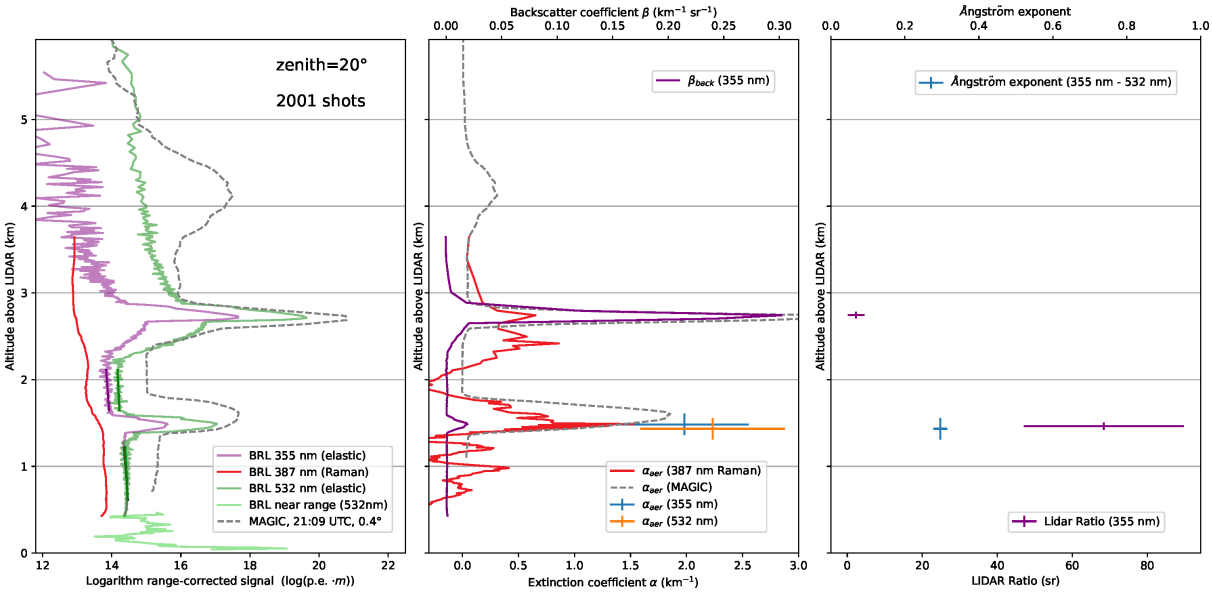

Figure 6.1: The plot of direct comparison between BRL and MAGIC lidar return signals. Data from MAGIC lidar system was provided as a courtesy of the MAGIC Collaboration[17] for comparison. **Left:** Range square corrected lidar returns in the three analog channels where purple at 355 nm and green at 532 nm are elastic, and red at 389 nm is the Raman backscattering channel. The dashed line is MAGIC 532 nm backscattering return signal. The measurement with BRL was performed at a zenith angle of 20° with 2001 laser shots at 10 Hz rate. **Center:** The backscattering coefficient retrieved from 355 nm channel in purple and the extinction coefficient of aerosols retrieved from Raman 389 nm channel in red. The blue and orange points are aerosol extinction coefficients retreived using Klett inversion from BRL data and dashed line is the extinction coefficient retreived using Klett inversion from MAGIC lidar data.**Right:** The lidar ratio for 355 nm channel in purple and Ångström exponent (355 nm-532 nm) in blue calculated from the BRL data.

The results obtained during Tajogaite eruption in September 2021 were cross-checked using preliminary analysis based on the data collected by the MAGIC elastic lidar approximately one hour later. Return signal profiles of both devices show the same atmospheric structure (an additional level of clouds developed at a higher altitude during MAGIC mesurements, Fig. 6.1). The same also applies to the extinction coefficients from both experiments. In the Calima event, there were no other lidars at ORM taking data that could be used for comparison, however, the values obtained for the

[17] `https://magic.mpp.mpg.de/`

Ångström exponent and lidar ratio agree within their uncertainty with published ones for similar conditions [113, 114, 115]. Test campaign results confirm that the analysis software written specifically for the BRL is performing correctly, as the results are in good agreement with those from other studies of the same/similar phenomena and are also confirmed by satellite images taken at the same time.

The BRL and its successor, the CTAN Raman lidar, are not intended to act as meteorological lidars and their design is limited by strict CTAO requirements. The purpose of the final CTAO lidar is to provide optical depth profiles along the field of view of Cherenkov telescopes, which can point at an arbitrary direction in the sky, as quickly as possible to minimize the gaps in the CTAO observation time. Consequently, the device must be as compact, light and simple as possible and the inclusion of non-essential components is not allowed. The device is expected to operate with as few interruptions as possible for at least ten years, throughout a considerable part of the life cycle of the observatory. This implies that CTAO lidar will not perform optimally for aerosol characterization, which is interesting from meteorological and environmental aspects, but not so much for astrophysical purpose of the CTA observatory. We have demonstrated that it nevertheless provides a very interesting observation window into selected processes in the atmosphere with its existing capabilities. The cases presented in Chapter 4. show that the system is perfectly capable of providing information on different aerosol structures above the observatory, even with limited BRL prototype functionality (the second Raman channel was not available). When the device is fully functional, careful calibration can allow it to provide additional measurements of meteorological parameters, such as temperature profile, which would also be of interest to CTAO, and in combination with other support instruments of the observatory, can be used for complete atmospheric monitoring of the La Palma location.

To exploit the full potential of aerosol classification, which is to a degree possible with BRL but will not be implemented in a CTAO Raman lidar, a re-disign of the polychromator would be needed and the addition of another optical and electronic readout chain for the detection of polarization change of the emitted laser pulses. Full aerosol characterization capability may be useful in specific cases of aerosols from multiple sources at various elevations above La Palma, but is not needed for regular CTAO operation. The possible benefits of such lidar configuration for atmospheric science were investigated using a conceptually similar device (the University of Nova Gorica polarization Raman lidar, which was found to be very useful tool in determination of aerosol types [65]). We demonstrated its capability of identifying the thermodynamic phase of clouds based on the depolarization of backscattered light. The test campaign was focused on the assessment of capability of bioaerosols to act as cloud condensation nuclei (CCN). Most of them were acting as poor CCN, which in addition to much lower amount of bioarosols with respect to other aerosols even further reduces their importance in ice nucleation process. The exception were cells of *Cystofilobasidium* sp. and *Curtobacterium* sp., predominantly found in the coarse sample and almost

nonexistent in the interstitial sample. Their ability to act as CCN might be due to an elevated level of autofluorescent molecules present in these particular species. The most abundant bioaerosol in our samples was a bacteria from the *Pseudomonas* sp., a species that is usually regarded as one of the better bioaerosol CCN. The concentration of our specific bacteria type from the *Pseudomonas* sp. in the coarse phase shows a strong anti-correlation with depolarization, suggesting that at least this particular bacteria acts as a poor ice nucleation particle (INP).

6.1 Future plans

With the testing phase of BRL finished in 2022, the group's main efforts are now focused on evaluating the experience and data collected with the prototype. Lessons learned will be implemented in the design of the next version of the Raman lidar that will act as a permanent monitoring device at the CTAO-North site. The BRL prototype demonstrated that the design is sound and can satisfy the CTAO requirements, but there is still room for improvement. First, the security system, based on interlock switches to prevent operation if somebody enters the operating area, was very unreliable (both on the LST-1 as the BRL side) and was causing many problems during lidar operation (resulting in loss of data), so this part needs a complete redesign. The second issue found is the shielding for the outgoing laser pulses. The BRL is of a monostatic coaxial design, but at the device level, it starts as a monostatic biaxial with a telescope and laser placed parallel to each other. The laser beam is redirected in front of the primary mirror using two unprotected dichroic mirrors to achieve coaxial configuration. Any stray light may not be directed toward the sky and could enter the field of view of other telescopes or present a danger to people at the observatory. Shaders shall be installed so the light can only travel in the desired direction to eliminate this danger. Thirdly, as we experienced saturation of PMT signal returns in all channels below a certain range when operating at an elevated laser power, the use of PMT gating shall be implemented. The approach will be similar to the one used for the LUPM lidar prototype, with PMT gating electronics to remove excess signals from close range and to shield the PMTs from overloading. Finally, as the lidar will be operated remotely, a new, comprehensive, and easy-to-use graphical user interface (GUI) for the operator to work with shall be implemented (the testing was performed in a terminal in expert mode). In addition to a GUI for operation, the lidar shall get an automated low-level data analysis to quickly produce inputs for calibrating data collected by CTAO Cherenkov telescopes. Along with this, the high-level analysis codes shall be as generalized as possible to provide an easy-to-use platform for any future meteorological or environmental measurements of atmospheric properties above La Palma.

Appendix A

La Palma campaign measurement list

Table A1: The entire dataset was taken with the CTA-N Raman lidar pathfinder prototype during its commissioning at the Observatorio Roque de los Muchachos, La Palma, in the period March 2021 – April 2022. Data were acquired during 33 moonlit nights in different atmospheric conditions. Heights are relative to the lidar, which was deployed at 2200 m a.s.l. The table is arranged so that in the first column is the date on which a measurement is performed, in the second is the number of runs performed that day and the total amount of laser pulses fired that night, the third column is a reference to any atmospheric features visible in the measurement, such as clouds or Calima. The approximate height of the beginning of a cloud is marked next to its mention. An elevation scan gives information on whether a measurement was performed; pointing lidar in single or multiple directions, measuring only on max angles (zenith 0° and zenith 60°) in the same night is not considered a scan. In the final column, there are listed data problems occurring: low detection or missing channels are probably associated with lowered voltages on photomultiplier tubes and are shown in data as very low or completely missing signals (PC stands for photon counting on specific channels), noisy stands for low signal to noise ratio, near range (NR) oscillations are probably associated with some electronic noise and are shown in the plots as regular increase and decrease of NR magnitude; finally, there are some runs with no clear signal, these were taken without operating a laser. In the case when the signal is good until a certain height (which is lower than the expected height), the height is specifically mentioned.

Date	**Runs / events**	**Atmospheric features**	**Elevation scan**	**Specific settings and problems**
25.03.2021	1 501	Clear sky	No	analog ch. low detection noisy
29.03.2021	13 10013	Clear sky	No	elastic PC ch. low detection noisy
21.04.2021	2 1002	Clear sky	No	no signal in first run elastic PC ch. low detection

22.04.2021	5 5005	Calima	No	no signal in first run elastic PC ch. low detection
23.04.2021	6 6006	Calima	No	no signal in first run elastic PC ch. low detection
21.05.2021	8 6507	Cloud at 250 m	No	elastic PC ch. low detection noisy
23.05.2021	8 5508	Clear sky	No	elastic PC ch. low detection noisy no signal in first run
27.05.2021	22 23522	Cloud at 4500 m	No	355 nm PC ch. low detection 532 nm PC ch. low detection noisy
28.05.2021	3 3003	Clear sky	No	355 nm PC ch. low detection 532 nm PC ch. low detection noisy NR oscillations above 500 m
29.05.2021	5 5005	Clear sky	No	355 nm PC ch. low detection 532 nm PC ch. low detection noisy above 2000 m
21.06.2021	14 14014	Clear sky	No	355 nm PC ch. low detection 532 nm PC ch. low detection NR oscillations above 500 m
22.06.2021	19 19019	Calima	No	355 nm PC ch. low detection 532 nm PC ch. low detection NR oscillations above 1000 m
23.06.2021	3 6003	Clear sky	No	355 nm PC ch. low detection 532 nm PC ch. low detection NR oscillations above 1000 m
24.06.2021	4 4004	Clear sky	No	355 nm PC ch. low detection 532 nm PC ch. low detection NR oscillations
25.06.2021	6 9006	Clear sky	No	elastic PC ch. low detection NR oscillations above 500 m
18.08.2021	21 10521	Clear sky	Yes	355 nm PC ch. low detection 532 nm PC ch. low detection NR oscillations above 500 m
19.08.2021	10 5010	Clear sky	Yes	elastic PC ch. low detection NR oscillations above 500 m
23.08.2021	10 12010	Clear sky	Yes	elastic PC ch. low detection NR analog ch. low detection NR oscillations above 500 m
25.08.2021	20	Clouds at	Yes	355 nm PC ch. low detection

	18020	500 m		355 nm PC ch. low detection noisy NR oscillations
26.08.2021	20 12020	Clear sky	Yes	355 nm PC ch. low detection 355 nm PC ch. low detection noisy above 3 km NR oscillations
18.09.2021	5 15005	Clear sky	No	355 nm PC ch. low detection 355 nm PC ch. low detection noisy above 3 km NR oscillations
19.09.2021	3 12003	Clear sky	No	355 nm PC ch. low detection 355 nm PC ch. low detection noisy above 3 km NR oscillations above 500 m
20.09.2021	28 2828	Clear sky	Yes	noisy NR oscillations elastic PC ch. low detection
21.09.2021	15 15015	Volcanic plume	Yes	noisy NR oscillations above 500 m elastic PC ch. low detection
22.09.2021	8 16008	Volcanic plume and cloud 2.8 km	Yes	elastic PC ch. low detection NR oscillations
11.01.2022	12 1212	Clear sky	No	noisy NR oscillations elastic PC ch. low detection no signal in first run
18.02.2022	10 10010	Clear sky	No	NR oscillations above 1000 m quick decay of 532 nm ch. strange PC signals no signal in several runs
17.03.2022	17 17017	Clear sky	No	NR oscillations noisy 532 nm ch. PC signals fast decay no signal in several runs
18.03.2022	16 16016	Cloud at 7500 m	No	NR oscillations missing Raman channels PC signals decay fast
19.03.2022	20 20020	Clear sky	No	NR oscillations missing Raman channels PC signals decay fast
13.04.2022	56	Clear	Yes	NR oscillations

49856	sky	noisy Raman channels PC signals decay fast

Appendix B

Ajdovščina campaign measurement list

Table B1: The entire lidar dataset and meteorological data were taken during the measurement campaign from October 2020 to December 2020. The table contains the start date and time, measurement duration, average and minimum temperatures recorded during the data taking, relative humidity, and the highest value of depolarization ratio. Lidar measurements at the UNG building in Ajdovščina were performed simultaneously with sampling at Otlica meteorological observatory, where the meteorological variables were also recorded. During each sampling, the interstitial (at a flow rate of 11.5 l/min) and coarse (at a flow rate of 75 l/min) samples were taken. Most of the time, the 0.9% NaCl sampling liquid was used, except in the measurements from 2 December to 4 December when 20% NaCl sampling liquid was used. The lidar measurement resolution is 3.75 m. The first three columns of the table give information about the measurement start date, start time, and duration in hours, followed by the temperature averaged over the whole measurement duration and the minimum temperature measured during this time. The penultimate column gives the average relative humidity during the measurement, and the final column gives the maximum half-hour average of depolarization ratio measured at an altitude of 965 m a.s.l. during the measurement interval.

Start date	**Start time**	**Duration [h]**	**Average temp. [°C]**	**Minimum temp. [°C]**	**Relative humidity [%]**	**Depo. ratio [%]**
22.10.2020	10:15	3	8.7	7.7	98.3	2.67
23.10.2020	04:00	7	8.9	8.5	100	5.54
23.10.2020	11:45	8	10.1	9.6	100	7.20
23.10.2020	21:30	9	10.5	10	100	9.72
02.12.2020	13:30	8	-5.8	-6.2	90.3	15.45
03.12.2020	11:50	20	-2.2	-5	95	12.05
04.12.2020	10:00	9.5	1.3	-0.2	94.9	0.67
19.12.2020	08:20	11.3	3.9	3.3	100	8.01
19.12.2020	23:10	8.2	3.1	2.5	100	7.60

20.12.2020	09:30	12	4.8	4.3	100	8.91
20.12.2020	23:30	8.5	4.4	4.2	100	9.62
22.12.2020	11:30	5	3.7	3.6	100	9.68

References

[1] D. Bose, V. R. Chitnis, P. Majumdar, and B. S. Acharya. Ground-based gamma-ray astronomy: history and development of techniques. *The European Physical Journal Special Topics*, pages 1–24, 2021.

[2] M. Gaug. CTA Atmospheric Calibration. *EPJ Web Conf.*, 144:01003, 2017.

[3] J. J. Rodriguez-Franco and E. Cuevas. Characteristics of the subtropical tropopause region based on long-term highly resolved sonde records over Tenerife. *Journal of Geophysical Research: Atmospheres*, 118(19):10–754, 2013.

[4] P. Munar-Adrover and M. Gaug. Studying molecular profiles above the Cherenkov Telescope Array sites. volume 197, page 01002, 2019.

[5] C. Fruck, M. Gaug, A. Hahn, V. Acciari, J. Besenrieder, D. Dominis Prester, D. Dorner, D. Fink, L. Font, S. Mićanović, et al. Characterizing the aerosol atmosphere above the Observatorio del Roque de los Muchachos by analysing seven years of data taken with an GaAsP HPD-readout, absolutely calibrated elastic LIDAR. *Monthly Notices of the Royal Astronomical Society*, 515(3):4520–4550, 2022.

[6] F. Gao. *Study of processes in atmospheric boundary layer over land-sea transition interface using scanning lidar*. PhD thesis, 2012.

[7] L. Wang, S. Stanič, A. Gregorič, K. Bergant, M. Mole, and M. Vučković. Evolution of the planetary boundary layer in the presence of fog and plume. In *EGU General Assembly Conference Abstracts*, pages EPSC2016–15363, 2016.

[8] K. Bernlöhr. Impact of atmospheric parameters on the atmospheric Cherenkov technique. *Astroparticle Physics*, 12(4):255–268, jan 2000.

[9] M. Meyer, D. Horns, and H.-S. Zechlin. The Crab Nebula as a standard candle in very high-energy astrophysics. *Astronomy & Astrophysics*, 523:A2, 2010.

[10] D. Bastieri, G. Busetto, A. De Angelis, F. Longo, G. Piano, R. Rando, and A. Saggion. Energy Calibration of Cherenkov Telescopes using GLAST Data. In *International Cosmic Ray Conference*, volume 3, pages 1555–1558, 2008.

[11] A. Fraß, C. Köhler, G. Hermann, M. Heß, and W. Hofmann. Calibration of the sensitivity of imaging atmospheric Cherenkov telescopes using a reference light source. *Astroparticle Physics*, 8(1-2):91–99, 1997.

[12] A. Daum, G. Hermann, M. Hess, W. Hofmann, H. Lampeitl, G. Pühlhofer, F. Aharonian, A. G. Akhperjanian, J. A. Barrio, A. S. Beglarian, et al. First results on the performance of the HEGRA IACT array. *Astroparticle Physics*, 8(1-2):1–11, 1997.

[13] G. Pühlhofer, O. Bolz, N. Götting, A. Heusler, D. Horns, A. Kohnle, H. Lampeitl, M. Panter, M. Tluczykont, F. Aharonian, et al. The technical performance of the HEGRA system of imaging air Cherenkov telescopes. *Astroparticle Physics*, 20(3):267–291, 2003.

[14] F. Goebel, K. Mase, M. Meyer, R. Mirzoyan, M. Shayduk, and M. Teshima. Absolute energy scale calibration of the MAGIC telescope using muon images. *Part 3: MAGIC Detector and Analysis Details*, page 37, 2005.

[15] J. Ebr, J. Blažek, M. Prouza, D. Mandát, M. Pech, M. Mašek, J. Juryšek, P. Janeček, P. Kubánek, J. Eliášek, et al. Aerosol measurements with the FRAM telescope. In *EPJ Web of Conferences*, volume 144, page 01011. EDP Sciences, 2017.

[16] J. Ebr, S. Karpov, J. Eliášek, J. Blažek, R. Cunniffe, I. Ebrová, P. Janeček, M. Jelínek, J. Juryšek, D. Mandát, et al. Aerosol measurements at sub-percent precision using wide-field stellar photometry. In *Journal of Physics: Conference Series*, volume 2398, page 012009. IOP Publishing, 2022.

[17] C. M. Hui and VERITAS collaboration. VERITAS Distant Laser Calibration and Atmospheric Monitoring. In *AIP Conference Proceedings*, volume 1085, pages 735–737. American Institute of Physics, 2008.

[18] J. Hahn and R. De los Reyes. Atmospheric monitoring in HESS. In *EPJ Web of Conferences*, volume 89, page 02002. EDP Sciences, 2015.

[19] C. Fruck and M. Gaug. Atmospheric monitoring in MAGIC and data corrections. In *EPJ Web of Conferences*, volume 89, page 02003. EDP Sciences, 2015.

[20] R. Mussa, S. Argiro, R. Cester, M. Chiosso, A. Filipčič, M. Horvat, J. Matthews, M. Mostafa, M. Roberts, G. Sequeiros, et al. The LIDAR systems for atmospheric monitoring in Auger. *Nuclear Instruments and Methods in Physics Research Section A: Accelerators, Spectrometers, Detectors and Associated Equipment*, 518(1-2):183–185, 2004.

[21] S. J. Nolan, Ge. Puehlhofer, and C. B. Rulten. Detailed studies of atmospheric calibration in imaging Cherenkov astronomy. *Astroparticle Physics*, 34(5):304–313, 2010.

[22] D. Sobczyńska and W. Bednarek. The impact of clouds on image parameters in IACT at very high energies. In *EPJ Web of Conferences*, volume 89, page 03009. EDP Sciences, 2015.

[23] J. Ebr, T. Bulik, L. Font, M. Gaug, P. Janecek, J. Jurysek, D. Mandat, S. Stefanik, L. Valore, G. Vasileiadis, and The CTA Consortium. Atmospheric calibration of the Cherenkov Telescope Array. *arXiv preprint arXiv:1709.04273*, 2017.

[24] CTA Consortium et al. *Science with the Cherenkov Telescope Array*. World Scientific, 2018.

[25] M. Will. Atmospheric Monitoring at the Site of the MAGIC Telescopes. In *EPJ Web of Conferences*, volume 144, page 01002. EDP Sciences, 2017.

[26] B. R. Dawson. The importance of atmospheric monitoring at the Pierre Auger Observatory. In *EPJ Web of Conferences*, volume 144, page 01001. EDP Sciences, 2017.

[27] L. Valore, C. Aramo, B. M. Dinelli, F. Di Pierro, G. Dughera, M. Gaug, M. Iarlori, M. Marengo, E. Papandrea, E. Pietropaolo, et al. The ARCADE Raman Lidar and atmospheric simulations for the Cherenkov Telescope Array. *arXiv preprint arXiv:1709.04246*, 2017.

[28] J. Jurysek, M. Prouza, et al. Sun/Moon photometer for Cherenkov Telescope Array-first results. In *35th International Cosmic Ray Conference (ICRC2017)*, volume 301, page 853, 2017.

[29] G. Vasileiadis et al. Raman LIDARs for atmospheric calibration in CTA. *Proc. 35th ICRC*, 2017.

[30] J. Adam, J. Buss, K. Brügge, M. Nöthe, and W. Rhode. Cloud detection and prediction with all sky cameras. In *EPJ Web of Conferences*, volume 144, page 01004. EDP Sciences, 2017.

[31] O. Ballester, M. Gaug, G. Vasileiadis, et al. Raman LIDARs and atmospheric calibration along the line-of-sight of the Cherenkov Telescope Array. In *36th International Cosmic Ray Conference-ICRC2019*, volume 814, 2019.

[32] M. Doro, M. Gaug, J. Pallotta, G. Vasileiadis, et al. Status and motivation of Raman LIDARs development for the CTA Observatory. *arXiv preprint arXiv:1402.0638*, 2014.

[33] D. G. Andrews. *An introduction to atmospheric physics*. Cambridge University Press, 2010.

[34] D. J. Griffiths. *Introduction to electrodynamics 4th ed.* Pearson Education Inc., New Jersey, 2013.

[35] K. N. Liou. *An introduction to atmospheric radiation*, volume 84. Elsevier, 2002.

[36] J. W. Strutt. XV. On the light from the sky, its polarization and colour. *The London, Edinburgh, and Dublin Philosophical Magazine and Journal of Science*, 41(271):107–120, 1871.

[37] G. Mie. Beiträge zur Optik trüber Medien, speziell kolloidaler Metallösungen. *Annalen der physik*, 330(3):377–445, 1908.

[38] C. F. Bohren and D. R. Huffman. *Absorption and scattering of light by small particles*. John Wiley & Sons, 1983.

[39] M. I. Mishchenko, L. D. Travis, and A. A. Lacis. *Scattering, absorption, and emission of light by small particles*. Cambridge university press, 2002.

[40] H. C. van de Hulst. *Light scattering by small particles*. Courier Corporation, 1981.

[41] V. A. Kovalev and W. E. Eichinger. *Elastic lidar: theory, practice, and analysis methods*. John Wiley & Sons, 2004.

[42] G. W. Petty. *A first course in atmospheric radiation*. Sundog Publishing, 2006.

[43] L. Wang. *Study of atmospheric aerosol properties in the Vipava valley*. PhD thesis, 2018.

[44] D. Halliday, R. Resnick, and J. Walker. *Fundamentals of physics*. John Wiley & Sons, 2013.

[45] K. N. Liou and H. Lahore. Laser sensing of cloud composition: a backscattered depolarization technique. *Journal of Applied Meteorology*, 13(2):257–263, 1974.

[46] D. Atlas, M. Kerker, and W. Hitschfeld. Scattering and attenuation by nonspherical atmospheric particles. *Journal of Atmospheric and Terrestrial Physics*, 3(2):108–119, 1953.

[47] P. Chỳlek. Depolarization of electromagnetic radiation scattered by nonspherical particles. *Journal of the Optical Society of America*, 67(2):175–178, 1977.

[48] E. H. Synge. XCI. A method of investigating the higher atmosphere. *The London, Edinburgh, and Dublin Philosophical Magazine and Journal of Science*, 9(60):1014–1020, 1930.

[49] M. A. Tuve, E. A. Johnson, and O. R. Wulf. A new experimental method for study of the upper atmosphere. *Terrestrial Magnetism and Atmospheric Electricity*, 40(4):452–454, 1935.

[50] E. A. Johnson, R. C. Meyer, R. E. Hopkins, and W. H. Mock. The measurement of light scattered by the upper atmosphere from a search-light beam. *JOSA*, 29(12):512–517, 1939.

[51] T Maiman. Stimulated Optical Radiation in Ruby. *Nature*, 187:493–494, 1960.

[52] F. J. McClung and R. W. Hellwarth. Giant optical pulsations from ruby. *Applied Optics*, 1(101):103–105, 1962.

[53] G. Fiocco and L. D. Smullin. Detection of scattering layers in the upper atmosphere (60–140 km) by optical radar. *Nature*, 199(4900):1275–1276, 1963.

[54] C. Weitkamp. *Lidar: range-resolved optical remote sensing of the atmosphere*, volume 102. Springer Science & Business, 2006.

[55] J. A. Cooney. Measurements on the Raman component of laser atmospheric backscatter. *Applied Physics Letters*, 12(2):40–42, 1968.

[56] J. Cooney. Remote measurements of atmospheric water vapor profiles using the Raman component of laser backscatter. *Journal of Applied Meteorology (1962-1982)*, 9(1):182–184, 1970.

[57] A. Comerón, C. Muñoz-Porcar, F. Rocadenbosch, A. Rodríguez-Gómez, and M. Sicard. Current research in lidar technology used for the remote sensing of atmospheric aerosols. *Sensors*, 17(6):1450, 2017.

[58] G. R. North, J. A. Pyle, and F. Zhang. *Encyclopedia of atmospheric sciences*, volume 1-6. Elsevier, 2014.

[59] J. Harms. Lidar return signals for coaxial and noncoaxial systems with central obstruction. *Applied Optics*, 18(10):1559–1566, 1979.

[60] U. Wandinger and A. Ansmann. Experimental determination of the lidar overlap profile with raman lidar. *Applied Optics*, 41(3):511–514, 2002.

[61] A. Ansmann, M. Riebesell, and C. Weitkamp. Measurement of atmospheric aerosol extinction profiles with a Raman lidar. *Optics letters*, 15(13):746–748, 1990.

[62] David N Whiteman. Examination of the traditional Raman lidar technique. I. Evaluating the temperature-dependent lidar equations. *Applied Optics*, 42(15):2571–2592, 2003.

[63] D. N. Whiteman. Examination of the traditional Raman lidar technique. II. Evaluating the ratios for water vapor and aerosols. *Applied optics*, 42(15):2593–2608, 2003.

[64] A. Ansmann, U. Wandinger, M. Riebesell, C. Weitkamp, and W. Michaelis. Independent measurement of extinction and backscatter profiles in cirrus clouds by using a combined Raman elastic-backscatter lidar. *Applied optics*, 31(33):7113–7131, 1992.

[65] L. Wang, S. Stanič, W. Eichinger, X. Song, and M. Zavrtanik. Development of an automatic polarization raman LiDAR for aerosol monitoring over complex terrain. *Sensors*, 19(14):3186, 2019.

[66] D. Renaut, J. C. Pourny, and R. Capitini. Daytime Raman-lidar measurements of water vapor. *Optics letters*, 5(6):233–235, 1980.

[67] D. N. Whiteman, S. H. Melfi, and R. A. Ferrare. Raman lidar system for the measurement of water vapor and aerosols in the Earth's atmosphere. *Applied optics*, 31(16):3068–3082, 1992.

[68] H. Inaba and T. Kobayasi. Laser-Raman radar—Laser-Raman scattering methods for remote detection and analysis of atmospheric pollution. *Opto-electronics*, 4:101–123, 1972.

[69] J. E. M. Goldsmith, F. H. Blair, S. E. Bisson, and D. D. Turner. Turn-key Raman lidar for profiling atmospheric water vapor, clouds, and aerosols. *Applied Optics*, 37(21):4979–4990, 1998.

[70] S. E. Bisson, J. E. M. Goldsmith, and M. G. Mitchell. Narrow-band, narrow-field-of-view Raman lidar with combined day and night capability for tropospheric water-vapor profile measurements. *Applied optics*, 38(9):1841–1849, 1999.

[71] Y. Arshinov and S. Bobrovnikov. Use of a Fabry–Perot interferometer to isolate pure rotational Raman spectra of diatomic molecules. *Applied optics*, 38(21):4635–4638, 1999.

[72] Y. F. Arshinov, S. M. Bobrovnikov, V. E. Zuev, and V. M. Mitev. Atmospheric temperature measurements using a pure rotational Raman lidar. *Applied Optics*, 22(19):2984–2990, 1983.

[73] A. T. Young. Revised depolarization corrections for atmospheric extinction. *Applied optics*, 19(20):3427–3428, 1980.

[74] A. T. Young. On the Rayleigh-scattering optical depth of the atmosphere. *Journal of Applied Meteorology (1962-1982)*, pages 328–330, 1981.

[75] D. R. Bates. Rayleigh scattering by air. *Planetary and Space Science*, 32(6):785–790, 1984.

[76] A. Bucholtz. Rayleigh-scattering calculations for the terrestrial atmosphere. *Applied optics*, 34(15):2765–2773, 1995.

[77] B. A. Bodhaine, N. B. Wood, E. G. Dutton, and J. R. Slusser. On Rayleigh optical depth calculations. *Journal of Atmospheric and Oceanic Technology*, 16(11):1854–1861, 1999.

[78] D. Müller, A. Ansmann, I. Mattis, M. Tesche, U. Wandinger, D. Althausen, and G. Pisani. Aerosol-type-dependent lidar ratios observed with Raman lidar. *Journal of Geophysical Research: Atmospheres*, 112(D16), 2007.

[79] J. Gasteiger, M. Wiegner, S. Groß, V. Freudenthaler, C. Toledano, M. Tesche, and K. Kandler. Modelling lidar-relevant optical properties of complex mineral dust aerosols. *Tellus B: Chemical and Physical Meteorology*, 63(4):725–741, 2011.

[80] M. Haarig, A. Ansmann, H. Baars, C. Jimenez, I. Veselovskii, R. Engelmann, and D. Althausen. Depolarization and lidar ratios at 355, 532, and 1064 nm and microphysical properties of aged tropospheric and stratospheric Canadian wildfire smoke. 2018.

[81] R. Zhang, A. F. Khalizov, J. Pagels, D. Zhang, H. Xue, and P. H. McMurry. Variability in morphology, hygroscopicity, and optical properties of soot aerosols during atmospheric processing. *Proceedings of the National Academy of Sciences*, 105(30):10291–10296, 2008.

[82] K. Adachi, S. H. Chung, and P. R. Buseck. Shapes of soot aerosol particles and implications for their effects on climate. *Journal of Geophysical Research: Atmospheres*, 115(D15), 2010.

[83] S. China, B. Scarnato, R. C. Owen, B. Zhang, M. T. Ampadu, S. Kumar, K. Dzepina, M. P. Dziobak, P. Fialho, J. A. Perlinger, et al. Morphology and mixing state of aged soot particles at a remote marine free troposphere site: Implications for optical properties. *Geophysical Research Letters*, 42(4):1243–1250, 2015.

[84] R. M. Schotland, K. Sassen, and R. Stone. Observations by lidar of linear depolarization ratios for hydrometeors. *Journal of Applied Meteorology and Climatology*, 10(5):1011–1017, 1971.

[85] D. N. Whiteman and S. H. Melfi. Cloud liquid water, mean droplet radius, and number density measurements using a Raman lidar. *Journal of Geophysical Research: Atmospheres*, 104(D24):31411–31419, 1999.

[86] C. Jimenez, A. Ansmann, R. Engelmann, D. Donovan, A. Malinka, P. Seifert, R. Wiesen, M. Radenz, Z. Yin, J. Bühl, et al. The dual-field-of-view polarization lidar technique: a new concept in monitoring aerosol effects in liquid-water clouds–case studies. *Atmospheric Chemistry and Physics*, 20(23):15265–15284, 2020.

[87] J. Reichardt, S. Reichardt, M. Hess, and T. J. McGee. Correlations among the optical properties of cirrus-cloud particles: Microphysical interpretation. *Journal of Geophysical Research: Atmospheres*, 107(D21):AAC–8, 2002.

[88] K. Sassen, A. W. Huggins, A. B. Long, J. B. Snider, and R. J. Meitín. Investigations of a winter mountain storm in Utah. Part II: Mesoscale structure, supercooled liquid water development, and precipitation processes. *Journal of the atmospheric sciences*, 47(11):1323–1350, 1990.

[89] I. Veselovskii, P. Goloub, T. Podvin, D. Tanre, A. Ansmann, M. Korenskiy, A. Borovoi, Q. Hu, and D. N. Whiteman. Spectral dependence of backscattering coefficient of mixed phase clouds over West Africa measured with two-wavelength Raman polarization lidar: Features attributed to ice-crystals corner reflection. *Journal of Quantitative Spectroscopy and Radiative Transfer*, 202:74–80, 2017.

[90] V. Freudenthaler, M. Esselborn, M. Wiegner, B. Heese, M. Tesche, A. Ansmann, D. Müller, D. Althausen, M. Wirth, A. Fix, et al. Depolarization ratio profiling at several wavelengths in pure Saharan dust during SAMUM 2006. *Tellus B: Chemical and Physical Meteorology*, 61(1):165–179, 2009.

[91] Markus Gaug et al. The IFAE/UAB Raman LIDAR for the CTA-North. In *EPJ Web of Conferences*, volume 197, page 02005. EDP Sciences, 2019.

[92] D. Alexandreas et al. Status report on CLUE. *Nuclear Instruments and Methods in Physics Research Section A: Accelerators, Spectrometers, Detectors and Associated Equipment*, 360(1-2):385–389, 1995.

[93] P. Baillon, A. Braem, G. Gendre, G. Muratori, and C. Nichols. An improved method for manufacturing accurate and cheap glass parabolic mirrors. *Nuclear Instruments and Methods in Physics Research Section A: Accelerators, Spectrometers, Detectors and Associated Equipment*, 276(3):492–495, 1989.

[94] P. Baillon, A. Braem, T. Ekelöf, G. Gendre, A. Hallgren, G. Muratori, C. Nichols, T. Rydqvist, and S. Walles. Production of 300 paraboloidal mirrors with high reflectivity for use in the Barrel RICH counter in DELPHI at LEP. *Nuclear Instruments and Methods in Physics Research Section A: Accelerators, Spectrometers, Detectors and Associated Equipment*, 277(2-3):338–346, 1989.

[95] A. López-Oramas. *Multi-year campaign of the gamma-ray binary LS I +61° 303 and search for VHE emission from gamma-ray binary candidates with the MAGIC telescopes*. PhD thesis, 2014.

[96] V. Da Deppo, M. Doro, O. Blanch, L. Font, A. Lopez, M. Gaug, and M. Martinez. Preliminary optical design of a polychromator for a Raman LIDAR for atmospheric calibration of the Cherenkov Telescope Array. In *Optical Systems Design 2012*, volume 8550, pages 537–543. SPIE, 2012.

[97] J. Cortina and C. l. Project. Status of the Large Size Telescopes of the Cherenkov Telescope Array. In *36th International Cosmic Ray Conference (ICRC2019)*, volume 36 of *International Cosmic Ray Conference*, page 653, July 2019.

[98] T. Bretz. Standard Analysis for the MAGIC telescope. 2005.

[99] A. Moralejo, M. Gaug, E. Carmona, P. Colin, C. Delgado, S. Lombardi, D. Mazin, V. Scalzotto, J. Sitarek, and D. Tescaro. MARS, the MAGIC analysis and reconstruction software. *arXiv preprint arXiv:0907.0943*, 2009.

[100] Chohong Min. Local level set method in high dimension and codimension. *Journal of computational physics*, 200(1):368–382, 2004.

[101] M. Gaug, L. Font, and C. Maggio. Site Characterization of the Northern Site of the Cherenkov Telescope Array. In *EPJ Web of Conferences*, volume 144, page 01010. EDP Sciences, 2017.

[102] F. Weiser, E. Baumann, A. Jentsch, F. M. Medina, M. Lu, M. Nogales, and C. Beierkuhnlein. Impact of Volcanic Sulfur Emissions on the Pine Forest of La Palma, Spain. *Forests*, 13(2):299, 2022.

[103] S. Rodríguez, C. Torres, J.-C. Guerra, and E. Cuevas. Transport pathways of ozone to marine and free-troposphere sites in Tenerife, Canary Islands. *Atmospheric Environment*, 38(28):4733–4747, 2004.

[104] J. Carrillo, J. C. Guerra, E. Cuevas, and J. Barrancos. Characterization of the marine boundary layer and the trade-wind inversion over the sub-tropical North Atlantic. *Boundary-layer meteorology*, 158(2):311–330, 2016.

[105] C. Criado and P. Dorta. An unusual 'blood rain'over the Canary Islands (Spain). The storm of January 1999. *Journal of Arid Environments*, 55(4):765–783, 2003.

[106] G. Lombardi, V. Zitelli, S. Ortolani, M. Pedani, and A. Ghedina. El Roque de Los Muchachos site characteristics III. Analysis of atmospheric dust and aerosol extinction. *Astronomy & Astrophysics*, 483(2):651–659, 2008.

[107] H. von Suchodoletz, B. Glaser, T. Thrippleton, T. Broder, U. Zang, R. Eigenmann, B. Kopp, M. Reichert, and Z. Ludwig. The influence of Saharan dust deposits on La Palma soil properties (Canary Islands, Spain). *Catena*, 103:44–52, 2013.

[108] M. Sicard, M. N. Md Reba, S. Tomás, A. Comerón, O. Batet, C. Muñoz-Porcar, A. Rodríguez, F. Rocadenbosch, C. Muñoz-Tuñón, and J. J. Fuensalida. Results of site testing using an aerosol, backscatter lidar at the Roque de los Muchachos Observatory. *Monthly Notices of the Royal Astronomical Society*, 405(1):129–142, 2010.

[109] A. García-Gil, C. Muñoz-Tuñón, and A. M. Varela. Atmosphere extinction at the ORM on La Palma: A 20 yr statistical database gathered at the Carlsberg Meridian Telescope. *Publications of the Astronomical Society of the Pacific*, 122(895):1109, 2010.

[110] T. Fehr, V. Amiridis, S. Bley, P. Cocquerez, C. Lemmerz, G. Močnik, G. Skofronick-Jackson, and A. Grete Straume. Aeolus calibration, validation and science campaigns. In *EGU General Assembly Conference Abstracts*, page 19778, 2020.

[111] T. Fehr, G. Skofronick-Jackson, V. Amiridis, J. von Bismarck, S. Chen, C. Flamant, R. Koopman, C. Lemmerz, G. Močnik, T. Parrinello, et al. The Joint ESA-NASA Tropical Campaign Activity-Aeolus Calibration/Validation and Science in the Topics. In *EGU General Assembly Conference Abstracts*, pages EGU21–15144, 2021.

[112] E. Marinou, V. Amiridis, I. Mavropoulou, H. Baars, S. Kazadzis, M. Rosoldi, D. Ene, A. Barreto, S. Casadio, C. Zenk, et al. The ASKOS experiment for the validation of Aeolus L2A aerosol product. Technical report, Copernicus Meetings, 2021.

[113] S. Groß, M. Esselborn, B. Weinzierl, M. Wirth, A. Fix, and A. Petzold. Aerosol classification by airborne high spectral resolution lidar observations. *Atmospheric chemistry and physics*, 13(5):2487–2505, 2013.

[114] M. Gutleben, S. Groß, C. Heske, and M. Wirth. Wintertime Saharan dust transport towards the Caribbean: an airborne lidar case study during EUREC 4 A. *Atmospheric Chemistry and Physics*, 22(11):7319–7330, 2022.

[115] M. Haarig, A. Ansmann, R. Engelmann, H. Baars, C. Toledano, B. Torres, D. Althausen, M. Radenz, and U. Wandinger. First triple-wavelength lidar observations of depolarization and extinction-to-backscatter ratios of Saharan dust. *Atmospheric Chemistry and Physics*, 22(1):355–369, 2022.

[116] A. F. Stein, R. R. Draxler, G. D. Rolph, B. J. B. Stunder, M. D. Cohen, and F. Ngan. NOAA's HYSPLIT atmospheric transport and dispersion modeling system. *Bulletin of the American Meteorological Society*, 96(12):2059–2077, 2015.

[117] G. Rolph, A. Stein, and B. Stunder. Real-time environmental applications and display system: READY. *Environmental Modelling & Software*, 95:210–228, 2017.

[118] Jan Pękala. Atmospheric scattering of light emitted by extensive air showers, 2007.

[119] J. Abraham, P. Abreu, M. Aglietta, C. Aguirre, E. J. Ahn, D. Allard, I. Allekotte, J. Allen, J. Alvarez-Muñiz, M. Ambrosio, et al. A study of the effect of molecular and aerosol conditions in the atmosphere on air fluorescence measurements at the Pierre Auger Observatory. *Astroparticle Physics*, 33(2):108–129, 2010.

[120] J. Pękala and H. Wilczyński. Point spread function due to multiple scattering of light in the atmosphere. *Nuclear Instruments and Methods in Physics Research*

Section A: Accelerators, Spectrometers, Detectors and Associated Equipment, 729:296–301, 2013.

[121] K. Louedec and J. Colombi. Atmospheric multiple scattering of fluorescence light from extensive air showers and effect of the aerosol size on the reconstruction of energy and depth of maximum. *Astroparticle Physics*, 57:6–15, 2014.

[122] H. R. Pruppacher and J. D. Klett. Microphysics of clouds and precipitation, 1980.

[123] Z. A. Kanji, L. A. Ladino, H. Wex, Y. Boose, M. Burkert-Kohn, D. J. Cziczo, and M. Krämer. Overview of ice nucleating particles. *Meteorological Monographs*, 58:1–1, 2017.

[124] J. Mülmenstädt, O. Sourdeval, J. Delanoë, and J. Quaas. Frequency of occurrence of rain from liquid-, mixed-, and ice-phase clouds derived from A-Train satellite retrievals. *Geophysical Research Letters*, 42(15):6502–6509, 2015.

[125] C. E. Morris, D. G. Georgakopoulos, and D. C. Sands. Ice nucleation active bacteria and their potential role in precipitation. In *Journal de Physique IV (Proceedings)*, volume 121, pages 87–103. EDP sciences, 2004.

[126] J. Sun and P. A. Ariya. Atmospheric organic and bio-aerosols as cloud condensation nuclei (CCN): A review. *Atmospheric Environment*, 40(5):795–820, 2006.

[127] T. Šantl-Temkiv, P. Amato, E. O. Casamayor, P. K. H. Lee, and S. B. Pointing. Microbial ecology of the atmosphere. *FEMS Microbiology Reviews*, 46(4):fuac009, 2022.

[128] U. Dusek, G. P. Frank, L. Hildebrandt, J. Curtius, J. Schneider, S. Walter, D. Chand, F. Drewnick, S. Hings, D. Jung, et al. Size matters more than chemistry for cloud-nucleating ability of aerosol particles. *Science*, 312(5778):1375–1378, 2006.

[129] T. Šantl-Temkiv, B. Sikoparija, T. Maki, F. Carotenuto, P. Amato, M. Yao, C. E. Morris, R. Schnell, R. Jaenicke, C. Pöhlker, et al. Bioaerosol field measurements: Challenges and perspectives in outdoor studies. *Aerosol Science and Technology*, 54(5):520–546, 2020.

[130] M. Živec and L. Wang. *Two-wavelength polarization Raman lidar: Operating manual-v1.0*. 2020.

[131] A. Filipčič, M. Horvat, D. Veberič, D. Zavrtanik, M. Zavrtanik, M. Chiosso, R. Mussa, G. Sequeiros, M. A. Mostafa, and M. D. Roberts. Pierre Auger atmosphere - monitoring lidar system. In *28th International Cosmic Ray Conference*, pages 461–464, 5 2003.

[132] S. Argirò, R. Cester, M. Chiosso, R. Mussa, G. Sequeiros, J. Matthews, M. Mostafà, M. Roberts, A. Filipčič, M. Horvat, et al. The Atmospheric Monitoring with Lidar for the Pierre Auger Observatory. In *Thinking, Observing And Mining The Universe*, pages 301–302. World Scientific, 2004.

[133] S. Y. BenZvi, R. Cester, M. Chiosso, B. M. Connolly, A. Filipčič, B. Garcia, A. Grillo, F. Guarino, M. Horvat, M. Iarlori, et al. The lidar system of the Pierre Auger Observatory. *Nuclear Instruments and Methods in Physics Research Section A: Accelerators, Spectrometers, Detectors and Associated Equipment*, 574(1):171–184, 2007.

[134] H. Amin, I. P. G. Marshall, R. J. Bertelsen, I. M. Wouters, V. Schlünssen, T. Sigsgaard, and T. Šantl-Temkiv. Optimization of bacterial DNA and endotoxin extraction from settled airborne dust. *Science of the Total Environment*, 857:159455, 2023.

[135] RC Team. R: A language and environment for statistical computing v. 3.6. 1 (R Foundation for Statistical Computing, Vienna, Austria, 2019). *Sci Rep*, 11:12957, 2021.

[136] M. Martin. Cutadapt removes adapter sequences from high-throughput sequencing reads. *EMBnet. journal*, 17(1):10–12, 2011.

[137] B. J. Callahan, P. J. McMurdie, M. J. Rosen, A. W. Han, A. J. A. Johnson, and S. P. Holmes. DADA2: High-resolution sample inference from Illumina amplicon data. *Nature methods*, 13(7):581–583, 2016.

[138] U. Kõljalg, H. R. Nilsson, D. Schigel, L. Tedersoo, K.-H. Larsson, T. W. May, A. F. S. Taylor, T. S. Jeppesen, T. G. Frøslev, B. D. Lindahl, et al. The taxon hypothesis paradigm—On the unambiguous detection and communication of taxa. *Microorganisms*, 8(12):1910, 2020.

[139] R. H. Nilsson, K.-H. Larsson, A. F. S. Taylor, J. Bengtsson-Palme, T. S. Jeppesen, D. Schigel, P. Kennedy, K. Picard, F. O. Glöckner, L. Tedersoo, et al. The UNITE database for molecular identification of fungi: handling dark taxa and parallel taxonomic classifications. *Nucleic acids research*, 47(D1):D259–D264, 2019.

[140] N. M. Davis, D. M. Proctor, S. P. Holmes, D. A. Relman, and B. J. Callahan. Simple statistical identification and removal of contaminant sequences in marker-gene and metagenomics data. *Microbiome*, 6:1–14, 2018.

[141] C. Wieber, K. W. Finster, C. Melvad, et al. PINGUIN: An ice nucleation instrument for the precise characterisation of ice nucleating particles. *Atmospheric Measurement Techniques*.

[142] G. Vali. Quantitative evaluation of experimental results an the heterogeneous freezing nucleation of supercooled liquids. *Journal of Atmospheric Sciences*, 28(3):402–409, 1971.

[143] T. Storelvmo and I. Tan. The Wegener–Bergeron–Findeisen process—Its discovery and vital importance for weather and climate. *Meteorologische Zeitschrift*, 24(4):455–461, 2015.

[144] E. L. Simpson, P. J. Connolly, and G. McFiggans. Competition for water vapour results in suppression of ice formation in mixed-phase clouds. *Atmospheric Chemistry and Physics*, 18(10):7237–7250, 2018.

[145] B. J. Murray, D. O'Sullivan, J. D. Atkinson, and M. E. Webb. Ice nucleation by particles immersed in supercooled cloud droplets. *Chemical Society Reviews*, 41(19):6519–6554, 2012.